LBL-34176
UC-413

Lawrence Berkeley Laboratory
UNIVERSITY OF CALIFORNIA

Published as a chapter in *Annual Reviews of Nuclear and Particle Science,* J.D. Jackson, Ed., Annual Reviews, Inc., Palo Alto, CA, May 1993

Multifragmentation in Heavy-Ion Processes

L.G. Moretto and G.J. Wozniak

May 1993

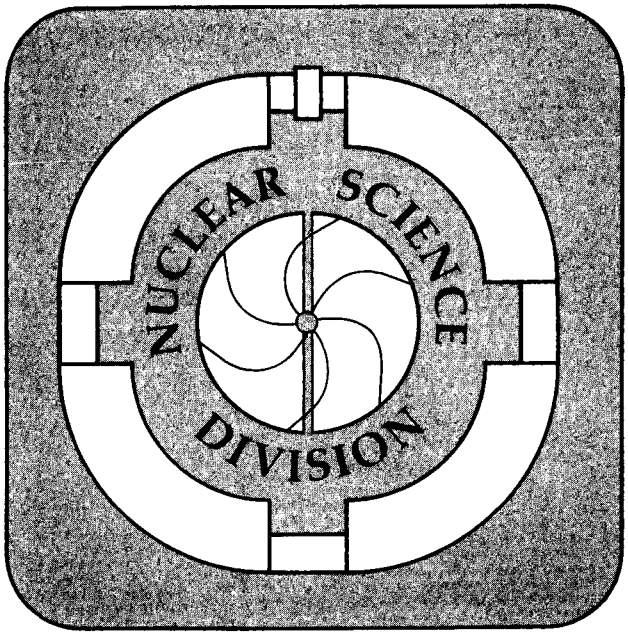

LOAN COPY
Circulates
for 4 weeks
Bldg. 50 Library.
LBL-34176
Copy 2

Prepared for the U.S. Department of Energy under Contract Number DE-AC03-76SF00098

DISCLAIMER

This document was prepared as an account of work sponsored by the United States Government. While this document is believed to contain correct information, neither the United States Government nor any agency thereof, nor the Regents of the University of California, nor any of their employees, makes any warranty, express or implied, or assumes any legal responsibility for the accuracy, completeness, or usefulness of any information, apparatus, product, or process disclosed, or represents that its use would not infringe privately owned rights. Reference herein to any specific commercial product, process, or service by its trade name, trademark, manufacturer, or otherwise, does not necessarily constitute or imply its endorsement, recommendation, or favoring by the United States Government or any agency thereof, or the Regents of the University of California. The views and opinions of authors expressed herein do not necessarily state or reflect those of the United States Government or any agency thereof or the Regents of the University of California.

LBL - 34176

Multifragmentation in Heavy-Ion Processes

Luciano G. Moretto and Gordon J. Wozniak

Nuclear Science Division, Lawrence Berkeley Laboratory
University of California, Berkeley, California 94720, USA

May 1993

This work was supported by the Director, Office of Energy Research, Division of Nuclear Physics of the Office of High Energy and Nuclear Physics of the U.S. Department of Energy under Contract DE-AC03-76SF00098

MULTIFRAGMENTATION IN HEAVY-ION PROCESSES

Luciano G. Moretto and Gordon J. Wozniak

Nuclear Science Division, Lawrence Berkeley Laboratory, Berkeley, CA 94720, USA

KEY WORDS: Multifragmentation, Intermediate Mass Fragments, Complex Fragments

Shortened Title: MULTIFRAGMENTATION

CONTENTS

1. INTRODUCTION 3

2. STATISTICAL THEORIES 7

2.1 Sequential Binary Decay 7

2.2 Direct Binary Plus Compound Binary Decay 8

2.3 Multifragmentation and Nuclear Comminution 9

2.4 Statistical Multifragmentation 11

2.5 Percolation 20

2.6 Statistical Shattering 22

3. DYNAMICAL THEORIES 24

3.1 Instabilities: Volume and Surface 25

3.2 Metastability of a Sheet of Liquid 27

3.3 Instability of a Sheet of Liquid and Surface-Surface Interactions 28

3.4 Application to Simulated Nuclear Collisions 29

3.5 Onset of Surface Instabilities 31

3.6 Donuts and Bubbles 32

3.7 Coulomb-induced Instabilities and "Stabilities" in Liquid Spheres and Bubbles 33

4. EXPERIMENTAL EVIDENCE 35

4.1 The Hot Environment of Multifragmentation 35

4.2 Sources of Multifragmentation: Experimental Observables and Key Variables 41

4.3 High Energy p- and ^{3,4}He-induced Reactions 54

4.4 Mass(Charge) Distributions 56

5. CONCLUSION 58

1. INTRODUCTION

After many decades of intensive study, the field of nuclear physics has reached a moment of critical differentiation. Beguiled by ever higher energies, one of its branches has separated itself from traditional nuclear physics to leap into the unexplored space of deconfinement and quark-gluon plasma. A second branch, tended by the epigones of low energy γ-ray spectroscopy, is now living in the dazzling world of ever faster whirling nuclei. A third branch yet, in the best tradition of nuclear physics, is successfully studying nuclear collectivity through giant resonances of one sort or another. Lastly, the branch that grew out of compound nucleus and fission studies, and matured through low energy deep-inelastic scattering, is now exploring the field of intermediate energy heavy-ion reactions, looking through the rubble of dismantled nuclei for one last gem. It is the great expectations and tantalizing achievements of this last branch of nuclear physics that we will discuss here. The gem is multifragmentation, a process still poorly characterized experimentally, which has moved many theoreticians to put forth a large number of theories touching at the soul of nuclear physics.

The story of multifragmentation is intimately connected with that of complex fragments. Complex fragments, alternatively called intermediate mass fragments, have been the object of a great deal of attention in recent years, because of their rather pervasive presence in many reactions at intermediate energies. Since the label "complex fragments" is used with a broad range of meanings, *we define as complex fragments those reaction products falling between ^{4}He and fission fragments that bear no obvious genetic relationship to either the target or projectile.* The need for such a classification stems from the fact that, until not long ago, a complex fragment was a rare bird seldom seen flying, and even then the object more of ornithological curiosity than of systematic scientific interest.

Complex fragments, like ^{24}Na, were first identified radiochemically(1-4) in high energy proton bombardments of medium to heavy targets. Subsequently, instrumental techniques(5, 6) were used to identify a broad range of fragments extending in atomic number up to $Z \sim 20$ and

above. However, these reactions were not considered as belonging to the mainstream of nuclear physics as understood at the time, and little attention was paid to them.

The advent of low energy heavy-ion reactions familiarized the nuclear community with reaction products ranging throughout the periodic table. Yet the genetic relationship of these products with either the target or projectile [as is the case of quasi-elastic or deep inelastic reactions, where both target and projectile retain their approximate identity] kept these processes more or less within the categorical boundaries of "direct reactions".

Intermediate energy heavy-ion reactions made their entrance accompanied by a readily observable cohort of complex fragments. Here the simplicity of binary quasi-elastic and deep inelastic collisions, prevailing at lower energy, was substituted by a mess of products that seemed to bear little or no relationship to either of the entrance channel partners. As a consequence, the abundant production of complex fragments, together with the turbid experimental environment of the early studies, prompted a tumultuous development of theories, claims, and counterclaims about the origin of these products. The day of complex fragments and of multifragmentation had come!

Early intermediate energy heavy-ion and proton-induced reactions showed mass distributions that followed a power law(7-11). Since a power-law distribution is predicted for droplets of liquid in equilibrium near the critical temperature, this experimental evidence was taken as a signature of liquid-vapor equilibrium at criticality. As discussed below, this signature is by no means unique, yet it sufficed to trigger unbounded enthusiasm and somewhat premature claims.

The day had also come for high energy proton-induced reactions, and for the people dedicated to their study. Their work suddenly became quite relevant, for the simple reason that the reactions they had been studying all along also produced fragments throughout the periodic table. Furthermore, there was a confident feeling that proton-induced fragment production would be inherently easier to interpret than the heavy-ion reaction counterpart.

Relativistic heavy-ion reactions were also shown to be generous producers of fragments(12-16) extending to and going beyond the boundaries of the known isotopes(17, 18).

Finally, complex fragments were detected in extremely low energy reactions(19-22) and, to complete the picture, even from the radioactive decay of ground state nuclei(23-26).

Nowadays, complex fragment emission has become an all-pervasive process, involving all excitation energies and all kinds of reactions. As such, it deserves a serious attempt at classification and systematic study.

The theoretical insight available at present reflects, by and large, the rather cavalier and pioneering attitude prevailing in many of the early studies. A brief description of the main theories that have been produced up to now may illustrate the point.

LIQUID-VAPOR EQUILIBRIUM It envisages the formation of a hot nuclear vapor condensing into droplets (complex fragments) somewhere near the critical temperature(27-35). It predicts a power law mass distribution that some experimenters claim to have established(7-11, 34-40).

STATISTICAL MULTIFRAGMENTATION THEORIES A hot nucleus is assumed to decay statistically into many fragments. A decay rate is evaluated at a suitably defined transition state(41-44), or a critical volume is postulated in which the fragments attain chemical and physical equilibrium. Agreement with many features of the experimental mass distributions has been claimed(45-51).

COLD FRAGMENTATION Nuclei are assumed to break up on impact and shatter like a piece of fragile material. A statistical ansatz for the resulting mass distribution is made. Agreement with experimental mass distributions has been claimed(52). This model has been generalized to include the effect of the surface energy(53).

TRANSPORT THEORIES These mean-field theories contain a collision term and are labelled with a variety of names and acronyms, e.g. BUU [Boltzmann-Uehling-Uhlenbeck(54)], Landau-Vlasov(55)], and BNV [Boltzmann-Nordheim-Vlasov(56)]. The dynamic evolution of systems resulting from collisions between two nuclei is studied numerically(55, 57-65). Fluctuations have

been incorporated in a Langevin-like approach(66-72). The somewhat related Quantum Molecular Dynamics (QMD) theory has also been propounded and employed to simulate intermediate energy-heavy ion collisions(59, 63, 73-77).

DYNAMICAL-STATISTICAL THEORIES A dynamically expanding nucleus is allowed to evaporate particles of any size during its dynamical evolution(78). The need is stressed for the evolution to a low density stage in order to explain the large yield of experimentally observed complex fragments(79).

PERCOLATION THEORIES Nuclei are imagined as aggregates of nucleons connected by bonds. As the percentage of broken bonds increases, one retains a main cluster (percolating cluster), which disappears above a critical percentage and is replaced by many clusters(80-91). Sometimes this theory is grafted to the end of a dynamical theory that provides, somehow, information about the number of broken bonds(92-99). Remarkably, this theory predicts many features of the experimentally observed mass distributions and fragment multiplicities.

STATISTICAL COMPOUND NUCLEUS DECAY A compound nucleus is assumed to be formed at a certain stage of the reaction. This compound nucleus then decays through all its available channels, including complex fragment emission(100, 101). Compound nucleus emission of complex fragments has been demonstrated at low energies (19-22) and the formation of compound nuclei at higher energies through complete or incomplete fusion processes has been verified(21, 102-108). Compound nucleus decay provides an important source of complex fragments. Therefore, sequential statistical-binary decay, or comminution(109), is an expected and to some extent predictable multifragmentation background that certainly exists and needs to be considered(21, 110).

HYBRID THEORIES A dynamical theory describes the initial stages of the reaction, while a statistical theory -- such as statistical multifragmentation, sequential compound nucleus decay, or percolation -- describes the final stages. They are mostly used to fit experimental data(93, 94, 96-99, 106, 111-118).

INTERMITTENCE ANALYSIS For the sake of completeness, we mention this method of analysis based on factorial moments that should permit one to establish deviations from Poissonian fluctuations in the data(119-122). It has been applied to charge or mass distributions. Because of its great sensitivity to the lightest particles (protons), its relevance to multifragmentation is uncertain.

After this admittedly schematic presentation, a rational classification of complex fragment production theories is possible. Our classification is shown in Figure 1. In it, the word (and concept) "binary" is of the essence. In our view, the binarity of a reaction, at whatever stage, should be the utmost concern of an experimental test. Lamentably, this has not always been the case.

Recent work has started to provide solid answers to some of the questions suggested by the above classification. In particular, the compound nucleus formed through complete or incomplete fusion has been shown to be a very important source of complex fragments over a wide range of excitation energies and of reactions(21, 105-108).

The aim of this paper is to offer an intelligible picture of the status of multifragmentation. This we try to achieve by presenting both theoretical and experimental approaches. A brief description of multifragmentation theories more commonly discussed in the literature is given, followed by a review of the experimental work. The reader may find it useful to consult other review papers emphasizing different aspects of this rapidly developing field(21, 34, 35, 51, 63, 123-130).

2. STATISTICAL THEORIES

2.1 Sequential Binary Decay

We use, as a guide through the labyrinth of multifragmentation theories, the diagram shown in the lower portion of Figure 1. The first heading, "sequential binary" refers to those theories in which multifragment emission occurs through a sequence of binary decays. These binary decays

can be either direct, or statistical. In a sense, these theories are already firmly established, since direct reactions are, in general, well understood, and so are statistical (compound) binary decays. The sequential occurrence of these binary processes is, as a consequence, a background on top of which "true" multifragmentation should stand. Nevertheless, it is of the utmost importance that such a background be understood, since the inherent simplicity of each step may be masked by the overwhelming complications arising from a long decay chain. Additional complications arise at the highest excitation energies, where temperature effects on **nuclear radii**, the **surface-energy coefficient**, and **level density parameters**, may lead to yet unknown and possibly dramatic changes in the decay widths.

2.2 Direct Binary Plus Compound Binary Decay

This is a very common process in low energy heavy-ion reactions, for instance, a deep inelastic scattering(128, 130) followed by "sequential" fission. The detail in which this sequential mechanism is understood has allowed one to discover, among other things, remarkable features of the reaction, for example, the magnitude and alignment of the primary fragment's angular momentum from the angular distribution of the fission fragments(131-133).

Ternary and quaternary events can result from a deep inelastic scattering, followed by statistical fission of one or both fragments(134, 135). Multibody events can also result from the breakup of excited projectile-like or target-like fragments produced in dissipative collisions. By detecting all the decay fragments, the excitation energy of the primary fragment can be determined. In addition, by analyzing the directional correlations among the particles, several sequential binary decays can, in principle, be distinguished from a prompt multifragmentation process(136). Analyses of reactions induced by light projectiles(137-140) show that the projectile is initially excited in a peripheral interaction with a heavy target nucleus and then subsequently decays sequentially, e. g., $^{16}O^*$ decays into four alpha particles.

At higher energies, the initial stage can be approximately described as the incomplete fusion of the target and projectile. The resulting incomplete fusion product(s) relaxes to a compound nucleus, which proceeds to decay statistically. In this statistical decay, one can observe the emission of one or more complex fragments. In rather asymmetric heavy-ion collisions, incomplete fusion followed by the statistical emission of one complex fragment by the incomplete fusion product may be the dominant fragment production mechanism. These reactions are understood quantitatively(21, 105).

2.3 Multifragmentation and Nuclear Comminution

The emission of complex fragments through binary compound nucleus decay is well understood(21). If there is enough excitation energy available, the primary binary-decay products are also very excited, and have a significant probability of decaying in turn into two additional fragments, and so on. In this very conventional way, one can describe the production of several fragments in the exit channel (multifragmentation) in terms of several sequential-binary decays. As mentioned above, at high excitation energies these multifragment events may be responsible for a substantial background to other predicted multifragmentation mechanisms. Sequential statistical emission is also very likely to affect the primary fragments of the more interesting multifragmentation reactions, making their interpretation all the more difficult.

This process of sequential-binary decay, controlled at each stage by the compound nucleus branching ratios, we call "nuclear comminution"(21, 109). It is bound by two main physical limitations. One obvious limitation is the ability of the system to form a compound nucleus. In other words, the relaxation times associated with compound nucleus formation may be too long when compared to the dynamical times leading the system to a different fate. Limitations of this sort are of course shared by all other multifragmentation processes involving an intermediate relaxed system.

The other limitation has to do with the aspect of sequentiality. Should two sequential-binary decays occur too close in space-time, they would interact to an extent incompatible with the definition of sequentiality. In this case one may be led to favor models in which fragments are formed simultaneously. Nonetheless, it may be possible to extend the sequential binary model to situations in which the interaction between two successive decays is only strong enough to perturb the angular distributions. The decay probabilities are overwhelmingly affected by the level densities of the corresponding final states. These level densities arise almost completely from the intrinsic degrees of freedom. The collective degrees of freedom, upon which the angular distributions depend, hardly contribute to the level densities. Therefore one could conceivably observe a multifragment pattern whose branching ratios are still clearly binary, while the angular distributions may be substantially perturbed.

The lesson to be learned from these considerations is that the best way to establish the underlying mechanism of a multifragmentation process may be to study the excitation functions of binary, ternary, quaternary, etc events, which are sensitive indicators of the statistical nature of the branching ratios, and not to be unduly troubled, should the angular distributions indicate multifragment interactions.

The calculations of the mass distributions arising from comminution are trivial in principle (except at very high energies, where temperature dependent changes in level density parameters and barriers may occur(141, 142)). They are, however, tedious and time consuming. As a simple illustration, we report the following comminution calculation(109). The process was simulated by assuming a potential energy curve $V(A)$ versus mass asymmetry (ridge line) with a maximum value of 40 MeV for symmetry and 8 MeV for the extreme asymmetries. The primary yield curve is taken to be of the simplified form: $Y(A) = K \exp[-V(A)/T(A)]$. Each of the resulting fragments A is assumed to have a similar ridge line and a properly scaled temperature $T(A)$, and each is allowed to decay accordingly, until all the excitation energy is exhausted. The resulting mass distributions are shown in Figure 2 for different initial excitation energies. At high

excitation energies, the log-log plots show a power law dependence for the yield of the low mass fragments. At excitation energies of about 400 MeV, the exponent (see Figure 3) is around 2.3 - 2.4. This value is very close to that expected for the liquid-vapor phase transition at the critical temperature. These simulations show that a power law dependence is not a unique diagnostic feature(21, 34, 35, 63, 109) of liquid-vapor equilibrium, but a "generic" feature that may arise even from sequential-binary decay or comminution. A more realistic calculation with the statistical decay code GEMINI(143) leads to similar results(21).

An example of an event with four complex fragments plus a multitude of lighter particles generated by GEMINI is shown in Figure 4. Of course, the analysis of individual complete events does not reveal the "statistical" nature of the branching ratios. The statistical nature of the decay can be appreciated more directly in the excitation functions for events with one, two, three, or more fragments in the exit channel, like those plotted in Figure 5. Here one can get a "qualitative" feeling for the statistical competition between channels in addition to quantitative predictions. In view of the uncertainties in the barriers used in the calculations, plus the fact that the temperature dependence of the barriers has not been included, the qualitative dependence of the branching ratios upon excitation energy may be the most important lesson to be derived from this exercise.

2.4 Statistical Multifragmentation

Statistical theories are the secure refuge to which we often repair in the absence of knowledge of the reaction mechanism. Their frequent success is due to the propensity of most systems to undergo relaxation even beyond "reasonable" expectations. However, multifragmentation presents a problem even at this level. The statistical decay width for a typical compound nucleus cannot be taken directly as a guide, since only binary decay channels have been treated in this approach. For instance, the generalization of the fission decay width (two fragments) to multifragmentation hinges on the existence and identification of multifragment

transition states in analogy to the binary transition state, or of a barrier presiding over multifragment decay. This approach has received only limited attention(42, 43, 144-146).

An alternative approach is to assume that many fragments are formed together in a certain volume, and that they are in chemical and physical equilibrium with each other, although it may not be easy to determine whether, how (and where!), a system may have achieved such an equilibrium. This approach has been implemented in a variety of models and codes, incorporating fragment masses, Coulomb energies, etc.(45, 48, 49, 51). Nonetheless, it is a useful exercise to calculate analytically some relevant distributions that may be used as minimal hypotheses in the analysis of experimental data. In the following, we consider three kinds of equilibria that have been discussed in the literature with some degree of attention: chemical, thermal, and angular momentum equilibria.

CHEMICAL EQUILIBRIUM Statistical mechanics shows one how to calculate equilibria of the general kind:

$$aA + bB + cC + \ldots \leftrightarrow \ell L + mM + nN + \ldots \tag{1}$$

or

$$\sum a_i I = 0. \tag{2}$$

For a system at equilibrium,

$$\sum a_i \mu_i = 0, \tag{3}$$

where μ_i are the chemical potentials of the ith species. These can be written as

$$\mu_i = -T \ln \frac{q_i}{N_i}, \tag{4}$$

where q_i is the partition function of the ith component. Substituting, one obtains

$$\sum \ln \left[\frac{q}{N_i} \right]^{a_i} = 0, \tag{5}$$

which is the result we have been looking for.

Liquid-vapor Equilibrium The "canonical" equilibrium described above requires the knowledge of the partition functions of the various species involved. The fact that nuclear matter behaves like a liquid, and nuclei obey a liquid-drop formula, permits a dramatic simplification because it reduces the problem to the process of nucleation in a nuclear vapor near saturation and/or criticality (neglecting the Coulomb interaction for the moment). In fact Fermi-Thomas(147-149) and Hartree-Fock calculations(29, 150) for nuclear matter lead to isotherms that are quite similar to those of the Van der Waals equation. In particular, there is a critical isotherm along which the two phases, liquid and vapor, identified through the Maxwell construction, lose their identity. At the critical point, density fluctuations acquire infinite range and manifest themselves through the spectacular phenomenon of critical opalescence. The distribution in cluster size can be derived in the following simple way(151, 152). The whole gas or vapor is an imperfect gas, but it can also be considered as an ideal gas mixture of clusters in equilibrium with each other. The condition of equilibrium between clusters of different size is: $\mu_j = j\mu$, where μ_j is the chemical potential of the clusters of size j and μ is the chemical potential of the clusters of size one.

Let J_j be the partition function of a cluster of size j. Then the partition function A_j of the m_j clusters of size j is

$$A_j = \frac{1}{m_j!} J_j^{m_j}. \tag{6}$$

The chemical potentials are:

$$-\frac{\mu_j}{T} = \frac{\partial \ln A_j}{\partial m_j} = \ln J_j - \ln m_j \tag{7}$$

and $m_j = J_j \exp[j\mu / T]$. The free energy of a cluster can be written as

$$F_j = -T \ln J_j = j\mu_L + cj^{2/3} \tag{8}$$

where μ_L is the chemical potential of the liquid and the term in $j^{2/3}$ is a surface contribution that takes care of the finite size of the cluster. Thus

$$m_j = y^j x^{j^{2/3}} \tag{9}$$

where

$$x = \exp[-c/T] \quad \text{and} \quad y = \exp[(\mu - \mu_L)/T]. \tag{10}$$

Below the critical temperature, and when the gas phase is stable $\mu < \mu_L$, $y < 1$, the contribution of large clusters is exponentially unimportant. On the other hand, if the liquid phase is stable, then $\mu \geqq \mu_L$ and the vapor is supersaturated. In this case, the first factor increases with j, and the second decreases with j. Therefore there is a value of j for which m_j is a minimum. This is given by

$$\frac{d \ln m_j}{dj} = 0 \quad \text{or} \quad \ln y = \frac{2c}{3Tj^{*1/3}}. \tag{11}$$

Clusters of this size represent a maximum in the free energy. Thus the size j^* defined by Equation 11 represents a hurdle to be overcome before entering the region of runaway condensation.

At the critical temperature, we find $y = 1$ and $x = 1$ (the latter because the surface-energy coefficient c in Equation 10 goes to zero at the critical temperature, where no distinction exists between liquid and vapor). Equation 9 would then predict a constant distribution in m_j. However, it has been pointed out(153) that in Equation 9 the factor y^j should be multiplied by a quantity $a(j)$ such that $a(j)$ is of order j and $\ln a(j)$ is of the order $\ln j$. This factor arises from the energy independent statistical weight of the cluster of size j and has been estimated(27, 28) to be of the form $j^{-\tau}$, where τ is a critical exponent that depends on the dimensionality of the cluster. Then, revision of Equation 9 gives

$$m_j = m_0 j^{-\tau} x^{j^{2/3}} y^j. \tag{12}$$

At the critical temperature the cluster distribution assumes a power law:

$$m_j \propto j^{-\tau}. \tag{13}$$

It is this power law distribution that some authors claimed to have identified in a variety of inclusive experiments(7-11, 36-40).

The finite nuclear size and the role of the Coulomb interactions(154, 155), not to speak of the shell structure of the individual fragments, set serious limitations to the applicability of the liquid-vapor equilibrium theory. Several authors have taken up these problems with different

emphases(33, 41, 44, 45, 48, 49, 124, 154, 156-160). The general approach is to assume a critical freeze-out volume within which a chemical equilibrium among all the possible fragments is established. It is in this chemical equilibrium aspect that these theories differ somewhat from the lower-energy, transition-state theory. Consequently, all of these theories require a "deus ex machina" that somehow guarantees statistical-chemical equilibrium at some stage that cannot be characterized within the theory itself.

THERMAL EQUILIBRIUM AND THE ENERGY PARTITION BETWEEN FRAGMENTS

Little attention, either theoretical or experimental, has been given to this subject(128, 130). However, its treatment in the equilibrium limit is quite straightforward. The most trivial case is, of course, that of two fragments in contact(161). The parameter characterizing the equilibrium between the fragments is their common temperature. If the specific heat of the nuclear matter is the same in both fragments, the energy of each fragment is, on the average, proportional to its mass: $x_o / (E - x_o) = A_1 / A_2$.

The fluctuations are easy to calculate:

$$\frac{1}{\sigma^2} = -\left[\frac{\partial 1/T_1}{\partial x} - \frac{\partial 1/T_2}{\partial x}\right] = \frac{1}{T^2}\left[\frac{1}{c_1} + \frac{1}{c_2}\right] \tag{14}$$

or $\sigma^2 = T^2 c_1 c_2 / (c_1 + c_2)$, where c_1 and c_2 are the heat capacities of the fragments. For a Fermi gas nucleus $c = 2a\,T$, so:

$$\sigma^2 = 2T^3 a_1 a_2 / (a_1 + a_2), \text{ where } (a \approx A/8). \tag{15}$$

The generalization to multifragmentation is also straightforward. A partition of the energy among fragments is defined by:

$$E = x_1 + x_2 + x_3 ... = \sum x_i . \tag{16}$$

Its probability is:

$$P(x_i) \propto \rho_1(x_1)\rho_2(x_2)... = \prod \rho(x_i). \tag{17}$$

The maximum probability can be obtained by searching for the stationary point with respect to variations in the x_i's with the constraint:

$$E = \sum x_i . \tag{18}$$

To do this, the auxiliary distribution is introduced:

$$P'(x_i) = P(x_i)\exp\left[-\beta \sum x_i\right] \tag{19}$$

or

$$\ln P'(x) = \sum \ln \rho(x_i) - \beta \sum x_i . \tag{20}$$

The maximum is given by:

$$\frac{\partial \ln P'(x_i)}{\partial x_i} = 0 \quad \text{or} \quad \frac{\partial \ln \rho(x_i)}{\partial x_i} - \beta = 0, \tag{21}$$

which can be written as: $1/T_i = \beta = 1/T$ or $T_i = T$. In other words, all the fragments are at the same temperature T = $1/\beta$, which can be defined as the temperature of the system.

The most probable fragment excitation energy is then approximately proportional to its mass. For the fluctuations, one can proceed by taking the second derivative to obtain:

$$\sigma_i^2 \cong T^2 c_i , \tag{22}$$

where $c_i = 2a_i T$ is the heat capacity of the ith fragment. If the fragments are many, the fluctuations are approximately uncorrelated.

ANGULAR MOMENTUM AND MULTIFRAGMENTATION As above, a collision giving rise to n fragments is considered. We assume statistical equilibrium until, beyond a critical shape or mass distribution, the fragments decouple from each other, and the equilibrium remains frozen in(162).

For simplicity, let us suppose that the critical shape is approximately spherical. Then, it is completely general to choose the z axis to coincide with the direction of the angular momentum. Also, for simplicity, let us assume that each fragment is spherical. The Hamiltonian of the system can be written as follows:

$$H = \sum H_i = \sum \left[\frac{I_x^2 + I_y^2 + I_z^2}{2\Im} + \frac{\ell_z^2}{2mr^2} + \frac{1}{2m}\left(p_r^2 + p_z^2\right) \right], \tag{23}$$

where the sum is to be carried over the fragments (the corresponding index is omitted for simplicity); I_x, I_y, and I_z are the intrinsic components of the angular momentum for a given fragment with moment of inertia $\Im$; ℓ_z is the z component of the orbital angular momentum of a fragment of mass m and distance r from the z axis; and p_r and p_z are the other two generalized momenta for the translational motion of a fragment in cylindrical coordinates. The choice of cylindrical coordinates for the relative motion has the advantage of isolating the z component of the orbital angular momentum.

The generalized grand partition function can now be calculated:

$$Z = \int \exp - \left[\sum \frac{H_i}{T} - \mu \sum (I_z + \ell_z) \right] dI_x dI_z dI_y d\ell_z dp_r dp_z, \tag{24}$$

where the constraint on the total angular momentum $I_T = \Sigma\,(I_Z + \ell_Z)$ (remember the choice of the z axis) has been introduced by means of the Lagrange multiplier μ. This guarantees that the total angular momentum will be conserved, on the average. Integration yields:

$$\ln Z = \sum \left[\ln 2\Im T + \ln 2mT + \frac{1}{2} \ln 2\pi\Im T + \frac{\mu^2}{2} \Im T + \frac{1}{2} \ln 2\pi m r^2 T + \frac{\mu^2}{2} m r^2 T \right]. \tag{25}$$

The value of the Lagrange multiplier μ is determined by the equation:

$$\frac{\partial \ln Z}{\partial \mu} = I_T = \mu \sum \left(\Im T + m r^2 T \right) \tag{26}$$

where

$$\mu = \frac{I_T}{T \sum \left(\Im + m r^2 \right)}. \tag{27}$$

Differentiation of the logarithm of the partition function with respect to $\beta = 1/T$ yields the total energy:

$$E = \frac{3}{2} nT + \frac{3}{2} nT + \frac{I_T^2}{2 \sum \left(\Im + m r^2 \right)}, \tag{28}$$

where n is the number of fragments, the first term refers to the intrinsic rotation energy, the second to the translational energy, and the third to the rigid rotation of the system at the critical shape. Again, the first two terms arise from the classical energy-equipartition theorem, while the third should be interpreted as the energy of a rigidly rotating body whose moment of inertia is

defined by the mass distribution associated with the critical shape. The intrinsic spin of each fragment can also be obtained:

$$\bar{I}^2 = 3\Im T + \left[\frac{\Im}{\sum(\Im + mr^2)}\right]^2 I_T^2. \tag{29}$$

This equation says that the fragment angular momentum arises from two contributions: the first is purely statistical, and would exist also for zero total angular momentum; the second is the share of the total angular momentum going to the fragment under consideration, dictated by the rigid-rotation condition. The two contributions are added in quadrature. From the structure of Equation 29, one can also infer that the three variances are equal: $\sigma_x^2 = \sigma_y^2 = \sigma_z^2 = \Im T$. The average for I_X and I_y is zero and the average for I_Z is:

$$\bar{I}_z = \frac{\Im}{\sum(\Im + mr^2)} I_T. \tag{30}$$

The results obtained so far allow us to describe the fragment-spin alignment through the relevant components of the polarization tensor:

$$P_{xy} \propto \sigma_x^2 - \sigma_y^2 = 0, \tag{31}$$

$$P_{zz} = \frac{1}{1 + 3\frac{\sigma^2}{\bar{I}_z^2}} = \frac{1}{1 + 3\Im T\left[\frac{\sum(\Im + mr^2)}{\Im I_T}\right]^2}. \tag{32}$$

CHEMICAL EQUILIBRIUM OR "SCISSION" MODELS? The liquid-vapor equilibrium model is improved by incorporating the Coulomb interaction, the nuclear masses, and level densities. In the Berlin model(51) all possible mass splits are considered. The fragments are randomly located inside a sphere whose radius is a free parameter. The fragments are spherical and are not allowed to be closer to each other than an arbitrarily set minimum distance. The statistical weight for the configuration is then evaluated microcanonically by distributing the available energy using the internal and collective (translational motion) degrees of freedom. Neither fragments nor the total system can carry angular momentum, although improvements din the model are under way. This statistical weight is obviously sensitive to the overall Coulomb energy of the configuration

which, in general, is very much dependent on the shape and size of the freeze-out volume. The Copenhagen model(48, 49, 112, 160, 163-165) differs in technical details. An example of the predictions of the Berlin model is given in Figure 6. At low excitation energy, the yield is dominated by evaporation residues (curve E). At intermediate energies, fission sets in (curve F). Above 600 MeV, the cracking of the nucleus into three or more pieces becomes the dominant mode (curve C).

Given the popularity of these models, it maybe worthwhile to attempt a critical analysis of them and of their assumptions. Their common assumptions are as follows: (a) Dynamical evolution leads the system to a preassigned, usually simple geometric configuration (freeze-out), within which (b) statistical equilibrium is realized among a certain class of degrees of freedom, e.g. the "fragmentation" degrees of freedom, with the notable exclusion of the container degrees of freedom.

Of critical importance in these models is the "guess" of the size and shape of the container within which the equilibrium is calculated, since the results may depend dramatically on this choice. Thus these models are not complete unless the "guess" is justified.

Perhaps Fong's model of fission is the first example of this class to appear in nuclear physics(166). In it, a "scission" configuration is chosen as two nuclei in contact. The overall statistical weight is then calculated for each asymmetry by folding the level densities of the two nuclei in contact. Then the mass yield and the fragment excitation energies can be calculated.

In models of this sort, the choice of "scission" configuration is critical. One can take the two fragments in contact with their ground state deformation or with their equilibrium deformation resulting from their mutual Coulomb repulsion. Similarly, the choice of the interfragment distance is critical. For instance, by allowing the fragment separation to go to infinity, ~150 - 200 MeV are gained that can be used to excite the fragments.

The Berlin and Copenhagen models are generalizations of Fong's model to multifragmentation. The choice of the container's shape and size is obviously very critical, and

needs to be justified. If instead of placing the fragments in a spherical container, without overlap, one chooses an elongated container, like a cigar, one diminishes the overall Coulomb energy and increases the excitation energy correspondingly. Thus, if for any fragment partition, one allows the system to choose the container shape of its liking, it will choose the one that is most stretched, with the fragments infinitely far apart. Claims about the importance of the Coulomb interaction in these models are therefore peculiar in view of the fact that the shape (spherical) is chosen without regard to the desires of the Coulomb interaction.

The Berlin and Copenhagen models differ somewhat in the way that the statistical weights are calculated. The use of the microcanonical ensemble in the Berlin model is claimed to be more correct than the canonical or grand canonical ensemble. In our opinion, the numerical effort that the microcanonical ensemble entails is in contrast with the ad-hoc assumption made for the shape and volume of the container.

These models are rather difficult to use in a realistic setting because they lack a prescription for the masses, charges, excitation energies, and angular momenta to be used. For this, they must rely on a separate dynamical calculation(98, 99, 112, 117), or they are used with the excitation-energy as a free parameter(113, 114, 118). This severe limitation is shared with other "equilibrium" models, e.g. compound nucleus theories and percolation theories.

2.5 Percolation

Some attempt has been made recently to describe nuclear fragmentation in terms of percolation theory(80-91). In this approach, the nucleus is imagined to be composed of nucleons located in a crystal lattice. In a cold nucleus all the sites are occupied. In an excited nucleus one can introduce a probability for the occupation of lattice sites. Alternatively, one can consider a lattice whose bonds have a given probability p of being broken. Depending on the value of p, one observes connected clusters of nucleons that are identified with the observed fragments. For an infinite system, there is a critical value of p above which a cluster extending throughout the

system exists (percolating cluster). In a nucleus, one can similarly define a critical value of p above which one major fragment is formed and below which many fragments are produced. The similarity of this result with the behavior of systems exhibiting second order phase transitions, such as liquid-vapor systems at the critical temperature, has led to the use of percolation theory to model these transitions. The mass distribution of the clusters near the percolation threshold is given by a power law. Thus it seems that the predictive potential of percolation theory may be limited to very generic statistical properties, which are associated with many other models as well. Nonetheless, the analysis of the experimental (and theoretical) distributions by means of percolation theory may be of benefit in discriminating between generic and specific properties of these distributions.

Campi(84, 87) has suggested the study of the charge(mass) distribution in terms of the event-by-event moments. The ith moment of the charge (mass) is given by:

$$m_i = \sum Z^i , \tag{33}$$

where the sum is extended to all the fragments of the event except the largest one. The exclusion of the largest fragment is justified as an attempt to eliminate the "percolating" cluster. An interesting combination of moments, γ_2, is given by

$$\gamma_2 = m_2 m_o / m_1^2 = \sigma^2 / \langle Z \rangle^2 + 1, \tag{34}$$

where σ^2 is the variance and $\langle Z \rangle$ is the mean fragment charge in the event.

When γ_2 is plotted versus the probability of bond breaking p, $\gamma_2 = 1$ for $p = 0$ and $p = 1$, while it goes to infinity at criticality ($p = p_{crit}$). In liquid mixtures, this gives rise to the well-known phenomenon of critical opalescence. In nuclear reactions, γ_2 should approach unity when only nucleons or very light clusters are evaporated (the heavy residue is dropped as the percolating cluster) or when the system is totally disassembled into nucleons. The experimental discovery of a variable strongly correlated with p like the excitation energy, or the number of nucleons bound in clusters Z_{bound} that might go as $1/p$, suggests that one look for a peak in γ_2 for an indication of criticality. Another suggestion for the classification of a system as below or

above criticality is to look for the correlation between Z_{max} and the event moments, as, for instance, in a scatter plot of $\ln Z_{max}$ vs $\ln(m_2/m_1)$. In such plots some people have identified two branches that have been attributed to subcritical and supercritical events(99). Experiments and theories alike have been subjected to this kind of analysis. The significance of this approach is still hotly debated and poorly understood.

2.6 Statistical Shattering

A different approach to multifragmentation was proposed by Aichelin & Hüfner(52). They envisage brittle nuclei that shatter under a sufficiently hard impact like two glass balls thrown at each other. The mechanisms of shattering of fragile material, let alone nuclei, are poorly understood. However, it has been found empirically that the resulting distribution of fragments, or shards, is rather simple, approaching a power law dependence on the fragment size. The same authors proposed to derive such a distribution from a maximum likelihood or minimum bias principle. Sobotka & Moretto(167) showed that this formulation corresponds to a saddle-point approximation to the Euler problem of number partition (i.e. all the possible ways in which an integer N can be split into integers under the constraint that their sum be N). Incidentally, these partitions, multiplied by a temperature-dependent statistical weight, appear also in some of the statistical multifragmentation theories(48, 49). Despite the lack of theoretical justification for such an ansatz, it is interesting to speculate further on possible improvements that could accommodate a modicum of physical input.

THE ROLE OF SURFACE IN NUCLEAR SHATTERING Among the many shortcomings of this approach are its lack of an energy dependence and its inability to connect the mass distributions to other observables. A possible way to introduce an energy dependence in this problem is suggested by the fact that it takes energy to produce the extra surface associated with

fragment formation. In what follows, a way is shown to evaluate the mass distribution with the constraint of a fixed amount of generated surface(53).

In a way similar to Aichelin's work(52), one defines a probability $P(m,a)$ of producing a fragment of mass a with multiplicity m. The constraints are:

$$\sum_m P(m,a) = 1 \tag{35}$$

for each a,

$$\sum_m \sum_a maP(m,a) = N, \tag{36}$$

N being the mass of the object being fragmented, and

$$\sum_m \sum_a kma^{2/3}P(m,a) = S, \tag{37}$$

S being the surface produced. The information I, associated with P modified by the constraints is:

$$I = \sum_m \sum_a P(m,a)\ln P(m,a) - K(a)P(m,a) + DmaP(m,a) + Ama^{2/3}P(m,a) \tag{38}$$

where $K(a)$, D, and A arise from the introduction of the constraints.

Minimization of the information I gives

$$P(m,a) = e^{[K(a)-1]}e^{[-m(Da+Aa^{2/3})]} = C(a)e^{[-m(Da+Aa^{2/3})]}. \tag{39}$$

Applying Eqs. 35, 36 and 37 to Eq. 39, one obtains:

$$C(a) = 1 - \exp\left[-(Da + Aa^{2/3}\right] \tag{40}$$

$$\sum_a \frac{a}{\exp[Da + Aa^{2/3}] - 1} = N \tag{41}$$

$$k\sum_a \frac{a^{2/3}}{\exp[Da + Aa^{2/3}] - 1} = S. \tag{42}$$

Summing $P(m,a)$ over m, the mass distribution is:

$$P(a) = \frac{1}{\exp\left[Da + Aa^{2/3}\right] - 1}. \tag{43}$$

Notice the striking similarity of this equation and Equation 9 derived for the droplet size in liquid-vapor equilibrium. By solving Equations 41 and 42 simultaneously for D and A and substituting the values so obtained in Equation 43, one arrives at the desired distribution. As an example, Figure 7 shows the resulting mass distribution assuming $N = 200$. The three curves

correspond to $\Delta S/S_0$ = 0; 0.2; -0.2, where S_o is the unconstrained surface (A = 0). One can readily see that, by requiring more surface area ($\Delta S/S_o$ = 0.2), one favors the formation of light fragments and by requiring less surface area ($\Delta S/S_o$ = -0.2) one enhances the production of heavy fragments.

It remains to be established how much energy is invested in surface production in any given reaction. This may not be easy to determine. However, it may be possible to infer this from the determination of the total fragment kinetic energy in the center of mass of the fragmenting nucleus. From the virial theorem, a relation must exist between the average total kinetic energy and the average potential energy, which is approximately proportional to the average produced surface.

3. DYNAMICAL THEORIES

Extensive efforts have been made to describe nuclear reactions involving many shape degrees of freedom in terms of dynamical theories.

The prototype of these theories is Time Dependent Hartree Fock theory(TDHF)(168, 169), which has been applied with mixed success to low energy, heavy-ion collisions (fusion and deep inelastic scattering). In this treatment, the mean field and its time dependence are dealt with in a consistent manner. However, since the nuclear wave function remains a single Slater determinant throughout, nucleon-nucleon collisions, which represent the main source of dissipation, are not described. Attempts to include collisions have proceeded along a semiclassical line. The collisionless Vlasov equation has been augmented with a collision (Boltzmann) term. The incorporation of nuclear forces of the Skyrme type, plus an empirical Fermi potential trying (with uncertain success) to implement the Pauli principle, has lead to a series of dynamical theories(55, 57-65), differing from one another both in the details of the ingredients and in the methods of solution.

These theories are variously labeled Boltzmann-Uehling-Uhlenbeck (BUU), Landau-Vlasov, and Boltzmann-Nordheim-Vlasov (BNV). There are some fundamental short comings in them. The Pauli principle, as an example, is not rigorously respected. Another shortcoming is their inability to accurately describe the statistical decay in the long time limit. This has been remedied, on occasion, by terminating the dynamical calculation at a suitable time, after energy relaxation has occurred, and continuing the calculation with a compound-nucleus-decay code(111, 115, 116) or a multifragmentation code(93, 96-99, 112-114, 117, 118, 170).

A further problem in the dynamical theories is their lack of treatment of fluctuations. This may not be too serious if the dynamics is well behaved, but, at least in principle, it may become important if the system encounters a region of instability where fluctuations, which are averaged out in the mean field, would amplify and dictate the evolution of the system thereafter. A major development in this direction is the theory by Ayik and Gregoire(66, 67) ddin which the time dependent field is decomposed into an average part (mean field) and a fluctuating part, in the spirit of the Langevin approach. The numerical implementation of this theory is in progress(67-72).

If dynamics rather than statistics prevails in nuclear reactions leading to multifragmentation, the possibility arises that the system encounters in its dynamical evolution regions of instabilities that may lead to multifragmentation. We shall consider here some of these instabilities.

3.1 Instabilities: Volume and Surface

VOLUME INSTABILITY One instability that has been considered as a possible initiator of multifragmentation is the spinodal instability, associated with the transit of a homogeneous fluid across a domain of negative pressure. In this region a single homogeneous phase is unstable, and the system breaks up into liquid and gas phases. Typically, this occurs by the formation of liquid droplets embedded in a saturated vapor. There is a misconception that the droplet-size

distribution is given by a power law (see Equation 13), but this is not so in general. The droplet-size distribution depends on the process of nucleation, which in turn may depend on a variety of intrinsic and extrinsic factors, all, in general, leading to a non-equilibrium distribution. In the case of homogeneous nucleation, the distribution is determined by the time constants of the unstable modes, which are totally unrelated to equilibrium. In fact, the droplets observed in the wet vapor, obtained in the spinodal breakup, are in their turn unstable towards coalescence into bigger drops, and eventually into liquid bulk. Since the spinodal instability can occur in an infinite system, it can be called a bulk, or volume instability.

SURFACE INSTABILITIES Here we want to consider another class of instabilities that may play an important role, if not a dominant one in multifragmentation, namely instabilities of the Rayleigh kind(171) that depend on the presence of a surface endowed with surface tension.

These instabilities have been observed(172) in heavy-ion collisions simulated using the Boltzmann-Nordheim-Vlasov (BNV) equation. In a nearly symmetric head-on collision, a "disk" develops as a result of the side-squeezing of nuclear matter, whose thickness decreases and diameter increases monotonically with increasing bombarding energy. When the disk becomes sufficiently thin, it breaks up into several fragments of a size commensurate with the thickness of the disk.

Some of these features are shown in Figures 8 - 10 for head-on collisions of two ^{90}Mo nuclei at three bombarding energies and at two extreme values of the incompressibility constant K. For K = 540 MeV and the lowest bombarding energy, a thick disk forms and some mottling develops at its maximum extension (incipient fragment formation). However, the mottling heals and the disk falls back to a more or less spherical blob. At higher bombarding energy, the disk becomes thinner, with a larger diameter than in the previous case. As the collision progresses, the mottling appears and develops rapidly into a crown of many fragments, each of approximately the same size, that slowly separate because of the residual kinetic energy of the disk and their

mutual Coulomb repulsion. In some cases, two or more of these proto-fragments coalesce into a larger fragment (see, for example, Figure 9, column 3).

To cover the range of nuclear incompressibility currently believed appropriate for nuclear matter, the calculations were repeated for $K = 200$ MeV. At 55 MeV/u, a thin disk forms and fragment formation occurs, in contrast to the situation at high incompressibility in which fragment formation does not occur at this energy. At higher bombarding energies, fragment formation is observed for both values of K. However, for the high incompressibility cases, the disks are much sharper, and the mottling and fragment formation stand out more clearly. Similar calculations have been performed for a range of central impact parameters and entrance channel mass asymmetries with similar results. The origin of the instability leading to multifragment formation is discussed below.

3.2 Metastability of a Sheet of Liquid

The overall appearance of the disk fragmentation strongly suggests that it is caused by surface instabilities. More precisely, the system seems to escape from the high surface energy of the disk by breaking up into a number of spherical fragments with less overall surface. Thus, fragment formation, in this picture, depends solely on the presence of a surface energy term. (In the static limit, the BNV model reduces to a semiclassical approximation to the Hartree Fock model, which can reproduce the nuclear masses throughout the periodic table and thus expresses a good surface energy.) Multinucleon correlations, which are commonly thought to be essential for fragment formation, are not actually necessary beyond their macroscopic manifestation through the surface energy. Incidentally, the very same observation can be made for volume instabilities.

The observed instability may be akin to the Rayleigh instability(171) of a cylinder of liquid. The cylinder is unstable with respect to small perturbations of wave length $\lambda \geqq 2\pi R$, where R is

the radius of the cylinder. But, is a disk of liquid, or more generally, a sheet of liquid truly unstable?

If we assume sharp non-interacting surfaces (no surface thickness, no surface-surface interaction), a sheet can be metastable with respect to break-up into a layer of cylinders or spheres (see Figure 11). The onset of metastability for both cases is easily calculated. On a sheet of thickness d let us identify stripes of width λ. These stripes can favorably collapse into cylinders when the surface area of a stripe (top + bottom) is greater than the surface area of the cylinder of equivalent volume. This can be easily shown to occur for $\lambda \geq \pi d$. Similarly, if the sheet is tiled with squares of side λ, the squares can collapse into spheres when: $\lambda \geq (3/2)\sqrt{2\pi}d$.

These conditions refer to metastability and not necessarily to instability, since there may be a barrier that prevents the sheet from reaching the more stable configurations illustrated above, and indeed there is. A sheet with sharp, non-interacting surfaces is stable to small perturbations of all finite wavelengths, and becomes indifferent to perturbations of infinite wavelengths. Clearly, any wave of infinitesimal amplitude A increases the surface area of the sheet, independent of the sheet thickness, since, in the limit of infinitely sharp surfaces, the surfaces do not know of each other, until they touch (see Figure 11). The dimensionless surface energy increase can be trivially shown to be:

$$\Delta V_s \approx \frac{2\pi^2}{\lambda^2} A^2 \quad + \text{higher order terms,} \tag{44}$$

where λ is the wavelength of the perturbation.

On the other hand, the systems portrayed in Figures 8 -10 develop what appears to be a genuine instability. Perhaps, the system, which has plenty of energy, simply jumps the barrier. But, there is another, more likely possibility.

3.3 Instability of a Sheet of Liquid and Surface-Surface Interactions

Nuclear surfaces are not sharp but diffuse, and they interact with each other through a finite range called also the proximity force(173), $\Phi(s)$, where s is the distance between surfaces. Let us now calculate the incremental proximity energy of a sheet subjected to a perturbation of wavelength λ and small amplitude A. The dimensionless proximity interaction is

$$V_P = \frac{2}{\lambda}\int_0^{\lambda}\Phi(s)dx \sim \frac{2}{\lambda}\left[P(\lambda)+Q(\lambda)A^2\right], \tag{45}$$

where

$$P(\lambda)=\int_0^{\lambda}\Phi_0(x)dx \quad \text{and} \quad Q(\lambda)=\int_0^{\lambda}\Phi_2(x)dx \tag{46}$$

with $s = d + 2A\sin kx$, Φ_0 and Φ_2 being the zero-order and second-order coefficients of the Taylor expansions of $\Phi(A,x)$ about $A = 0$, and $k = 2\pi/\lambda$.

The overall energy increase, including the term in Eq. 44, is

$$\Delta V = A^2\left[\frac{2\pi^2}{\lambda^2}+\frac{Q(\lambda)}{\lambda}\right]. \tag{47}$$

Instability occurs when the coefficient of A^2 is zero or negative. Thus, the critical wavelength for the onset of the instability is given by the equation: $\lambda_c Q(\lambda_c)+2\pi^2 = 0$. Any perturbation with $\lambda > \lambda_c$ is unstable, namely it will grow spontaneously and exponentially. Using for the proximity potential the numerical expression given by Blocki et al.(173), we obtain

$$\lambda_c = 1.10b\exp[2d/3b], \tag{48}$$

where b is the range of the proximity interaction.

When the thickness d of the sheet becomes much greater than the range of the proximity interaction, the critical wavelength tends to infinity. This is the trivial result that was mentioned above for infinitely sharp surfaces. However, when the thickness of the sheet becomes comparable to the proximity range b, the critical wave-length decreases very rapidly.

3.4 Application to Simulated Nuclear Collisions

The considerations made above are purely static, while the BNV calculations deal with the full dynamical problem. For instance, the thickness and radius of the disk develop in time,

though eventually they become nearly stationary, as if a turning point were reached. In other words, there is an interplay between the rate of growth of the instabilities and the underlying disk dynamics. Therefore, it may be difficult to interpret the details of these phenomena without incorporating specifically the time evolution of the disk. Furthermore, Equation 48 gives only a lower bound for the instability range. Clearly the disk must become thin enough to allow the critical wavelength to fit comfortably within the disk diameter. But which wavelength, if any, actually determines the collapse of the disk? The answer cannot be determined from the instability considerations made above. Rather, it depends on how fast the instability develops. For instance, Rayleigh showed that, for a cylinder, the instabilities grow exponentially, and that the growth is fastest for $\lambda = 9.11R$ (171). This result has been obtained assuming irrotational flow and no viscosity. However, it is known that viscosity can play an important role in this respect.

In contrast to an infinitely extended sheet, the finite size of the disk may introduce interesting effects. The nearly symmetric patterns of the fragments suggest the presence of stationary waves determined by the boundary conditions of the disk edge. In fact, the association of these patterns with the nodal pattern of cylindrical harmonics is very tempting.

The role of incompressibility in these calculations has also been studied. The upper value of the incompressibility parameter essentially prevents any compression (and expansion) from occurring. Thus, it should isolate surface effects from those associated with compression and expansion. The overall comparison between the two extreme cases shown in Figures 9 and 10 suggests that thinner and sharper disks are formed at high incompressibility. In fact, at the highest bombarding energy (100 MeV/u) investigated, the low incompressibility calculation shows a coarse, fuzzy disk where fragments are seen to form within its thickness in a volume-like process. This may indicate the appearance of a volume (spinodal) instability.

3.5 Onset of Surface Instabilities

What triggers the instabilities that are visible in the BNV calculations? There are at least two possibilities, not mutually exclusive. (a) The dynamics of the collision may excite some higher order modes that later become unstable. (b) The algorithmic noise, mostly associated with test particle number, may trigger these same modes.

Let us consider these possibilities in order.

It is quite possible, and very likely, that some higher order modes are excited by the very dynamics of the collision, provided that these modes reflect the symmetry of the equation. In a head-on collision there is cylindrical symmetry, so one should look for cylindrically symmetric eigenmodes, which for a disk would be a combination of suitable cylindrical harmonics. The symmetric distribution of fragments in the calculation is suggestive of the nodal patterns of cylindrical harmonics.

If the modes of cylindrical symmetry can be excited by the dynamics, the "azimuthal modes" must be associated with the spontaneous breaking of the symmetry arising from the underlying instability and triggered by algorithmic noise. Algorithmic noise gives the system the chance to take advantage of instabilities, to break symmetries, etc. However, its power spectrum is in general unknown, probably machine dependent, and certainly unphysical. Consequently, one could argue that such noise is good only to show the instabilities but not to generate realistic distributions.

Theoretical efforts have been made to introduce truly physical fluctuations(66-72). However, is physical noise really needed? It depends. For instance, for the Rayleigh instabilities in a cylinder, the outcome, namely the breaking up of the cylinder into droplets, is practically independent of the noise that triggers the instability. This independence results because there is a maximum instability at a given wavelength that dominates exponentially in time over all the other wavelengths.

There are other instabilities whose onset is practically independent of the noise that triggers them. This is the case of resonant instabilities. For instance, a violin string struck by a bow sets

up a stick-slip instability that always produces the same note, independently of the violinist. Of all the frequencies contained in the noise, only the resonant frequencies survive and have a chance to be amplified by the instability. The others are cancelled by negative interference.

3.6 Donuts and Bubbles

Besides disks, other exotic shapes have been predicted(174) for hot nuclei and recently observed in BUU or BNV calculations(172, 175-179). These shapes are donuts or toroids (see Figure 12), and bubbles. Both of these shapes should be subject to surface instabilities. A torus can be imagined as a cylinder bent so that its two bases are united. Consequently, it should manifest the classic Rayleigh instability, whose critical wave-length is given by $\lambda_{crit} = 2\pi R$, where R is the radius of the cylinder. This is the shortest unstable wave-length. Therefore, to make a torus critically unstable, we must make it such that its internal circumference degenerates into a point. (This shape is generated by taking a circumference and rotating it about a straight line tangential to it.) Any wider torus or donut with a finite hole should be unstable, and will spontaneously pinch off, most likely in just a few points. This is a serious instability, but it should not give rise, on its own, to very many fragments.

A bubble, on the other hand, behaves more like a sheet, and is indeed subject to the sheet instability discussed in connection with the disk. Since a bubble, as a sheet, must rely on proximity to become unstable, it will retain its surface stability until its thickness is of the order of the surface-surface interaction range. Thus, a rather thick-walled bubble will not be susceptible to surface instabilities over a very broad range of its inner sphere radius. BNV calculations for very heavy systems at low bombarding energies show the formation of a thin bubble(176) that bursts under the action of the sheet instability(172).

3.7 Coulomb-induced Instabilities and "Stabilities" in Liquid Spheres and Bubbles

It seems intuitive that the Coulomb field should act as a disruptive force in nuclear reactions involving very heavy nuclei. Its role has been heavily underscored by Gross et al in their multifragmentation model(180). The instabilities caused by the Coulomb field in a liquid sphere illustrate the point very dramatically.

LIQUID SPHERE The eigen frequencies of a liquid, incompressible, nonviscous sphere with irrotational flow are given by

$$\omega'^2 = n(n-1)(n+2) \tag{49}$$

where ω' is the frequency given in units of $(c_s/\rho R^3)^{1/2}$ (c_s is the surface energy coefficient and ρ and R are the density and radius of the sphere, respectively) and n is the order of the spherical harmonic under consideration. Since all these frequencies are real, all the modes are bound.

The introduction of a charge (uniformly distributed throughout the volume of the sphere) changes the frequencies as follows:

$$\omega'^2 = n(n-1)[(n+2)-4x] \,, \tag{50}$$

where $x = E_{Coul} / 2E_{surf}$ -- defined in terms of the Coulomb energy E_{Coul} and the surface energy E_{surf} of the sphere -- is the well-known fissility parameter.

The Coulomb field destabilizes a number of modes. For $x < 1$ all the modes are stable. At $x = 1$, the frequency ω' goes to zero for $n = 2$. This is the onset of quadrupole instability, or of the fission instability. For $x > 1$, progressively higher modes are destabilized. The last unstable mode is: $n_{last} = \mathrm{int}(4x - 2)$.

One would think that when many modes are unstable, the most unstable mode would remain the lowest mode $n = 2$ or the fission mode. This is, curiously, not the case. For instance, for $x = 3$, $n_{last} = 10$, $n_{max} = 7$ and for $x = 4$, $n_{last} = 14$, n_{max} is between 9 and 10. So, a highly charged sphere will not merely fission, it will break up in many droplets through an instability associated with a high multipole mode.

One might question whether this sort of process is relevant to nuclear multifragmentation. At first sight one would think not. In fact, by fusing the heaviest nuclei available, one barely reaches $x \sim 1.5$, which would give: $n_{last} = 4$. However, this assumes that the fused nucleus is cold. In typical heavy-ion reactions one can reach large excitation energies and temperatures. At high temperatures the surface energy decreases and the fissility parameter x increases. Therefore, it is conceivable that this type of Coulomb instability may have some relevance to multifragmentation.

BUBBLES The normal modes of a bubble can be divided into two classes. The first class consists of radial modes for which the bubble shape is modulated by a spherical harmonics mode, and the thickness of the bubble remains uniform throughout. These modes are destabilized by the Coulomb field very much like those of a liquid sphere. (The equation of the eigen frequencies is the same as Equation 50 with the provision that x is redefined suitably through the redefinition of E_{Coul} and E_{surf}). Since x is smaller for a bubble than for the corresponding spherical drop, these instabilities are not likely to play any role.

The second class of modes, which we call "crispation modes", involves a thickening and thinning of the liquid layer. In the limit of sharp surfaces (no surface-surface interaction) and in the absence of the Coulomb field, all these modes are stable except the dipole mode, which is indifferent. The "inner" sphere of the bubble in this mode is free to drift with respect to the outer sphere, which leads eventually to the puncturing of the bubble. The introduction of surface-surface interaction makes the crispation modes potentially unstable through the "sheet instability" described above.

On the other hand, the Coulomb field tends to stabilize these modes. This is seen quite simply for the dipole mode. In this case one can write the Coulomb energy as that of the uniformly charged outer sphere with a negative charge in the center of the inner sphere such that the resulting net charge is that of the bubble. This energy increases quadratically with the

distance between the centers of the two spheres, thus stabilizing the mode. Similarly, the Coulomb force resists any attempt to concentrate the charge in "clumps" distributed on the surface of the sphere, as required by the higher modes.

4.0 EXPERIMENTAL EVIDENCE

4.1 The Hot Environment of Multifragmentation

Before serious attempts were made to characterize multifragmentation, very dramatic features had already been discovered in heavy-ion collisions at intermediate energy. Two of these appear very relevant to our discussion: incomplete momentum transfer, or incomplete fusion, and extremely high thermalization of the entrance channel kinetic energy. We discuss them here in some detail because of their importance in describing the overall environment in which the process of multifragmentation is embedded, and for the role that they have played in the characterization of the multifragmentation sources.

INCOMPLETE MOMENTUM TRANSFER, INCOMPLETE FUSION, AND FIREBALL REGIMES A large literature exists on incomplete momentum transfer. Perhaps, the experimental approach most widely used has been the determination of the fission-fragment folding angle(127, 181-192) in reactions induced by an intermediate energy heavy ion on a rather fissionable target, like Au, Th or U. The distribution of folding angles typically shows two peaks, one close to 180°, characteristic of grazing collisions, and another, very broad, at a smaller angle. At low bombarding energies, the latter corresponds to "full momentum transfer" indicating complete fusion. At higher energies, the same peak can be accounted for only in terms of an "incomplete momentum transfer", the remaining momentum presumably being carried away by pre-equilibrium emission, or by an incomplete fusion spectator. These two alternatives are not mutually exclusive. However, the incomplete fusion picture has received abundant, though only semiquantitative, experimental support and has become, for better or for worse, a standard

schematic representation of the reaction mechanism at intermediate energies(53, 127). Recent experiments have partitioned the velocity distribution of fusion-like products into individual incomplete fusion channels(188, 191, 193) yielding a wealth of data on the reaction process.

At somewhat higher energies, the incomplete fusion peak in the folding angle distribution disappears(185, 188) partly because of the onset of multifragment production, partly because fission seems to compete less effectively with massive evaporation(187, 189, 190). At even higher energies, incomplete fusion is substituted by the fireball formation(13, 194). In this region, contrary to what happens in incomplete fusion, where the larger partner picks up the occluded piece of the smaller partner, the two occluded regions form a clump of hot nuclear matter, the fireball, that decouples from the colder donors, or spectators. A diagram illustrating the approximate domains of the various processes is shown in Figure 13.

This simple picture leads to the prediction that, in the incomplete fusion regime, a "hot" compound nucleus is formed and then proceeds to decay in the usual fashion, while in the fireball regime, the fireball disassembles completely into nucleons and small aggregates, like α particles, while the spectators remain 'rather' cold. The minimum excitation energy of the spectators, in both cases, is proportional to their excess surface. The boundaries of these regimes have not been precisely established. As we discuss below, they depend rather dramatically not only upon impact parameter but also, and perhaps overwhelmingly, on the entrance channel mass asymmetry.

REVERSE KINEMATICS AND BINARY COMPLEX FRAGMENT EMISSION The folding angle procedure can be generalized to complex fragments produced in reverse kinematics reactions. This approach was made possible by the availability of intermediate energy heavy projectiles, for instance at the Bevalac, in conjunction with the observation of complex fragment emission. An invariant $(v_{\parallel},v_{\perp})$ plot of the complex fragment cross section permits, for instance,

the visualization of the incomplete fusion objects, which, by relaxing into compound nuclei, could undergo binary decay by emitting complex fragments.

At low energies, and for very asymmetric entrance channels, sources of complex fragments can be identified directly by inspecting the invariant cross sections for individual atomic numbers (see Figure 14). The presence of Coulomb rings allows one to verify that the fragments are emitted by the relaxed binary decay of a source with compound nucleus velocity(21). Coincidence measurements(22, 105, 195, 196) verify that the reaction proceeds via the binary decay of a compound nucleus.

With a moderate increase of bombarding energy, always in very asymmetric systems, one still observes sharp Coulomb circles, but centered at a velocity characteristic of incomplete fusion(103, 104, 106, 197). Thus, in these reactions three fragments are produced: an incomplete fusion spectator and a pair of fragments arising from the compound nucleus decay of the incomplete fusion product. The great separation in velocity space between the spectator and the binary decay products illustrates the heterogeneity of this three-fragment decay. More symmetric entrance-channel systems at rather low energy, like 18 MeV/u ^{139}La + ^{64}Ni, show very poorly defined Coulomb rings, stretched along the direction of the projectile motion(198). However, if in the "binary" coincidence data, gates are set on the source velocity of the two fragments, sharp Coulomb rings are recovered. The lesson is simple. In more nearly symmetric systems, incomplete fusion occurs with a continuum of mass transfers leading to a continuum of incomplete fusion products with a corresponding range of masses, charges, excitation energies, and source velocities.

Figure 15 illustrates how the incomplete fusion process evolves as a function of entrance channel mass asymmetry and of bombarding energy. A global overview of the reactions ^{129}Xe/^{139}La + ^{12}C, ^{27}Al, ^{48}Ti, ^{64}Ni/^{nat}Cu at a variety of bombarding energies can be obtained by examining the two-fold complex fragment coincidence data(108, 199). The source velocity was reconstructed on an event-by-event basis from the velocities and the masses of the detected

fragments. In Figure 15, contour plots in the plane of the source velocity (normalized to the beam velocity) and the total detected charge, are presented for two-fold events at seven different bombarding energies and four entrance-channel mass asymmetries. The 18 MeV/u data(105, 198) represent a low energy benchmark, since at this energy the reaction mechanisms are better understood.

Figure 15 the first column corresponds to the most asymmetric system $^{139}La/^{129}Xe + ^{12}C$. This system, which has relatively low available energies in the center of mass, presents a very simple pattern. At 18 MeV/u, the source velocity distribution peaks at the value expected for complete fusion, which corresponds to the solid line, and the total charge detected is equal to the total charge of the system ($Z_P + Z_T = 63$). In this case, complete fusion has occurred and primarily neutrons have been evaporated.

When the incident energy increases, the distributions move toward a higher source velocity and a lower total detected charge. The higher velocity corresponds to the onset of incomplete fusion, because, in reverse kinematics, when the projectile picks up less mass from the target, it is slowed down to a lesser degree. A similar description applies to the somewhat heavier ^{27}Al target. The only difference is that, at the higher excitation energies, evaporation is more extensive, and the detected charge becomes smaller than that of the primary compound nucleus.

The pattern observed for the heavier targets ^{48}Ti,^{64}Ni and ^{nat}Cu is more complicated. At 18 MeV/u, a ridge is seen going to lower total charge as the source velocity increases. This pattern is expected when a range of incomplete fusion processes are present. As the incident energy and the excitation energy available in the reaction increase, the pattern shifts towards lower Z values and rotates because of secondary evaporation. The competing role of incomplete fusion and charged particle evaporation is illustrated schematically in Figure 16. The thick line represents the range of primary products from the incomplete fusion process, prior to evaporation (this should be approximately the same at all bombarding energies). The dashed lines to the left show the total charge after evaporation as the bombarding energy (excitation energy) is increased. Since for

each bombarding energy the maximum excitation energy is always for complete fusion, the dashed line should rotate clockwise as the bombarding energy increases. A vertical line means that the charge gained in the incomplete fusion process is equal to the charge lost by evaporation. This is roughly the case for the 31-MeV/u reactions. Above this energy, for each charge unit transferred from the target to the projectile, more than one charge unit is lost on the average by evaporation.

The correlation between the measured charges of the two fragments is also instructive, since it allows one to determine whether the decay mechanism is predominantly binary or multibody. If the final state is binary, the contour plots should be dominated by a band of events peaking at $Z_1+Z_2 \approx Z_{source}$. If the exit channel is actually multibody, with one or several fragments not detected, the events should fall below the line.

The measured Z_1 - Z_2 correlations for the systems studied are shown in Figure 17. The pattern observed for the $^{139}La/^{129}Xe + ^{12}C$ reaction is very clear. For this very asymmetric system, the contour plots show a distinct band with a total charge close to the sum of the projectile and target Z values, thus illustrating the binary nature of the process. Evaporation causes the band to broaden and shift toward smaller total charge as the incident energy increases. For the ^{27}Al target, this effect becomes more important, and, at the highest incident energy, the scattering of events indicates that a large fraction of the "binary" events are in fact multibody events in which only two of the fragments have been detected. This pattern is even more pronounced for the heavier targets, where the two-body band disappears completely by 35 MeV/u. Figures 16 and 18 illustrate the dramatic changes observed in the data with increasing bombarding energy and entrance-channel mass asymmetry, as the reaction evolves from primarily two-body to multibody.

HIGHLY THERMALIZED SOURCES The advent of large 4π neutron detectors(200-203) allowed one to determine the extent to which the kinetic energy available in the entrance channel

is thermalized. As most of the neutrons in a given reaction are expected to be emitted by evaporation, the number of neutrons associated with that reaction should be a measure of the energy that has been thermalized(202).

A strong correlation between the fission-fragment folding angle (and thus the momentum transfer) and the neutron multiplicity M_n has been demonstrated. Low(high) values of M_n correspond to large(small) folding angles(204). These studies showed that M_n is strongly correlated with impact parameter, the highest multiplicities resulting from the most central collisions. The mean neutron multiplicity increases over a large range of momentum or mass transfers which indicates, on the one hand, the large extent to which energy relaxation occurred, and on the other, the approximate validity of the incomplete fusion model.

The influence of bombarding energy on the maximum thermal energy deposited has been studied for the systems $^{40}Ar + ^{197}Au$ and ^{232}Th in the energy range 27 - 77 MeV/u(205). With this rather light projectile, M_n increases slowly over this wide bombarding energy range, which indicates a saturation in the energy deposition. As the bombarding energy increases, preequilibrium processes carry away a larger fraction of the available energy.

At a fixed bombarding energy, the maximum thermal energy deposited for any given projectile depends strongly on the projectile mass(205, 206). For central collisions of the 29-MeV/u $^{208}Pb + ^{197}Au$ reaction, on average 78 neutrons are emitted(207). This represents almost one third of all the neutrons in the system and is a much larger fraction than is observed for the lighter ^{40}Ar and ^{84}Kr projectiles at similar beam energies (see Figure 18). For the largest values of M_n, the fragment yield decreases in an exponential fashion with increasing mass, which suggests that the entire Pb + Au system disassembles into a large number of nucleons and small fragments.

For peripheral collisions, quasielastic or dissipative collisions are observed in the 29-MeV/u $^{208}Pb + ^{197}Au$ reaction. The most peripheral collisions lead to the formation of projectile residues, whereas sequential fission of the projectile residue is observed for somewhat less

peripheral collisions. A plot of the invariant cross sections in the plane of rapidity versus perpendicular momentum shows striking ring patterns(208) very reminiscent of those shown in Figure 14. The angular and energy distributions of the fragments indicate a significant spin alignment of the fissioning nuclei. Such simultaneous measurements of the dissipation of kinetic energy into heat and the transfer of relative angular momentum into intrinsic spin provide important insight into the heavy-ion reaction mechanism.

The simultaneous measurement of the neutron and light charged particle multiplicities for the 28.2 MeV/u $^{136}Xe + ^{209}Bi$ reaction gave evidence for dissipative collisions. For all degrees of dissipation (all values of M_n) the velocity distributions of the light charged particles were characteristic of sequential emission following binary collisions(203).

4.2 Sources of Multifragmentation: Experimental Observables and Key Variables

Within a given model, it is easy to identify those variables that are most useful in describing a given event. In a compound nucleus description, for instance, the obvious relevant variables are mass, charge, excitation energy and angular momentum. Experimentally, the problem is complicated by the difficulty in directly determining these variables, and sometimes by the fact that different theories suggest different variables. Therefore, the choice of variables is often made either by the empirical evidence of their relevance, or by a compromise between what is desired and what is available. All of these difficulties are present in multifragmentation, where there is still much confusion regarding the significance of some empirical variables.

Perhaps some progress could be made in this direction by asking how one might identify and characterize the sources involved with the production of intermediate mass fragments. The space-time extension of the sources produced in heavy-ion collisions can be determined by particle-particle interferometery using a technique similar to that of Hanbury Brown & Twiss(209). Fragment-fragment correlations could also be important in characterizing a multifragment event as sequential or simultaneous. Correlations between particles arising from

the decay of different unbound states in primary fragments have also been used in attempts to determine the (thermal) population of excited states and the temperature of the source(210-212).

The discussion in the previous sections suggests that the center-of-mass velocity of a multifragmentation event could be an interesting variable from which one could attempt to calculate the excitation energy of the source, as was done for binary events. In addition, the neutron multiplicity, or even the charged particle multiplicity could be used to infer the approximate excitation energy of the intermediate system. Alternatively, or complementarily, the total charge bound into fragments, Z_T or Z_{bound} could be useful in setting approximate gates on the excitation energy. In the next section, we give examples of experiments that have been analyzed in terms of one or more of these variables.

PARTICLE-PARTICLE CORRELATIONS AND SPACE-TIME EXTENSION OF THE SOURCE Amplitude interference measurements have been used to determine stellar sizes, but they are complicated by contributions from atmospheric distortions. A major improvement was the development of two-photon intensity interferometry by Hanbury Brown & Twiss(209) (HBT), which measures the two-photon correlation function for incoming coincident photons as a function of their relative momentum. This technique can be generalized to other pairs of identical particles(129) like pions, protons, and neutrons. Pion interferometry has been used extensively to study the pion source characteristics in relativistic heavy-ion collisions. Two-proton interferometry has also been used to study the emission sources formed in intermediate energy heavy ion collisions(129) and the evaporation lifetime of hot compound nuclei(213, 214) or target-like residues(215).

Two particles, emitted at small relative momenta from an excited nuclear system, carry information about the space-time characteristics of the emitting source. A typical analysis assumes a Gaussian source distribution for the emitted particles in terms of size and lifetime. If one assumes that the source lifetime is zero, one can determine the emission source size by fitting

the correlation function with the radius of the source distribution as a free parameter. Extensive two-proton correlations have been measured. In Figure 19, extracted source radii are plotted versus the average velocity of the coincident proton pair for variety of light heavy-ion-induced reactions on ^{197}Au and ^{nat}Ag targets(216). For energetic protons, the extracted source radius agrees with the radius of the projectile used in the different reactions. However, a recent systematic study, at 30 MeV/u, found that the source radii were independent of the size of the target and typically exceeded the radius of the compound nucleus(217). These results and other work(218) have led some authors to argue about the relevance of this method of extracting information about the size of the emitting system.

SEQUENTIALITY AND FRAGMENT-FRAGMENT CORRELATIONS One of the elusive goals in this field has been to find an experimental signature that would distinguish between true prompt multifragmentation and a series of sequential binary decays. Lopez & Randrup(136) looked for a difference between these two alternatives by studying the Coulomb trajectories of the fragments in the early stage of the distintegration process. Their analysis of the momentum distribution of each event, using the sphericity tensor, shows that sequential decay exhibits an elongated shape, whereas simultaneous breakup leads to a fairly spherical shape. Several experimentalists have applied this event-shape analysis technique to multifragment products of heavy ion reactions. For the 35 - 85-MeV/u ^{40}Ar + ^{51}V reactions, the data yield an elongated shape at the lowest bombarding energy, indicating that the fragments result from sequential decay(219). At higher energies, more spherical shapes are observed intermediate to the sequential and simultaneous limits. A similar analysis(220) of the 25 - 85-MeV/u ^{40}Ar + ^{27}Al reactions shows that a compound nucleus is formed in an incomplete fusion process and that it decays via isotropic emission at all incident energies, although no heavy residue is left above 36 MeV/u.

The closer together in time that the fragments are emitted, the stronger their Coulomb repulsion. This interaction affects the shape of the two-fragment correlation functions at small

relative momenta. Recently, the technique of intensity interferometry has been applied to multifragment decays(221), and the two-fragment correlation functions have been measured(222) for the 35-MeV/u ^{36}Ar + ^{197}Au reaction. A deep minimum at $q \sim 0$ MeV/c is observed because of the repulsive final-state Coulomb interaction between the emitted fragments (see Figure 20). Comparison with three-body trajectory calculations indicates average fragment-emission times of 100 - 200 fm/c. Such an emission time is neither very large nor very small and thus is compatible with the picture of interacting sequential decays.

The time-scale of the emission process can be studied by constructing a correlation function of the the relative velocity and relative angle for three body decays. For the 60 MeV/u ^{22}Ne + ^{197}Au system, these three-body events appear to be produced by the decay of the compound system with high recoil velocity and thus high excitation energy ($E^* \sim 4$ MeV/u). An analysis of these events in their center of mass shows that the fragments are produced in a two-step process with a time lag between the two binary decays short enough to allow for noticeable mutual interaction between the fragments after their separation(223).

Four-body events produced in the 43 MeV/u ^{84}Kr + ^{197}Au reaction appear to be associated with intermediate impact parameters, and thus suggest a dissipatitive collision producing very hot ($T \sim 6$ MeV) projectile-like and target-like nuclei(224). The slow moving target-like nucleus is observed to fission and to emit an intermediate mass fragment (IMF) preferentially in the direction of the projectile. This process differs from low-energy deep inelastic reactions, in that full damping is not reached, and the angular distibutions of the emitted IMFs are not isotropic. For interactions corresponding to full damping, large primary fragments are not likely to survive, since the available energy is larger than the energy needed to vaporize the whole system.

POPULATION RATIOS AND TEMPERATURE For systems in thermal equilibrium, the ratio of the populations of the excited and ground states can be written as:

$$R \propto \exp\left[\frac{-\Delta E}{T}\right] \tag{51}$$

where ΔE is the energy gap between the ground and excited states, and T is the nuclear temperature. The temperature of the system can be extracted if one measures the ratio of populations R and one knows ΔE. Two conditions must be fulfilled to make this method reliable: (a) the emitting system must be in thermal equilibrium, and (b) the observed products must be primary products.

This idea has been applied to γ-ray emission from bound states(225) and to particle emission from unbound states(211, 212, 226-228). The γ-ray emission technique has been tested on the bound-state populations of ^{10}B and ^{7}Be fragments emitted from light compound nuclei, formed in low energy reactions. The extracted temperatures agree with the temperature of the compound nucleus(229, 230). Emission temperatures (2 - 3 MeV) of target-like fragments, produced in higher energy reactions, are also consistent with emission from a thermalized source(227).

Whenever the level separations are smaller than the emission temperatures, feeding from higher-lying particle-unbound states can alter the primary populations and substantially alter the deduced temperature. Since the γ-ray method is restricted to low-lying bound states, it is more sensitive to side-feeding, whereas high-lying, particle-unstable states of intermediate mass fragments should be less sensitive to side-feeding effects. Over a wide incident energy range, the temperature extracted from the relative population of states of light clusters emitted in the forward hemisphere is 3 - 5 MeV(210-212, 231), which is substantially lower than the effective temperature inferred from the slope of the particle kinetic energy spectra. Furthermore, the temperature extracted from the relative population of states is only weakly dependent on the incident beam energy (see Figure 21). Even at 200 MeV/u, which should be well in the fireball regime, emission temperatures of only 6 MeV are measured(228). Temperature mesurements(232) for the hot composite nuclei formed in central collisions of the $^{40}Ar + ^{27}Al$ reaction also saturate around 5 MeV in the bombarding energy range of 45 - 65 MeV/u (see Figure 22).

MULTIFRAGMENTATION AND LIGHT CHARGED PARTICLE MULTIPLICITY The multiplicity of light particles or, for that matter, the total charged particle multiplicity may serve as a coarse measure of the impact parameter as well as a measure of the excitation energy. A set of experiments performed at Michigan State University on reactions of 50 MeV/u ^{129}Xe + ^{27}Al, ^{51}V, ^{nat}Cu, ^{89}Y, and ^{197}Au was designed to measure the forward-going intermediate mass fragments(IMFs) with a Si detector array(233), and to measure the light charged particles plus the lighter IMFs emitted at larger angles with the Miniball array(234). In Figure 23, the IMF multiplicity distribution is plotted for various cuts in the total charged particle multiplicity for several different targets. The IMF multiplicity (N_{IMF}) increases with both increasing target mass and charged particle multiplicity N_c. For the ^{197}Au target, the largest charged-particle multiplicity gate (and thus the highest excitation energy) is associated with the most probable value of N_{IMF} of 6, and the distribution extends up to 14. It is interesting to note that N_{IMF} increases smoothly with N_c and is practically independent of the target (see Figure 24). This suggests that the source of the IMFs as well as of the light charged particles is the incomplete fusion product formed when the Xe projectile picks up various amounts of mass from <u>any</u> target. This mass, and not the target, determines the mass and excitation energy of the source.

The simultaneous availability of the light charged particle multiplicity N_{lcp} from the Miniball and the source velocity associated with the intermediate mass fragments makes it possibile to establish their mutual correlation and any association with the excitation energy of a hot intermediate source. In Figure 25 the excitation energy calculated from the source velocity is plotted versus the N_{lcp} for three targets. The observed strong correlation between the source velocity and the N_{lcp} lends credence to their use as empirical variables strongly related to the excitation energy.

SOURCE VELOCITY AND EXCITATION ENERGY As we have seen, the center-of-mass velocity of a given event has been used in many experiments as a measure of the inelasticity of

the event and thus of the excitation energy(107, 108, 198, 199). If the reaction is studied in the incomplete fusion regime, the dependence of the excitation energy upon source velocity is simple, and the correlation between these two variables is expected to be strong. While an absolute correlation between the true excitation energy and that calculated from the source velocity is not yet available (see however Figure 25), the distributions in center-of-mass velocities can be used to identify and characterize multifragmentation sources.

The same technique that was used to identify and characterize binary sources in incomplete fusion reactions can be applied to multifragment decay. The parallel source velocity V_s of the multi-fold events was determined by: $V_s = \Sigma_i m_i V_i / \Sigma_i m_i$ where m_i and V_i are respectively the mass and the velocity in the laboratory frame of the ith fragment, and the summation is performed over all the detected fragments. As an example, the normalized source velocity distributions obtained from the reaction of 40-MeV/u ^{139}La on four targets are presented in Figure 26 for different fragment multiplicities. The observed peaks broaden significantly as the mass of the target is increased. In the framework of the incomplete fusion model, the increased width can be explained by a broader range of impact parameters giving rise to a larger range of incomplete fusion products. Light particle evaporation also contributes to the broadening of the source velocity distribution. This last contribution has been estimated(107) with the statistical code GEMINI(197). For the ^{12}C target, the width can be explained almost entirely by light particle evaporation, whereas for the heavier targets, evaporation accounts only for, at most, a third to a half of the observed width. Therefore, for these heavy targets, the width of the source velocity distribution can effectively be associated with a range of incomplete fusion processes.

At each energy, for a given target, the requirement of a larger multiplicity of complex fragments selects out events with lower source velocities, which, in an incomplete fusion picture, correspond to higher excitation energies. Similar results have been reported for the 60-MeV/u ^{22}Ne + ^{197}Au(223), the 30-MeV/u ^{40}Ar + ^{197}Au(235), and the 30-MeV/u ^{32}S + ^{58}Ni reactions(236).

Excitation Functions Valuable information can be obtained from the "excitation functions" of *n*-fold events. For instance, different models predict a sudden rise in the multibody probability for an excitation energy between 3 and 5 MeV/u, as a signature for the onset of multifragmentation(49, 180)(see e.g. Figure 6). These excitation functions can be obtained at a given bombarding energy from the source velocity distributions, since, as discussed above, the widths of these distributions are effectively related to a continuous range of incomplete fusion processes, and thus of excitation energies.

For 35 - 55 MeV/u ^{139}La-induced reactions on several targets, the relative abundances of binary, ternary, quaternary, and quinary events were determined for different bins of the source velocity, and thus of the corresponding mass and excitation energy of the source. Figure 27 presents the "excitation functions" for the multifold events, obtained from the source velocity distributions at four bombarding energies. $P(n)$ represents the proportion of n-fold events with respect to the total number of coincidence events: $P(n) = N(n)/[N(2)+N(3)+N(4)+...]$, where $N(n)$ is the number of n-fold events. Rather than plotting these probabilities directly as a function of the source velocity, we have chosen to plot them versus the quantity:

$$Q = (E/A)_{beam} x (V_{source}/ V_{beam}) x (1-V_{source}/V_{beam}). \quad (52)$$

This removes the bombarding energy dependence. The quantity Q corresponds to the excitation energy per nucleon in a simple incomplete fusion model. Because such a model does not take into account pre-equilibrium particle emission processes, the quantity Q may be considered as an upper limit of the true excitation energy. The uncertainty in the horizontal scale connected to the emission of preequilibrium nucleons is around 30% for the systems considered in this study(115). Therefore the semi-quantitative analysis presented below should not be strongly affected by such pre-equilibrium emission processes.

The excitation functions presented in Figure 27 exhibit several remarkable features. The excitation energies obtained with this procedure are stunning, as they extend up to 8 MeV/u!

Thus, "nuclear systems" with excitation energies as large as their total binding energy may be produced. The probabilities for three-, four-, and five-fold events increase substantially as a function of the quantity Q. Such behavior suggests that there is indeed a strong connection between the source velocity and excitation energy, since the multifragment decay probability is expected to increase dramatically with excitation energy. The strong dependence of the branching ratios on the calculated excitation energy also confirms that the width of the velocity distribution is mostly due to the reaction dynamics, and is only partly due to evaporative broadening. If evaporation processes were the only source of broadening, these excitation functions should be flat. A similar increase in the multiplicity of intermediate mass fragments has been observed recently at 30 - 100 MeV/u (79, 170, 237) and also at much higher incident energy(98, 99, 238, 239), where the average multiplicity of complex fragments increases up to an estimated excitation energy of 8 MeV/u, and decreases for higher excitation energies.

The rate of multifold events increases smoothly with the quantity Q, up to approximately 6-8 MeV/u, without showing any discontinuity. The statistical multifragmentation calculations of Bondorf et al. (49) predict a sudden rise in the multibody probability at an excitation energy of about 3 MeV/u for a nucleus of mass 100. Gross et al.(180) predict a similar transition to nuclear cracking at about 5 MeV/u for the ^{131}Xe nucleus.

<u>Decoupling of the Entrance and Exit Channels</u> A most remarkable result is that, at any given bombarding energy, these excitation functions are almost identical for all targets. Even more extraordinary is that these excitation functions are almost independent of the bombarding energy. At a given bombarding energy, the similarity between the excitation functions for the different targets indicates that the sources produced in these reactions can be characterized mainly from the amount of mass picked up by the projectile from the target, and that the reactions depend relatively little on the actual nature of the target.

To summarize, it appears that, no matter what the bombarding energy, once the excitation energy (and thus the angular momentum) is determined from the source velocity, the resulting branching ratios for the various multifragment channels are fixed. This suggests that statistics may play an important role in multifragmentation.

These results have been confirmed for the reactions induced by 60 MeV/u ^{197}Au incident on a variety of targets (see Figure 28). Again the excitation functions appear to be remarkably independent from the target on which the ^{197}Au projectile impinges.

Statistical Multifragmentation? The next obvious question that we want to address is that: what is the multi-fragmentation mechanism of these sources? In particular, is this decay controlled by dynamics, or by statistics?

As discussed in the previous section, the branching ratios between binary, ternary, etc decays and their dependence upon excitation energy may contain valuable information regarding this aspect of the reaction mechanism. We have already commented on the statistical appearance of these excitation functions and now would like to show that it is possible to plot them in a way that may make their statistical nature more readily apparent(240).

Let us suppose that the hot nuclear system formed in the heavy ion reaction decays statistically, and that a barrier of some sort governs this decay. This is the case for binary decay, though, of course, it is not clear that a similar "barrier" exists for higher order decays(42, 43, 144-146). Alternatively, in the framework of the chemical equilibrium picture, one can consider the potential energy of each configuration as a barrier. It is conceivable that, in this picture, there might arise a hierarchy of "barriers" such that all the binary configurations would have barriers closer to each other than to those of the ternary configurations, and so on. Thus, let us assume that B_2, B_3, ... B_n are the average "barriers" associated with binary, ternary, and n-body decays. The decay probability for each channel $P_n(E)$ should be proportional to the level density of the

system $\rho(E)$ (dominated by the internal degrees of freedom) at an excitation energy equal to the available energy E minus the barrier: $P_n(E) \propto \rho(E - B_n)$. For a Fermi gas level density, we have

$$P_n(E) \propto \exp\left[2\sqrt{a(E - B_n}\right], \tag{53}$$

where a is the level density parameter. For $E >> B_n$ one obtains:

$$P_n(E) \propto e^{2\sqrt{aE}} e^{-B_n\sqrt{a/E}} \propto e^{-B_n/T}. \tag{54}$$

Thus, a plot of P_n versus $E^{-1/2}$ should give a straight line.

This simple theoretical prediction has been empirically tested(241) for the overall fission probabilities in the Pb region, and was used to prove that the rapid rise in fission cross section in electron-induced fission of similar nuclei is due to statistics. In Figure 29 the total fission probability is plotted vs $E^{-1/2}$ for three α-induced reactions in an energy regime where compound nucleus formation is well established. The expected linear dependence is observed, and the slopes correlate quantitatively with the known fission barriers.

To see whether a similar dependence exists in the multifragmentation branching ratios, researchers have determined the multifragment branching ratios as a function of the excitation energy of the decaying source for the 60-MeV/u ^{197}Au + ^{27}Al, ^{51}V, ^{nat}Cu and ^{197}Au reactions. The normalized probabilities $P_n/(P_2)$ plotted in this manner are shown in Figure 30a. This $E^{-1/2}$ plot, indeed generate straight lines. In Figure 30b, data from 55-MeV/u ^{139}La-induced reactions(108) are plotted in the same fashion, to illustrate the generality of these results.

We believe that the observed linear dependence for both the ^{197}Au- and ^{139}La-induced reactions strongly suggests that these probabilities are controlled by phase space. Unfortunately, it can be shown that this qualitative approach cannot distinguish between simultaneous and sequential multifragmentation(240).

Z_{BOUND}, PERCOLATION, AND THE ALADIN EXPERIMENT The quantity Z_{bound} is defined as the sum of the charges bound in fragments (with the exclusion of those bound in deuterons or tritons). There should exist a correlation of this variable with the excitation energy,

since large excitation energies would decrease Z_{bound} by light particle evaporation. Thus, Z_{bound} has been used as a running variable to test a variety of models.

Of particular interest in this regard is the work(99) by the ALADIN collaboration that has studied the reactions $^{197}Au + ^{12}C$, ^{27}Al, ^{nat}Cu and ^{208}Pb at 600 MeV/u. These reactions are substantially different from those considered so far, since they are, most likely, located in the fireball regime. Consequently, the ^{197}Au projectile is abraded by the target nucleus and should not be excited by nucleons picked up from the target. Its excitation energy arises from the energy associated with the extra surface plus the part of the energy dissipated by friction during abrasion, plus the energy received from the strong nucleonic irradiation from the fireball. Examples of the use of Z_{bound} as a running variable or as a gate are demonstrated in Figure 31 which shows the evolution of the shape of the mass distribution with Z_{bound}. Other examples are shown in Figures 32 and 33. The choice of observables plotted vs Z_{bound} was strongly influenced by the Campi application of percolation theories to finite systems like nuclei, although other theories have also been used in attempts to fit the data.

Figure 32 shows the dependence of $\langle Z_{max} \rangle$ upon Z_{bound}. Of course Z_{bound} is the upper limit for $\langle Z_{max} \rangle$, so it is the difference between Z_{bound} and $\langle Z_{max} \rangle$ that is interesting. Similarly, the average IMF multiplicity vs Z_{bound}, as shown in Figure 33, must go to zero at both extremes of the range and have at least one maximum in between. These two figures are important because both empirical dependences were fit to determine the parameters of a percolation model. Figures 34 -35 study the relative asymmetry for the two largest fragments and the combination of moments γ_2(see Equation 34). The analyses shown in these figures demonstrate that, once the percolation parameters are adjusted to fit the data in Figures 32 and 33, the percolation model fits the remaining dependences as well. The Copenhagen statistical model, as well as GEMINI were also tested by using the masses and excitation energies obtained from a BUU calculation. The angular momentum was set to zero, which is very unrealistic and biased against GEMINI. The

Copenhagen statistical model fares less well than the percolation model, and the low energy sequential decay code GEMINI fares worst.

However, a direct intervention by the authors of the multifragmentation models into the data analysis has changed the situation dramatically. The latest publications from both the Copenhagen and Berlin groups show fits that are as satisfactory as those obtained with the percolation model(113, 114, 118). This agreement has been achieved as follows: a BUU code was run at various impact parameters, and the main fragment was taken as the starting point for the statistical multifragmentation calculation. The excitation energy, however, was not taken from the BUU calculation, but instead was adjusted in order to reproduce the curves in Figures 32 and 33, just as for the percolation model. Unfortunately, the adjusted energies turned out to be as much as a factor of two smaller than the BUU predictions. On the bright side, the remaining dependences were fit as well as by the percolation model.

A recent clusterizing model(242), purposefully incorporating a minimum of physics (Fermi distribution, two-body interaction, nucleon-nucleon interactions with strengths chosen to reproduce the mean binding energy for nucleons), also fits the data astonishingly well when applied to the output of a BUU code, without adjusting the energy.

It is also interesting to note that, although percolation could reproduce the dependence of the IMFs on the light charged particle multiplicity for the 50-, 80-, and 110-MeV/u $^{36}Ar + ^{197}Au$ reactions, it failed to reproduce the larger numbers of IMFs from the 50 MeV/u $^{129}Xe + ^{197}Au$ system(243). The lessons to be learned from these tumultuous and unbridled attempts to fit the data are not too clear as yet. But, when the dust settles, the following may be a possible outcome.

1. The percolation model is the simplest model with the least amount of physics that can reproduce certain features that apparently depend only upon some very generic and general properties of the relevant Hamiltonians.
2. All the other models luckily seem to contain these very general properties, but because of the choice of the variable are <u>not</u> tested on their specific physics.

3. We should search out observables that are not predicted by the percolation model in order to test the nuclear physics contained in the competing models.

4.3 High Energy Proton- and ^{3,4}He-induced Reactions

Some of the scenarios proposed for multifragmentation induced in heavy-ion collisions involve either compression followed by expansion through the spinodal region, or the evolution of the shape of the system into a configuration like a disk, a donut, or a bubble, which would then proceed to decay into many fragments as a result of surface instabilities. The strong dependence of the average IMF multiplicity upon excitation energy shown by the excitation functions, not to mention the decoupling of entrance and exit channels shown in many reactions, speak instead for a process dominated by statistics, not by dynamics. This primacy of excitation energy in multifragmentation can be tested in reactions induced by a very light particle (e.g., p or ^{3,4}He).

In these reactions, it is very difficult to imagine either compression phenomena or exotic shapes that require a complex dynamical evolution (except donuts, perhaps). There is strong evidence for complex fragment emission in high energy p- or ^{3,4}He induced reactions(7, 8, 11, 36-39, 244, 245).

For the ^{3}He + ^{nat}Ag reaction, inclusive data exist from ~100 to 3,600 MeV(20, 38, 246). Over this bombarding energy range, the elemental cross sections for IMFs increase by approximately two orders of magnitude. Power law fits to the fragment charge distributions result in decreasing values of the exponent τ (see, for example, Equations 13 and 43) up to a bombarding energy of 1,800 MeV. For this energy and higher, a constant value of $\tau = 2.1$ is observed(38). More recently, multifragment events with multiplicity up to four have been observed with a large solid angle, low threshold detector array for the 900 and 1800 MeV bombarding energies(245). Plots of the invariant cross section for carbon fragments in velocity space ($V_{\parallel}$ - $V_{\perp}$) space indicate a slow moving source with a velocity of 0.4 - 0.8 cm/ns.

A very recent experiment has studied the ^{4}He + ^{197}Au reaction at 0.985 and 3.65 GeV/u with a rather complex detector system(247). It showed the presence of multifragmentation with a mean multiplicity of intermediate mass fragments, $M_{IMF} = 3.6 \pm 0.6$ and 5.3 ± 0.8, respectively, for events triggered on one complex fragment. The rapid rise of M_{IMF} with bombarding energy is very likely attributable to the increased energy deposition in the ^{197}Au target with increasing bombarding energy.

Reminiscent of a classic experiment performed in singles, interesting features like those described for heavy-ion induced reactions have been observed in p-induced reactions at very high bombarding energies. The knowledge of p-induced reactions was furthered by the work of Porile et al(37) who studied the production of complex fragments from Xe with protons of energy extending from 1 to 80 GeV. Excitation functions from this work are shown in Figure 36. The analysis of kinetic energy spectra associated with the fragments shows the presence of two components. The first component is identified by the authors as a binary compound-nucleus-like component, while the second, which predominates at high energy, is seen as arising from a process of multifragmentation. An intriguing aspect of the authors' analysis is the attempt to explain the observed mass (charge) distributions and their energy dependence in terms of the liquid-vapor equilibrium theory. As shown above, such a theory predicts a mass distribution of the form

$$P(A) = P_o A^{\tau} x^A y^{A^{\sigma}}. \tag{55}$$

One should recall that the critical point corresponds to $x = y = 1$. When $T < T_{cr}$, $x < 1$ and $y > 1$, the vapor is supersaturated. When the charge distributions are analyzed by assigning $\tau = 2.2$ and $\sigma = 0.6386$, which are empirical values for a liquid-vapor phase transition, one obtains the values of x and y shown in Figure 37. One notices a striking behavior in their energy dependence. At low bombarding energies we find $x < 1$ and $y > 1$, as in a supersaturated vapor. As the bombarding energy increases, x increases and y decreases until, at approximately 10 GeV,

they meet at value 1 where they then stabilize and remain even as the bombarding energy is increased further.

The authors see in this dependence the confirmation of the liquid-vapor equilibrium theory. What would be desirable to have, in addition, is a determination of the excitation energy deposited in the nucleus as a function of bombarding energy, and finally a broader range of masses over which to test the distribution given by Equation 55.

4.4 Mass (Charge) Distributions

POWER LAW Trautmann et al(40) studied the mass distributions of singles from a broad range of reactions looking for the power law dependence predicted by the liquid-vapor transition near the critical temperature. The observation of such a power law dependence with an exponent close to the expected value of 2.3 lent early credence to such a model. It was soon noticed that this dependence is rather generic and can easily arise in a variety of situations, having little to do with critical processes(21, 34, 35, 63). Nonetheless, the shape of the light wing of the mass distribution is indeed very close to a power law and, when the exponent τ is plotted vs E_{lab} for a great variety of target-projectile combinations (in ordinary direct kinematics), one obtains a curve that is rather independent of the target-projectile combination(40) (see Figure 38). With increasing bombarding energy, τ first decreases and then is constant for the higher energies. The significance of this is still uncertain.

When gates are set on quantities that are correlated with the excitation energy, like Z_{bound}, the mass distributions undergo an interesting evolution (see Figure 31). Figure 31 can be compared with Figure 2, in which the results from a comminution calculation (sequential statistical decay) are reported. The shapes and their evolution with excitation energy are quite similar.

On the other hand, the dependence of the parameter τ on Z_{bound} (Figure 39) is not reproduced quantitatively either by a sequential multifragmentation calculation with GEMINI or

by a prompt multifragmentation calculation with the Copenhagen model. The input parameters for the GEMINI and Copenhagen codes were obtained from a BUU calculation, with some additional restrictions in the other model parameters, like a total angular momentum I = 0ħ assigned to the decaying system in GEMINI, or by choosing the cracking distance in Copenhagen model to reproduce the experimental dependence of Z_{max} vs Z_{bound}. A percolation model calculation (solid curve) fits the data when its parameters are adjusted to reproduce $\langle M_{IMF} \rangle$ and $\langle Z_{max} \rangle$. The significance of this fit is also uncertain.

TERNARY EVENTS The availability of good statistics for ternary events makes it possible to study the mass/charge partition between fragments in some detail. The distribution can be represented by means of Dalitz plots., in which the probability of a given mass partition is graphed as a density plot in an equilateral triangle. Each point in the triangle corresponds to a partition given by the length of the three segments lowered perpendicularly to each of the three sides. Therefore, an event with three equally-sized fragments is represented as a point in the center of the triangle, while an event with one large fragment and two small ones is located in one of the corners.

In Figure 40 the experimental values of Z_1/Z_{total}, Z_2/Z_{total}, Z_3/Z_{total} are plotted in such a manner. For low excitation energies (e.g. obtained for the reaction 35-MeV/u ^{139}La + ^{27}Al), the three-body events concentrate on the vertices of the triangle, indicating two small and one large fragments. With increasing excitation energy first the ridges and then the center of the triangle fill in, evidence of an evolution to more equal sized events. A similar evolution from the vertices to the center is observed for the 600-MeV/u ^{197}Au reaction on various targets as a smaller Z_{bound} gates are applied(99). However, a recent study of a very similar system, 45 MeV/u ^{129}Xe + Cu indicates an enhancement for the production of three fragments of nearly the same mass(248).

Attempts to fit the distributions from the 55-MeV/u ^{139}La + ^{27}Al reaction have been made in terms of a hybrid model(115) involving a Landau-Vlasov dynamical stage followed by a

statistical decay described by GEMINI (see Figure 41). It should be stressed that at the end of the dynamical stage the Dalitz plot would be empty, because only an incomplete fusion residue or a target and projectile remnant would be produced. After the deexcitation stage, the simulated Dalitz plot is very similar to the data, with a predominance of events with one heavy and two light fragments (located in the corners of the triangle). The relative abundance of these events is considerably reduced after filtering through the detection efficiency because the heavy fragments are strongly forward peaked and very often do not pass through the filter. From these calculations for the $^{139}La + ^{27}Al$ reaction, it appears that the three-body events are mostly deep-inelastic-like events followed by the decay of the excited projectile remnant.

5. CONCLUSION

Despite the intense efforts on the experimental and theoretical fronts, multifragmentation remains a rather mystifying process. Experimentally, it is not yet clear whether the process of multifragmentation is homogeneous or heterogeneous. However, it is known that often not all the fragments originate from the same mechanism. Furthermore, in some reactions, the initial binary decays are attributable to deep inelastic scattering or to incomplete fusion, while other binary decays that follow sequentially may be statistical.

Some progress has been made in characterizing the sources of what appears to be genuine multifragmentation, although a precise assignment of excitation energies, angular momentum, etc. is still lacking. The aspect of sequentiality remains uncertain. There are some indications that sequential binary decays close enough in time to allow for interactions among fragments are often involved. Excitation functions suggest that binary, ternary, quaternary, ... decays somehow compete statistically, and that dynamics may be relegated to the initial stage of source formation (for example, incomplete fusion or fireball regimes).

The problem of the unavoidable multiplication of complex fragments arising from the statistical decay of an alleged primary multifragmentation process is as worrisome as it is untouched.

The theoretical landscape reflects the unsettled experimental picture. Statistical models, sequential or simultaneous, are either fraught with ad-hoc parameters, or are hard pressed to reproduce the experimental data. In any case, they need as input masses, excitation energies, etc. that they can not provide on their own.

Dynamical models, at the moment, are more interesting for their ambitious scope than for their predictive abilities. The combination of mean field and multibody interactions, together with their varying roles with bombarding energy, represents the real challenge in the field of heavy-ion reactions.

The presence of various kinds of instabilities suggests a richness that may conceivably be present in multifragmentation. These are, at the moment, only hopes that nature may dash with the looming stroke of statistical equilibration.

Percolation models can describe many features associated with multiplicities and mass fluctuations with perplexing accuracy, despite their dearth of nuclear physics content. It is not obvious that this signifies the formation of a nuclear fluid near criticality. Nevertheless, it may be a signature of universal features associated with a challenging process.

***Acknowledgments**

This work was supported by the Director, Office of Energy Research, Office of High Energy and Nuclear Physics, Nuclear Physics Division of the U S Department of Energy, under contract DE-AC03-76SF00098.

Figure Captions

Fig. 1 Schematic classification of heavy-ion reactions and complex fragment production theories. The upper portion depicts binary processes that contribute to complex fragment production at low energy. The lower portion shows different possible multifragmentation processes.

Fig. 2 A log-log plot of theoretical mass distributions from comminution calculations of the deexcitation of a mass 100 compound nucleus at several excitation energies. Notice the power law behavior at small masses(109).

Fig. 3 Exponent τ of a power law fit to the low mass region, plotted as a function of excitation energy of the compound nucleus. See Figure 2.

Fig. 4 An example of the production of a four-body event from the sequential decay of the compound nucleus ^{145}Eu (ℓ_{max} = 60$\hbar$, E* = 600 MeV), as calculated by the statistical model code GEMINI(143). Evaporated neutrons and light charged particles ($Z \leq 2$) are shown by the filled and open circles, respectively. Residual nuclei and complex fragments are labelled by their mass and charge numbers.

Fig. 5 Probability of producing exactly one, two, three, or four fragments (left) with A>4, or (right) with A>10 as a function of excitation energy for ^{145}Eu (ℓ_{max} = 60$\hbar$) as calculated with statistical model code GEMINI(143).

Fig. 6 Calculated yields for the evaporation (E), fission (F), and cracking (C) processes as a function of the excitation energy for ^{131}Xe. The effect of the Coulomb interaction can seen by comparing the curves with (E and F) to the ones without (E_{nc} and F_{nc}) the Coulomb interaction(51). See discussion in text.

Fig. 7 Calculated mass distribution P(a) assuming N = 200. The three curves(53) correspond to $\Delta S/S_0$ = 0; 0.2; and -0.2. See discussion in text.

Fig. 8 BNV calculations for a head-on collision (b = 0) of the 55-MeV/u ^{90}Mo + ^{90}Mo reaction(172) at time steps of (a) 20, (b) 60, (c) 120, and (d) 180 fm/c. The front and side-views of the colliding systems are given in columns 1 and 2, respectively for a value of the incompressibility constant, K = 200 MeV. Similar views are shown in columns 3 and 4 for K = 540 MeV.

Fig. 9 Same as for Figure 8 for the 75-MeV/u ^{90}Mo + ^{90}Mo reaction.

Fig. 10 Same as for Figure 8 for the 100-MeV/u ^{90}Mo + ^{90}Mo reaction.

Fig. 11 Schematic illustration of the perturbation of a thin sheet of liquid. See discussion in text.

Fig. 12 BNV calculation for the 60-MeV/u ^{112}Sn + ^{112}Sn reaction (b = 4, K = 200 MeV) at a time step of 180 fm/c.

Fig. 13 A schematic representation of the evolution of the heavy-ion reaction mechanism with bombarding energy E and impact parameter b. The solid curves represent the transitions between the different regimes: (a) complete fusion plus deep inelastic collisions (DIC), (b) incomplete fusion, and (c) the fireball regimes.

Fig. 14 Contours of the experimental cross section $\partial^2\sigma/\partial v_{\|}\partial v_{\perp}$ in the $v_{\|}$-$v_{\perp}$ plane for representative fragments Z = 6 - 40 detected in the reaction E/A = 18.0-MeV ^{139}La + ^{12}C. The beam direction is vertical towards the top of the figure. The dashed lines show the maximum and minimum angular thresholds and the low velocity threshold of the detectors. The magnitudes of the contour levels indicated are relative(105).

Fig. 15 Linear contour plots of the source velocity versus total detected charge for two-fold coincidence events, for six incident bombarding energies and four different entrance channel asymmetries(108). The beam energy and the target are indicated in the first row and column, respectively. The total available energy in the center-of-mass system is given in the lower right of each frame. The horizontal lines and the vertical arrows indicate the complete fusion velocity for each system and the projectile charge, respectively. The data

corresponding to ^{129}Xe beams(199) have been shifted by three Z units to make the comparison easier ($\Delta Z_{La\text{-}Xe} = 3$).

Fig. 16 Schematic representation of the effect of light charged-particle evaporation on the correlation between the source velocity V_s and total charge Z_{tot} in complex fragments. The thick solid curve represents the correlation for the primary fragments. Going from the right to the left the three dashed lines represent cases of low, moderate and high excitation energy E^*, respectively, which corresponds to increasing amounts of light charged-particle emission and decreasing amounts of charge bound in complex fragments.

Fig. 17 Linear contour plots of Z_1 versus Z_2 for two-fold coincidence events(108). On some of the plots a diagonal line indicates the charge of the projectile ($Z_p = 57$).

Fig. 18 Most probable fraction of neutrons emittedas a function of the total number of neutrons contained in three heavy systems, studied at E_{lab} close to 30 MeV/u(207).

Fig. 19 Systematics of Gaussian source radii extracted for a variety of reactions(216)

Fig. 20 The upper portion contains a comparison of inclusive C-C correlation functions (points) to three-body Coulomb trajectory calculations (curves)(222). The lower portion contains a comparison of correlations functions calculated using the techniques fo Gong et al (249) (curve) and using three-body trajectory methods (points).

Fig. 21 Emission temperatures as deduced from the ratio of population ratios in ^{5}Li(top) and ^{4}He(bottom) as function of incident energy for heavy-ion-induced reactions on ^{197}Au (228).

Fig. 22 Evolution of the measured temperatures and of the deduced initial values as a function of incident energy in central collisions between ^{40}Ar + ^{27}Al(232).

Fig. 23 Probability distributions of IMF multiplicity, $P(N_{IMF})$, measured for the 50-MeV/u ^{129}Xe + ^{197}Au, ^{89}Y, ^{nat}Cu, ^{51}V, ^{27}Al, and ^{12}C reactions for several gates on total charged particle multiplicity, N_c. The panels are labeled by target. The different symbols represent

the indicated multiplicity gates. The solid and dashed lines guide the eye through the data points(170).

Fig. 24 Average IMF multiplicity $<N_{IMF}>$ measured for a given total charged particle multiplicity N_c for the 50-MeV/u ^{129}Xe + ^{197}Au, ^{89}Y, ^{nat}Cu, ^{51}V, ^{27}Al, and ^{12}C reactions. The different symbols represent the indicated targets(170).

Fig. 25 The excitation energy E^* extracted from the experimental source velocity plotted against the light charged-particle multiplicity N_{lcp} for the 50-MeV/u ^{129}Xe + ^{197}Au, ^{nat}Cu, and ^{27}Al reactions(170).

Fig. 26 Source velocity distributions for the 40-MeV/u ^{139}La + ^{12}C, ^{27}Al, ^{51}V, and ^{nat}Cu reactions, and for different numbers of detected fragments. Only events with a total detected charge larger than 30 are represented. The source velocity has been normalized to the beam velocity(108).

Fig. 27 Proportion of 2-, 3-, 4-, and 5-fold events as a function of excitation energy per nucleon Q (see text) for the different targets (symbols, see inset) studied at E_{lab}=35 (upper left), 40 (lower left), 45 (upper right), and 55 MeV/u (lower right)(108).

Fig. 28 Same as Fig. 27 for the 60 MeV/u ^{197}Au + ^{12}C, ^{27}Al, ^{51}V, ^{nat} Cu and ^{197}Au reactions.

Fig. 29 The fission probability plotted as a function of $E^{-1/2}$ for the α-induced reactions $^{206}Pb(\alpha, f)$, $^{197}Au(\alpha, f)$, and $^{184}W(\alpha,f)$ The data are taken from (241).

Fig. 30 (*a*) The natural logarithm of the ratio of the probability of an *n*-fold event normalized to the binary events (symbols) as a function of $E^{-1/2}$ for the 60-MeV/A ^{197}Au + ^{27}Al, ^{51}V, ^{nat}Cu, and ^{197}Au reactions(240). The lines are the best fits to the data. (*b*) Same as in part a) of this figure for the 55 MeV/A ^{139}La + ^{27}Al, ^{51}V, and ^{nat}Cu reactions(108). See discussion in text.

Fig. 31 The measured charge distribution cross sections for 600-MeV/u ^{197}Au collisions on C, Al, Cu, and Pb targets(99). The data have been gated by the values of Z_{bound} that are listed on the right-hand side of the figure. For each target the data have been multiplied by the

following factors (in decreasing order of Z_{bound}: 10^4, 10^2, 1,10^{-1}, 10^{-2}, 10^{-3}, 10^{-4}, and 10^5 to separate the data sets. The error bars are in most cases smaller than the size of the symbols.

Fig. 32 The average Z_{max} as a function of Z_{bound} for Au 600-MeV/u collisions(99) on C(circles), Al(triangles), Cu(squares) and Pb(stars). The error bars are in most cases smaller than the size of the symbols. The lines are Copenhagen (dashed), GEMINI (dotted) and percolation (full) predictions.

Fig. 33 The average multiplicity of IMFs as a function of Z_{bound}. See Figure 32.

Fig. 34 The average value of the relative asymmetry between the largest and second largest charges in the event as a function of Z_{bound}. See Figure 32.

Fig. 35 The average value of γ_2 (see Equation 34) as a function of Z_{bound}. See Figure 32.

Fig. 36 Excitation functions for the reaction p + Xe producing complex fragments (F thru Si) at 48.5° (37).

Fig. 37 Values of the x and y parameters obtained from a fit to the data at 48.5° (37).

Fig. 38 Systematics of the τ parameter extracted from a power law fit to the mass (charge) distributions from a variety of reactions, as a function bombarding energy. The reactions and the references are indicated(40). See discussion in Section 4.4.

Fig. 39 The extracted τ parameters as a function of Z_{bound} for 600-MeV/u Au collisions on C(circles), Al(triangles), Cu(squares), and Pb(stars). The lines are Copenhagen (dashed), GEMINI (dotted) and percolation (full) predictions(99).

Fig. 40 Dalitz plots for three-body events from the 35-, 40- and 55-MeV/u ^{139}La + ^{27}Al, ^{51}V, ^{nat}Cu, and ^{139}La reactions(108). The detected fragments have been randomized so that there is no preferred ordering of Z_1, Z_2 and Z_3. See discussion in Section 4.4 on ternary events.

Fig. 41 Comparison of linear contour Dalitz plots for the data and the simulation before and after filtering through the detection efficiency, for the reaction $^{139}La + ^{27}Al$ at 55 MeV/u(115).

Literature Cited

1. Friedlander G, et al. *Phys. Rev* 94:727 (1954)

2. Caretto AA, Hudis J, Friedlander G. *Phys. Rev.* 110:1130 (1958)

3. Miller J, Hudis J. *Annu. Rev. Nucl. Sci.* 9:159 (1959) and references therein

4. Friedlander G. *Symp. Phys. & Chem. Fission, Salzburg, 1965,* pp. 265. Int'l Atomic Energy Agency

5. Poskanzer AM, Butler GW, Hyde EK. *Phys. Rev.* C3:882 (1971)

6. Hyde EK, Butler GW, Poskanzer AM. *Phys. Rev.* C4:1759 (1971)

7. Finn JE, et al. *Phys. Rev. Lett.* 49:1321 (1982)

8. Minich RW, et al. *Phys. Lett.* B118:458 (1982)

9. Chitwood CB, et al. *Phys. Lett.* B131:289-92 (1983)

10. Panagiotou AD, et al. *Phys. Rev. Lett.* 52:496-9 (1984)

11. Bujak A, et al. *Phys. Rev.* C32:620-22 (1985)

12. Poskanzer AM, et al. *Phys. Rev. Lett.* 35:1701 (1975)

13. Gosset J, et al. *Phys. Rev.* C16:629 (1977)

14. Meyer WG, et al. *Phys. Rev.* C22:179-91 (1980)

15. Warwick AI, et al. *Phys. Rev.* C27:1083-102 (1983)

16. Gutbrod HH, Poskanzer AM, Ritter HG. *Rep. Prog. Phys.* 52:1267-328 (1989) and references therein

17. Symons TJM, et al. *Phys. Rev. Lett.* 42:40 (1979)

18. Westfall GD, et al. *Phys. Rev. Lett.* 43:1859 (1979)

19. Sobotka LG, et al. *Phys. Rev. Lett.* 51:2187 (1983)

20. McMahan MA, et al. *Phys. Rev. Lett.* 54:1995 (1985)

21. Moretto LG, Wozniak GJ. *Prog. Part. & Nucl. Phys.* 21:401 (1988) and references therein

22. Delis DN, et al. *Nucl. Phys.* A534:403 (1991)

23. Rose HJ, Jones GA. *Nature* 307:245 (1984)

24. Hourani E, Hussonnois M, Poenaru DN. *Ann. Phys. (Paris)* 14:311 (1989) and references therein

25. Price PB. *Annu. Rev. Nucl. Part. Sci.* 39:19 (1989) and references therein

26. Zamyatnin SY, et al. *Fiz. Elem. Chastits At. Yadra* 21:537 (1990) and references therein

27. Fischer ME. *Physica* 3:255 (1967)

28. Fischer ME. *Rep. Prog. Phys.* 67:615 (1967)

29. Sauer G, Chandra H, Mosel U. *Nucl. Phys.* A264:221 (1976)

30. Bertsch G, Siemens PJ. *Phys. Lett.* B126:9 (1983)

31. Siemens PJ. *Nature* 305:410 (1983)

32. Schulz H, Voskresensky DN, Bondorf J. *Phys. Lett.* B133:141-5 (1983)

33. Goodman AL, Kapusta JI, Mekjian AZ. *Phys. Rev.* C30:851-65 (1984)

34. Hüfner J. *Phys. Rep.* 125:129 (1985) and references therein

35. Lynch WG. *Ann. Rev. Nucl. Part. Sci* 37:493 (1987) and references therein

36. Mahi M, et al. *Phys. Rev. Lett.* 60:1936-9 (1988)

37. Porile NT, et al. *Phys. Rev.* C39:1914-28 (1989)

38. Yennello SJ, et al. *Phys. Lett.* B246:26 (1990)

39. Yennello SJ, et al. *Phys. Rev.* C41:79-86 (1990)

40. Trautmann W, et al. *Z. Phys.* A344:447 (1993) and references therein

41. Randrup J, Koonin SE. *Nucl. Phys.* A356:223 (1981)

42. Lopez JA, Randrup J. *Nucl. Phys.* A503:183-222 (1989)

43. Lopez JA, Randrup J. *Nucl. Phys.* A512:345-64 (1990)

44. Medeiros EdL, Randrup J. *Phys. Rev.* C45:372-81 (1992)

45. Gross DHE. *Phys. Scr.* T5:213 (1983)

46. Friedman WA, Lynch WG. *Phys. Rev.* C28:16 (1983)

47. Friedman WA, Lynch WG. *Phys. Rev.* C28:950 (1983)

48. Bondorf JP, et al. *Nucl. Phys.* A443:321 (1985)

49. Bondorf JP, et al. *Nucl. Phys.* A444:460 (1985)

50. Friedman WA. *Phys. Rev. Lett.* 60:2125 (1988)

51. Gross DHE. *Rep. Prog. Phys.* 53:605 (1990) and references therein

52. Aichelin J, Hüfner J. *Phys. Lett.* B136:15 (1984)

53. Moretto LG, Bowman DR. *XXIV Inter. Winter Meeting of Nucl. Phys., Bormio, Italy, 1986,* pp. 126. Ricerca Scientifica ed Educazione Pemanente

54. Uehling EA, Uhlenbeck GE. *Phys. Rev.* 43:552 (1933)

55. Gregoire C, et al. *Nucl. Phys.* A465:317 (1987)

56. Nordheim LW. *Proc. Roy. Soc.* A119:689 (1928)

57. Aichelin J, Bertsch G. *Phys. Rev.* C31:1730 (1985)

58. Remaud B, et al. *Phys. Lett.* B180:198 (1986)

59. Rosenhauer A, et al. *J. Physique* 47 C4:395 (1986)

60. Gregoire C, et al. *Phys. Lett.* B186:14 (1987)

61. Bertsch GF, Gupta SD. *Phys. Rep.* 160:189 (1988) and references therein

62. Schuck P, et al. *Prog. Part. Nucl. Phys.* 22:181 (1989) and references therein

63. Aichelin J. *Phys. Rep.* 202:233-360 (1991) and references therein

64. Bonasera A, Gulminelli F. *Phys. Lett.* B259:399 (1991)

65. Bonasera A, Gulminelli F. *Phys. Lett.* B275:24 (1992)

66. Ayik S, Gregoire C. *Phys. Lett.* B212:269 (1988)

67. Ayik S, Gregoire C. *Nucl. Phys.* A513:187 (1990)

68. Randrup J, Remaud B. *Nucl. Phys.* A514:339 (1990)

69. Chomaz P, Burgio GF, Randrup J. *Phys. Lett.* B254:340 (1991)

70. Burgio GF, Chomaz P, Randrup J. *Nucl. Phys.* A529:157-89 (1991)

71. Burgio GF, Chomaz P, Randrup J. *Phys. Rev. Lett.* 69:885 (1992)

72. Suraud E, et al. *Nucl. Phys.* A542:141-58 (1992)

73. Aichelin J, Stöcker H. *Phys. Lett.* B176:14 (1986)

74. Aichelin J, et al. *Phys. Rev. Lett.* 58:1926 (1987)

75. Peilert G, et al. *Mod. Phys. Lett.* A3:459 (1988)

76. Peilert G, et al. *Phys. Rev.* C46:1457-73 (1992)

77. Sangster TC, et al. *Phys. Rev.* C46:1404-15 (1992)

78. Friedman WA. *Phys. Rev.* C42:667 (1990)

79. Bowman DR, et al. *Phys. Rev. Lett.* 67:1527 (1991)

80. Campi X, Desbois J. *XXIII Int'l Winter Meeting on Nuclear Physics, Bormio, Ital, 1985,* pp. 498-511. Ricerca Scientifica ed Educazione Permananente

81. Bauer W, et al. *Phys. Lett.* B150:53-6 (1985)

82. Bauer W, et al. *Nucl. Phys.* A452:699 (1986)

83. Biro TS, Knoll J, Richert J. *Nucl. Phys.* A459:692 (1986)

84. Campi X. *J. of Phys.* A19:L917 (1986)

85. Desbois J, et al. *Z. Phys.* A328:101 (1987)

86. Desbois J. *Nucl. Phys.* A466:724 (1987)

87. Campi X. *Phys. Lett.* B208:351 (1988)

88. Bauer W. *Phys. Rev.* C38:1297 (1988)

89. Jaqaman HR, Papp G, Gross DHE. *Nucl. Phys.* A514:327-38 (1990)

90. Ngo H, et al. *Z. Phys.* A337:81 (1990)

91. Kimura K, Tanaka Y. *J. Phys. G* 18:359-66 (1992)

92. Boisgard R, et al. *Inter. Conf. on High Energy Nucl. Phys., Balatonfüred, Hungary, 1987,* pp. 136-40.

93. Sneppen K, Vinet L. *Nucl. Phys.* A480:342 (1988)

94. Ngo C, et al. *Nucl. Phys.* A499:140-72 (1989)

95. Cugnon J, Volant C. *Z. Phys.* A334:435-42 (1989)

96. Leray S, et al. *Nucl. Phys.* A511:414 (1990)

97. Leray S, et al. *Nucl. Phys.* A531:177-91 (1991)

98. Hubele J, et al. *Phys. Rev.* C46:R1577-81 (1992)

99. Kreutz P, et al. *Nucl. Phys.* A(in press) (1993)

100. Moretto LG. *Phys. Lett.* B40:185 (1972)

101. Moretto LG. *Nucl. Phys.* A247:211 (1975)

102. Auger G, et al. *Z. Phys.* A321:243 (1985)

103. Charity RJ, et al. *Phys. Rev. Lett.* 56:1354 (1986)

104. Bowman DR, et al. *Phys. Lett.* B189:282 (1987)

105. Charity RJ, et al. *Nucl. Phys.* A511:59 (1990)

106. Bowman DR, et al. *Nucl. Phys.* A523:386 (1991)

107. Blumenfeld Y, et al. *Phys. Rev. Lett.* 66:576 (1991)

108. Roussel-Chomaz P, et al. *Nucl. Phys.* A551:508-40 (1993)

109. Moretto LG, Ashworth M, Wozniak GJ. *Proc. 8th High Energy Heavy Ion Study, Berkeley, CA, 1987,* pp. 273-87. Lawrence Berkeley Laboratory

110. Blann M, et al. *Phys. Rev.* C44:431-9 (1991)

111. Blann M, Mustafa MG. *Phys. Rev.* C44:R590-93 (1991)

112. Barz HW, et al. *Phys. Rev.* C46:R42-4 (1992)

113. Barz HW, et al. *NBI-92-88,* Neils Bohr Institute (1992)

114. Botvina AS, Mishustin IN. *Phys. Lett.* B294:23 (1992)

115. Colonna M, et al. *Phys. Lett.* B283:180 (1992)

116. Colonna M, et al. *Nucl. Phys.* A541:295 (1992)

117. Hagel K, et al. *Phys. Rev. Lett.* 68:2141-3 (1992)

118. Li B-A, DeAngelis AR, Gross DHE. *Phys. Lett.* B303:225-29 (1993)

119. Ploszajczak M, Tucholski A. *Phys. Rev. Lett.* 65:1539 (1990)

120. Ploszajczak M, Tucholski A. *Nucl. Phys.* 523:651 (1991)

121. Gross DHE, et al. *Phys. Rev. Lett.* 68:146-9 (1992)

122. DeAngelis AR, Gross DHE, Heck R. *Nucl. Phys.* A537:606-30 (1992)

123. Friedlander EM, Heckman HH. *Treatise on Heavy-Ion Science,* pp. 403. New York: Plenum Press (1985)

124. Csernai LP, Kapusta JI. *Phys. Rep.* 131:223 (1986) and references therein

125. Gregoire C, Tamain B. *Ann. Phys. Fr.* 11:323 (1986) and references therein

126. Boal DH. *Ann. Rev. Nucl. Part. Sci* 37:1 (1987) and references therein

127. Guerreau D. *Formation and Decay of Hot Nuclei: The Experimental Situation,* pp. 187-230. Plenum Publishing Corp. (1989)

128. Borderie B, Rivet MF, Tassan-Got L. *Ann. Phys. Fr.* 15:287-392 (1990) and references therein

129. Bauer W, Gelbke CK, Pratt S. *Annu. Rev. Nucl. Part. Sci.* 42:77-100 (1992) and references therein

130. Töke J, Schröder WU. *Annu. Rev. Nucl. Part. Sci* 42:401-46 (1992) and references therein

131. Glässel P, et al. *Z. Phys.* A310:189-216 (1983)

132. Moretto LG, Wozniak GJ. *Annu. Rev. Nucl. Part. Sci.* 34:189-245 (1984) and references therein

133. Morrissey DJ, et al. *Nucl. Phys.* A442:578-604 (1985)

134. Olmi A, et al. *Europhys. Lett.* 4:1121-26 (1987)

135. Charity RJ, et al. *Z. Phys.* A341:53-73 (1991)

136. Lopez JA, Randrup J. *Nucl. Phys.* A491:477 (1989)

137. Pouliot J, et al. *Phys. Lett.* B299:210 (1993)

138. Harmon BA, et al. *Phys. Lett.* B235:234 (1990)

139. Pouliot J, et al. *Phys. Rev.* C43:735-44 (1991)

140. Charity RJ, et al. *Phys. Rev.* C46:1951-67 (1992)

141. Hasse RW, Schuck P. *Phys. Lett.* B179:313 (1986)

142. Bortignon PF, Dasso CH. *Phys. Lett.* B189:381 (1987)

143. Charity RJ, et al. *Nucl. Phys.* A476:516 (1988)

144. Royer G, Mignen J. *J. Phys. G. Nucl. Part. Phys.* 18:1781-92 (1992)

145. Royer G, Haddad F, Mignen J. *J. Phys. G: Nucl. Part. Phys.* 18:2015-26 (1992)

146. Haddad F, Royer G. *J. Phys. G: Nuc. Part. Phys.* 18:L153-58 (1992)

147. Barranco M, Buchler JR. *Phys. Rev.* C22:1729 (1980)

148. Barranco M, Buchler JR. *Phys. Rev.* C24:1191 (1981)

149. Brack M. *Phys. Rev. Lett.* 53:119 (1984)

150. Lamb DQ, et al. *Nucl. Phys.* A360:459 (1981)

151. Band W. *J. Chem. Phys.* 7:324 (1939)

152. Frenkel J. *J. Chem. Phys.* 7:200 (1939)

153. Hill TL. *Statistical Mechanics,* pp. 149. McGraw Hill Inc (1956)

154. Bonche P, Levit S, Vautherin D. *Nucl. Phys.* A436:265 (1985)

155. Levit S, Bonche P. *Nucl. Phys.* A437:426 (1985)

156. Fai G, Randrup J. *Nucl. Phys.* A381:557 (1982)

157. Fai G, Randrup J. *Nucl. Phys.* A404:551 (1983)

158. Gross DHE, et al. *Z. Phys.* A309:41 (1982)

159. Jaqaman H, Mekjian AZ, Zamick L. *Phys. Rev.* C27:2782 (1983)

160. Barz WW, et al. *Nucl. Phys.* A448:753 (1986)

161. Morrissey DJ, Moretto LG. *Phys. Rev.* C23:1835 (1981)

162. Moretto LG. *Phys. Rev.* C29:843-6 (1984)

163. Bondorf JP, et al. *Nucl. Phys.* A444:460 (1986)

164. Barz HW, Bondorf JP, Schultz H. *Nucl. Phys.* A462:742 (1987)

165. Barz HW, et al. *Phys. Rev.* C39:1176-8 (1989)

166. Fong P. *Statistical Theory of Nuclear Fission,* pp. New York: Gordon & Breach (1969)

167. Sobotka LG, Moretto LG. *Phys. Rev.* C31:668 (1985)

168. Davies KTR, et al. *Phys. Rev. Lett.* 41:632 (1978)

169. Negele JW. *Rev. Mod. Phys.* 54:913 (1982) and references therein

170. Bowman DR, et al. *Phys. Rev.* C46:1834 (1992)

171. Rayleigh L. *Proc. London Math. Soc.* x:4-13 (1879)

172. Moretto LG, et al. *Phys. Rev. Lett.* 69:1884 (1992)

173. Blocki J, et al. *Ann. Phys.* 105:427 (1977)

174. Wong CY. *Phys. Rev. Lett.* 55:1973-5 (1985)

175. Bauer W, Bertsch GF, Schulz H. *Phys. Rev. Lett.* 69(13):1888-91 (1992)

176. Borderie B, et al. *Phys. Lett.* B302:15-17 (1992)

177. Gross DHE, Li B-A, DeAngelis AR. *Ann. Phys.* 1:467-72 (1992)

178. Xu XM, et al. *93-04,* Texas A&M University (1993)

179. Li B-A, Gross DHE. *Nucl. Phys.* A:in press (1993)

180. Gross DHE, Zheng Y, Massmann H. *Phys. Lett.* B200:397 (1988)

181. Nicholson WJ, Halpern I. *Phys. Rev.* 116:175 (1959)

182. Sikkeland T, Haines EL, Viola VE. *Phys. Rev.* 125:1350 (1962)

183. Viola VE, et al. *Phys. Rev.* C26:178 (1982)

184. Galin J, et al. *Phys. Rev. Lett.* 48:1787 (1982)

185. Conjeaud M, et al. *Phys. Lett.* B159:244 (1985)

186. Fatyga M, et al. *Phys. Rev. Lett.* 55:1376 (1985)

187. Bizard G, et al. *Nucl. Phys.* A456:173-85 (1986)

188. Viola VE. *Nucl. Phys.* A502:531c-50c (1989) and references therein

189. Begemann-Blaich M, et al. *Phys. Rev.* C45:677-88 (1992)

190. Knoche K, et al. Z. *Phys.* A342:319-27 (1992)

191. Leegte HKW, et al. *Phys. Rev.* C46:991-1007 (1992)

192. Jacquet D, et al. *Nucl. Phys.* A511:195-220 (1990)

193. Chbihi A, et al. *Phys. Rev.* C43:652-65 (1991)

194. Westfall GD, et al. *Phys. Rev. Lett.* 37:1202 (1976)

195. Charity RJ, et al. *Nucl. Phys.* A476:516 (1988)

196. Han HY, et al. *Nucl. Phys.* A492:138 (1989)

197. Charity RJ, et al. *Nucl. Phys.* A483:371 (1988)

198. Colonna N, et al. *Phys. Rev. Lett.* 62:1833 (1989)

199. Hanold K, et al. *LBL-32717,* Lawrence Berkeley Laboratory (1993)

200. Jahnke U, et al. in *Detectors in Heavy Ion Physics,* by Wv Oertzen. Vol. 178. ed. Berlin: Springer Verlag (1983)

201. Morjean M, et al. *Phys. Lett.* B203:215 (1988)

202. Galin J. *XXI Summer School on Nucl. Phys., Mikolajki, Poland, 1990,* pp.

203. Lott B, et al. *Phys. Rev. Lett.* 68:3141-4 (1992)

204. Galin J, et al. *Z. Phys.* A331:63 (1988)

205. Jiang DX, et al. *Nucl. Phys.* A503:560 (1989)

206. Crema E, et al. *Phys. Lett.* B258:266 (1991)

207. Piasecki E, et al. *Phys. Rev. Lett.* 66:1291-4 (1991)

208. Bresson S, et al. *Phys. Lett.* B294:33-39 (1992)

209. Brown RH, Twiss RQ. *Nature* 177:27 (1956)

210. Pochodzalla J, et al. *Phys. Rev. Lett.* 55:177-80 (1985)

211. Pochodzalla J, et al. *Phys. Rev.* C35:1695-719 (1987)

212. Nayak TK, et al. *Phys. Rev.* C45:132-61 (1992)

213. DeYoung PA, et al. *Phys. Rev.* C39:128-31 (1989)

214. Koonin SE, Bauer W, Schäfer A. *Phys. Rev. Lett.* 62:1247-50 (1989)

215. Goujdami D, et al. *Z. Phys.* A339:293-6 (1991)

216. Zhu F, et al. *Phys. Rev.* C44:R582-5 (1991)

217. Rebreyend D, et al. *Phys. Rev.* C46:2387-92 (1992)

218. Cebra DA, et al. *Phys. Lett.* B227:336-40 (1989)

219. Cebra DA, et al. *Phys. Rev. Lett.* 64:2246-9 (1990)

220. Hagel K, et al. *Phys. Lett.* B229:20-4 (1989)

221. Kim YD, et al. *Phys. Rev.* C45:387-95 (1992)

222. Kim YD, et al. *Phys. Rev. Lett.* 67:14-17 (1991)

223. Bougault R, et al. *Phys. Lett.* B232:291 (1989)

224. Stuttge L, et al. *Nucl. Phys.* A539:511-26 (1992)

225. Morrissey DJ, et al. *Phys. Lett.* B148:423-27 (1984)

226. Chen Z, et al. *Phys. Rev* C36:2297-308 (1987)

227. Dabrowski H, et al. *Phys. Lett.* B247:223 (1990)

228. Kunde GJ, et al. *Phys. Lett.* B272:202 (1991)

229. Morrissey DJ, et al. *Phys. Rev.* C34:761-3 (1986)

230. Lee JH, Benenson W, Morrissey DJ. *Phys. Rev.* C41:1562-75 (1990)

231. Chen Z, Gelbke CK. *Phys. Rev.* C38:2630-39 (1988)

232. Borderie B. *Ann. Phys. Fr.* 17:349 (1992)

233. Kehoe WL, et al. *Nucl. Instr. Meth. Phys. Res.* A311:258-72 (1992)

234. Souza RTd, et al. *Nucl. Instr. and Meth.* A295:109 (1990)

235. Bizard G, et al. *Phys. Lett.* B276:413-17 (1992)

236. Nebbia G, et al. *Phys. Rev.* C45:317-25 (1992)

237. Souza RTd, et al. *Phys. Lett.* B268:6 (1991)

238. Ogilvie CA, et al. *Phys. Rev. Lett* 67:1214 (1991)

239. Hubele J, et al. *Z. Phys.* A340:263 (1991)

240. Moretto LG, Delis DN, Wozniak GJ. *LBL-32948,* Lawrence Berkeley Laboratory (1992)

241. Moretto LG, et al. *Phys. Rev.* 179:1176 (1969)

242. Cerruti C, Garcia JB. *XXXI International Conference on Nuclear Physics, Bormio, Italy, 1993,* pp. in press. Nucl. Phys. A

243. Phair L, et al. *Phys. Lett.* B285:10-14 (1922)

244. Sangster TC, et al. *Phys. Lett.* B188:29-32 (1987)

245. Yennello SJ, et al. *Phys. Rev. Lett.* 67:671-674 (1991)

246. Kwiatkowski K, et al. *Phys. Lett.* B171:41 (1986)

247. Lips V, et al. *XXXI International Winter Meeting on Nuclear Physics, Bormio, Italy, 1993,* pp.

248. Bruno M, et al. *Phys. Lett.* B292:251-56 (1992)

249. Gong WG, et al. *Phys. Rev.* C43:781-800 (1991)

A Classification of IMF Production Theories

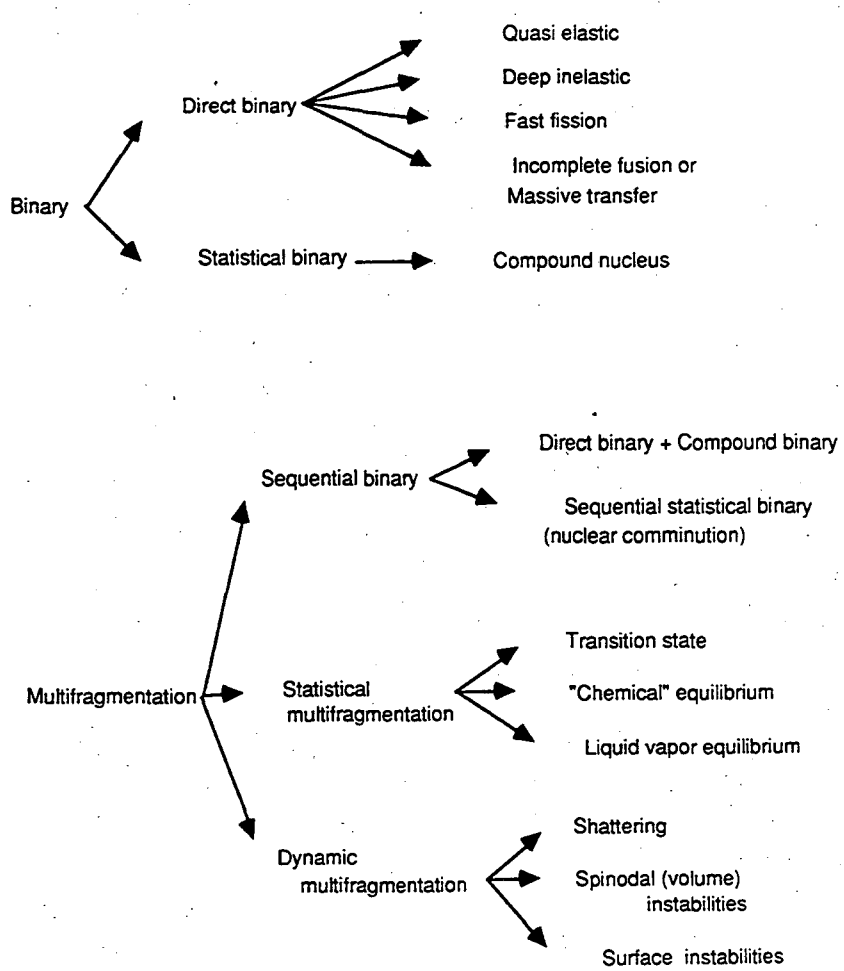

XBL 931-126

fig. 1

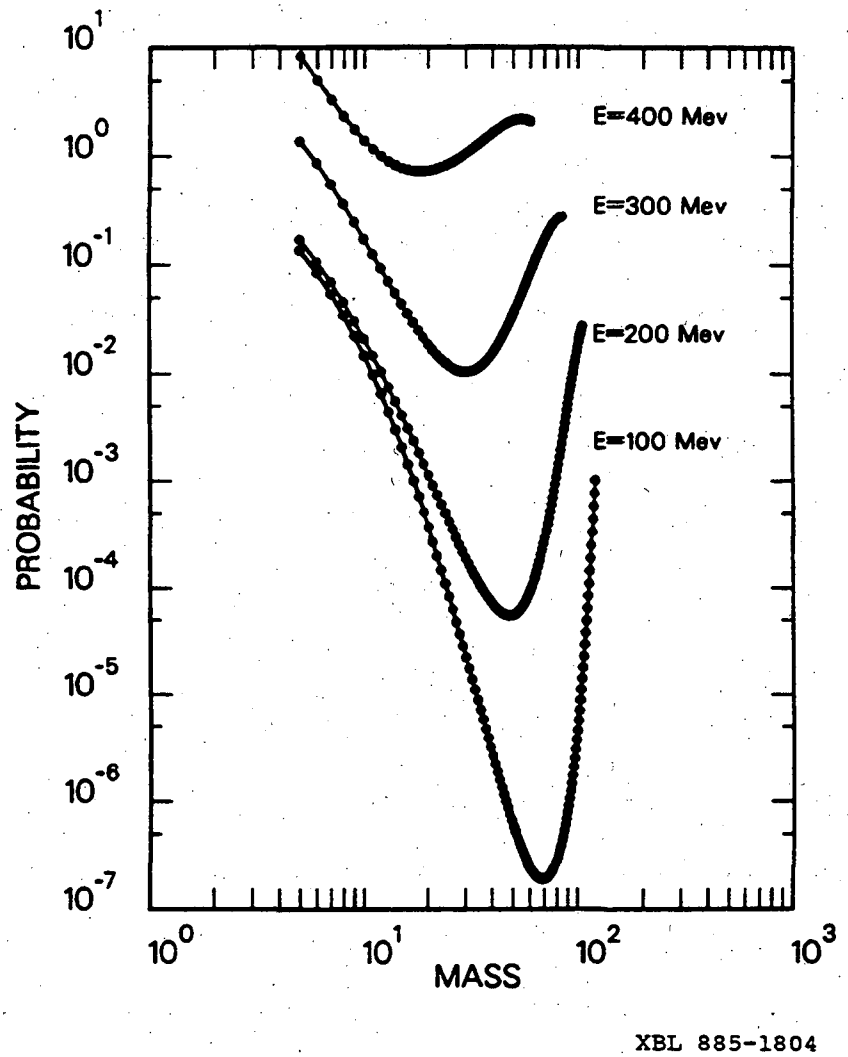
E=400 Mev
E=300 Mev
E=200 Mev
E=100 Mev
PROBABILITY
MASS
10^{1}
10^{0}
10^{-1}
10^{-2}
10^{-3}
10^{-4}
10^{-5}
10^{-6}
10^{-7}
10^{0}
10^{1}
10^{2}
10^{3}
XBL 885-1804

fig. 2

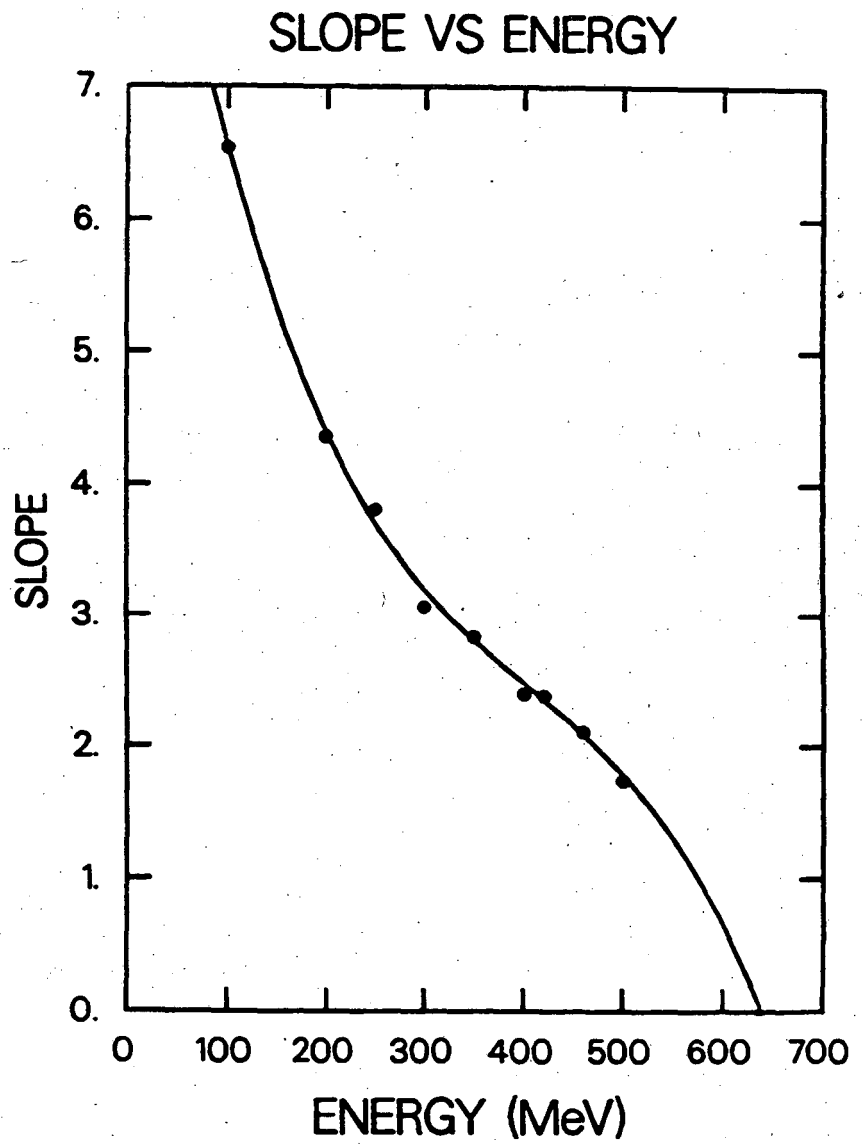

XBL 885-1805

fig. 3

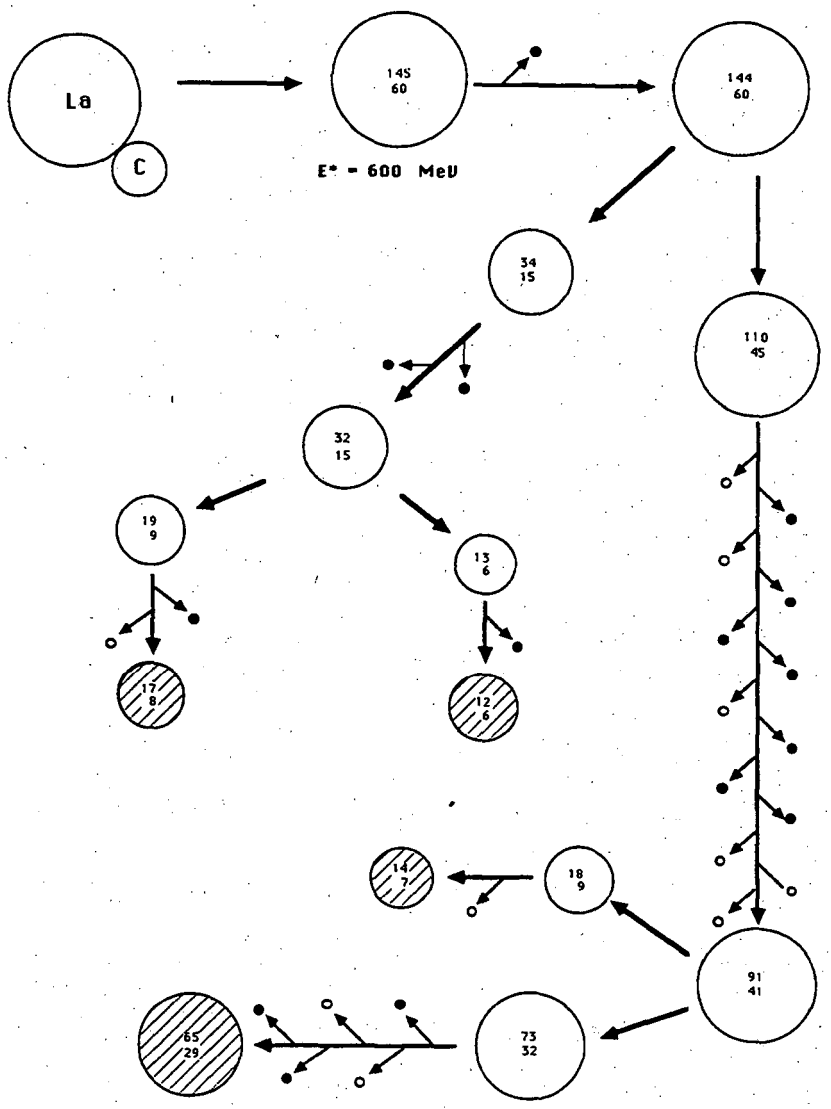

XBL 896-2407

fig. 4

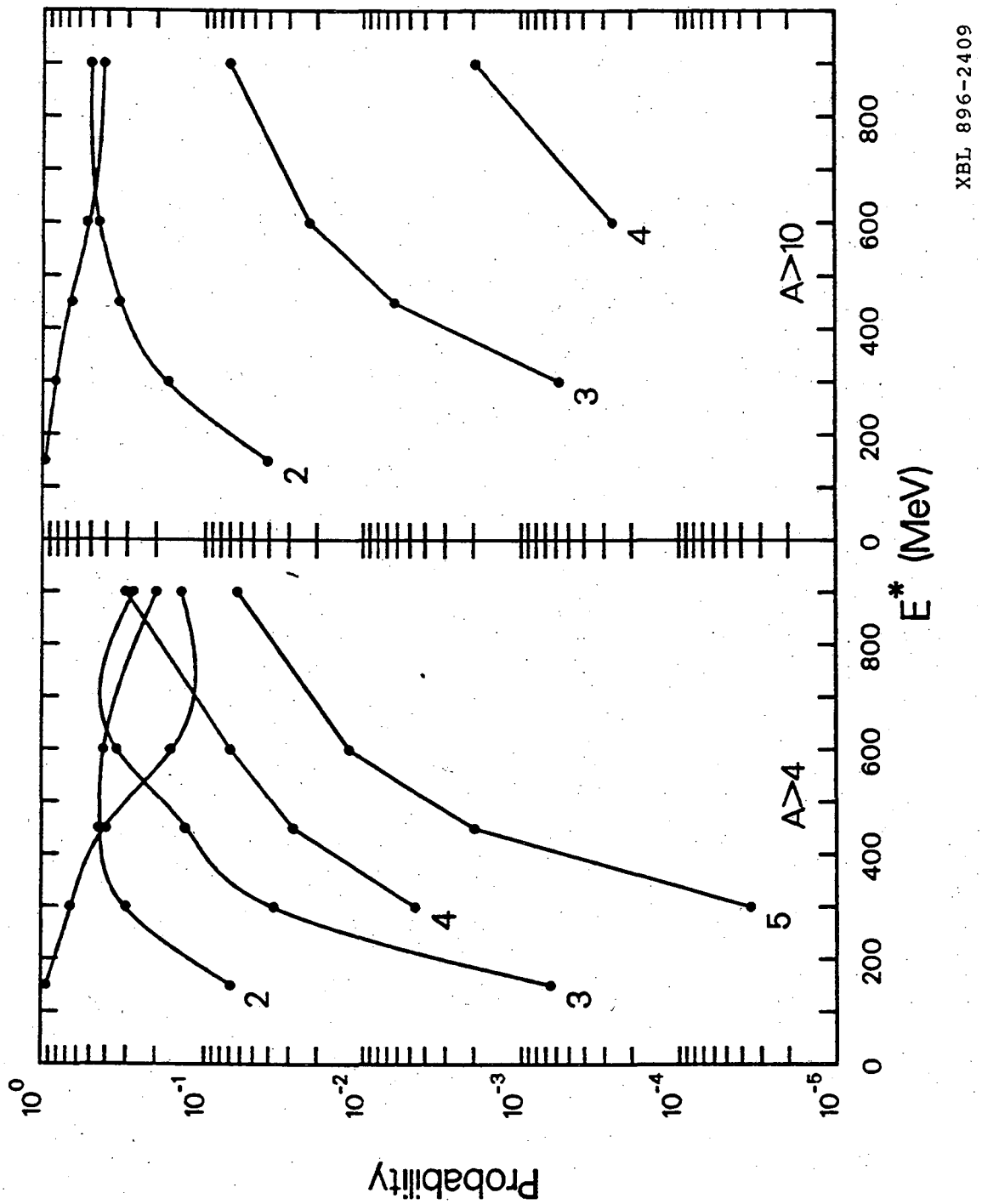
Probability
10^0
10^{-1}
10^{-2}
10^{-3}
10^{-4}
10^{-5}
A>4
A>10
2
3
4
5
0
200
400
600
800
E^* (MeV)
XBL 896-2409

fig. 5

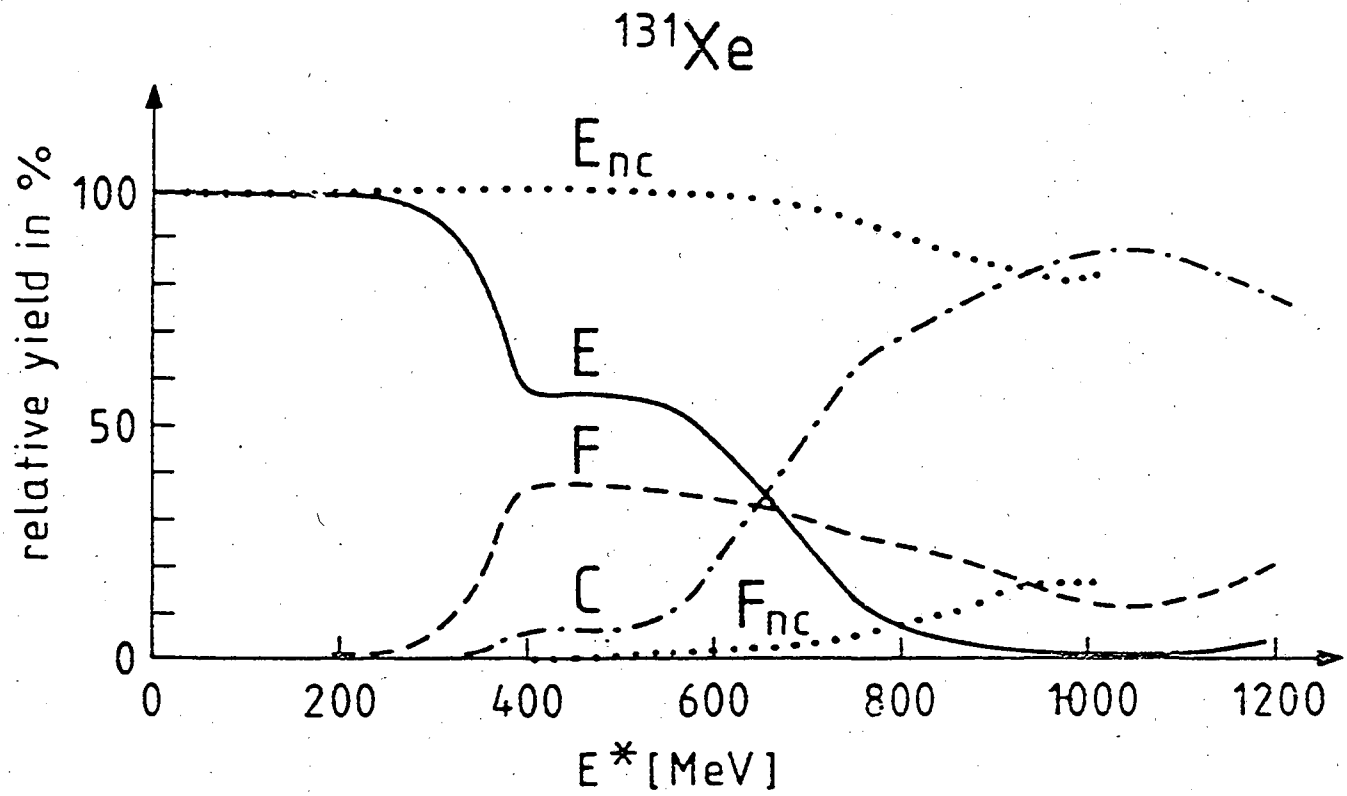

XBL 931-125

fig. 6

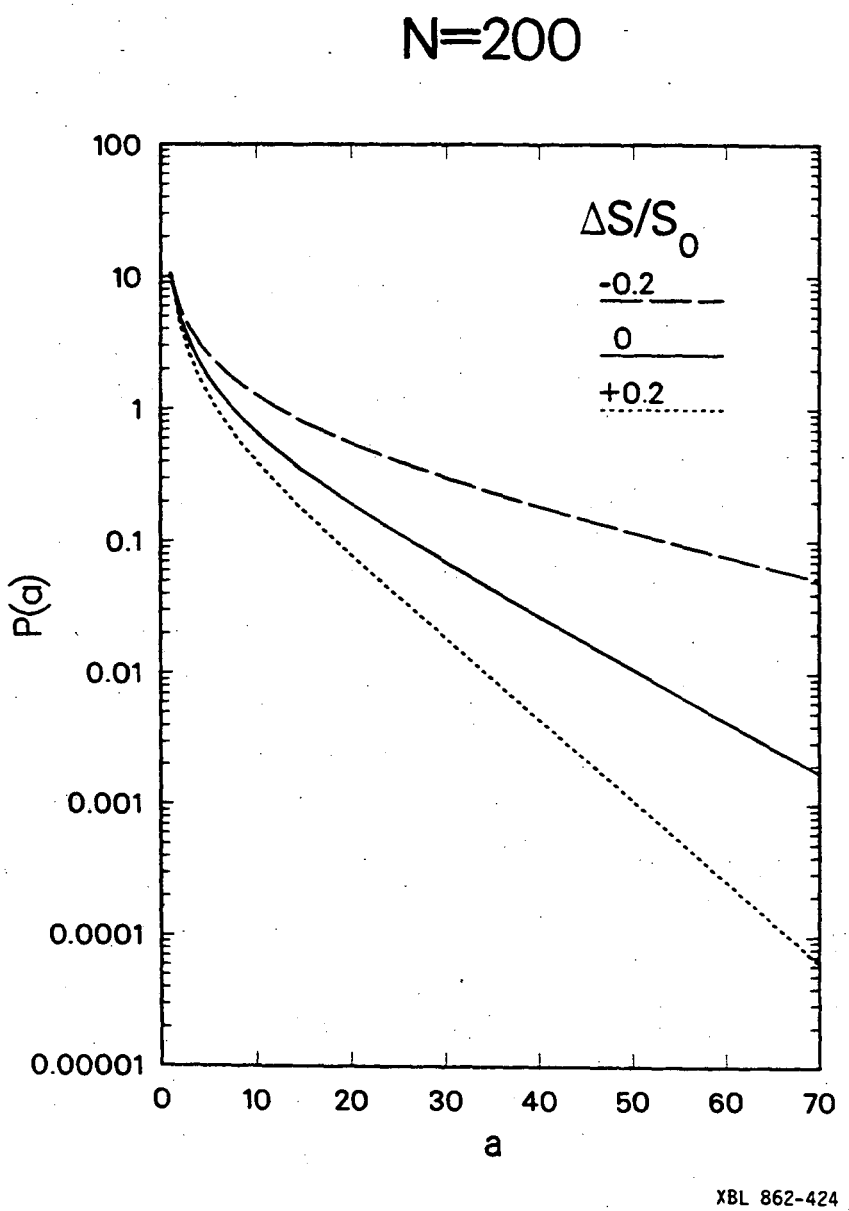
N=200
ΔS/S0
-0.2
0
+0.2
100
10
1
0.1
0.01
0.001
0.0001
0.00001
P(a)
0
10
20
30
40
50
60
70
a
XBL 862-424

fig. 7

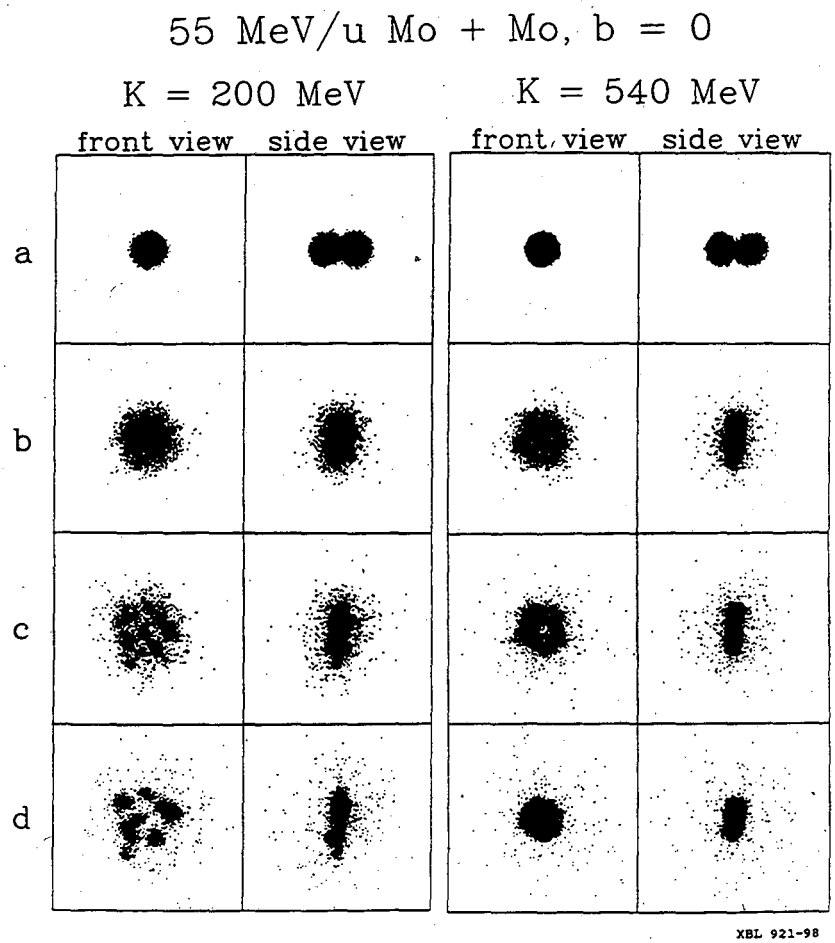
55 MeV/u Mo + Mo, b = 0
K = 200 MeV
K = 540 MeV
front view
side view
front view
side view
a
b
c
d
XBL 921-98

fig. 8

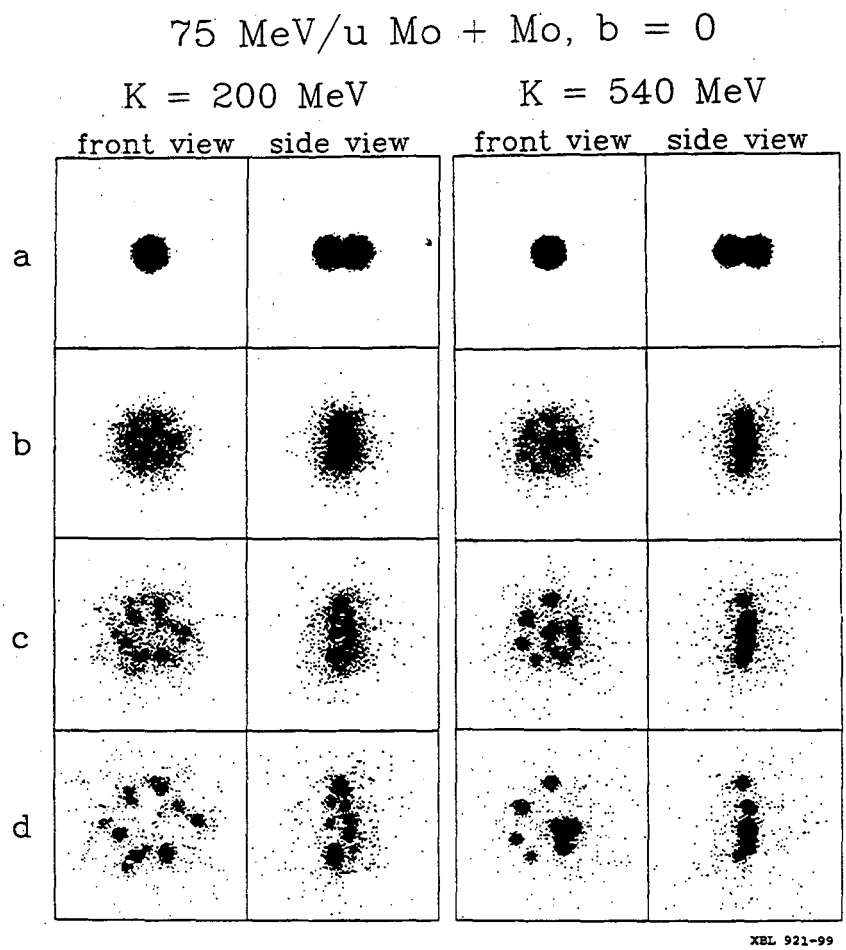
75 MeV/u Mo + Mo, b = 0
K = 200 MeV
K = 540 MeV
front view
side view
front view
side view
a
b
c
d
XBL 921-99

fig. 9

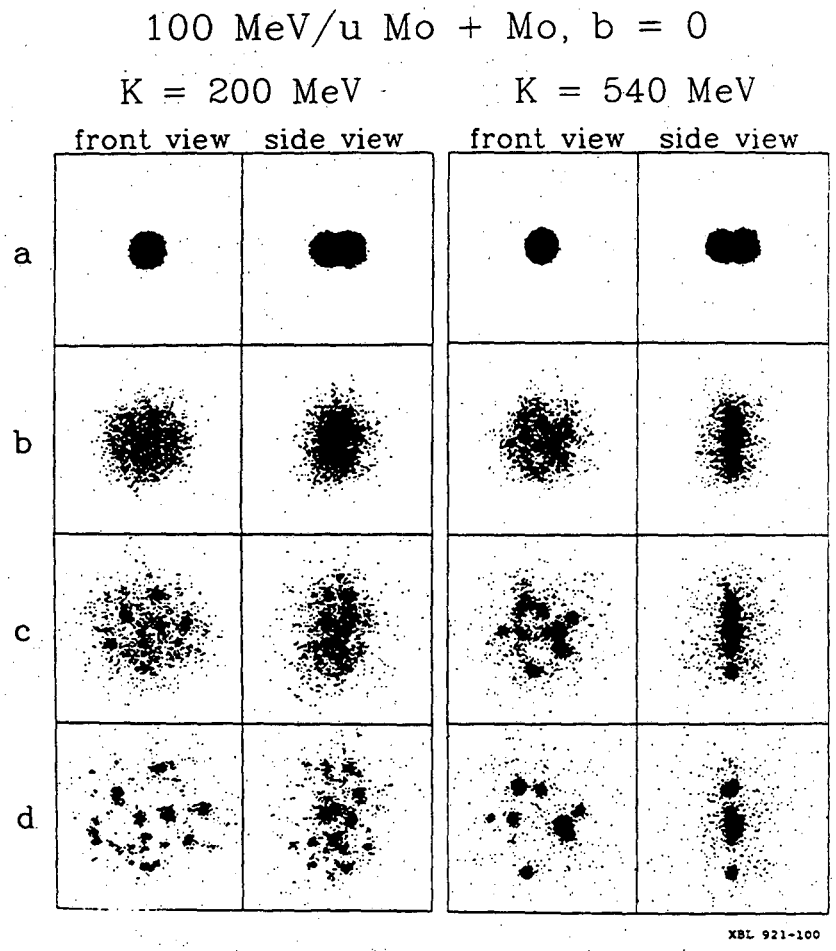
100 MeV/u Mo + Mo, b = 0
K = 200 MeV
K = 540 MeV
front view
side view
front view
side view
a
b
c
d
XBL 921-100

fig. 10

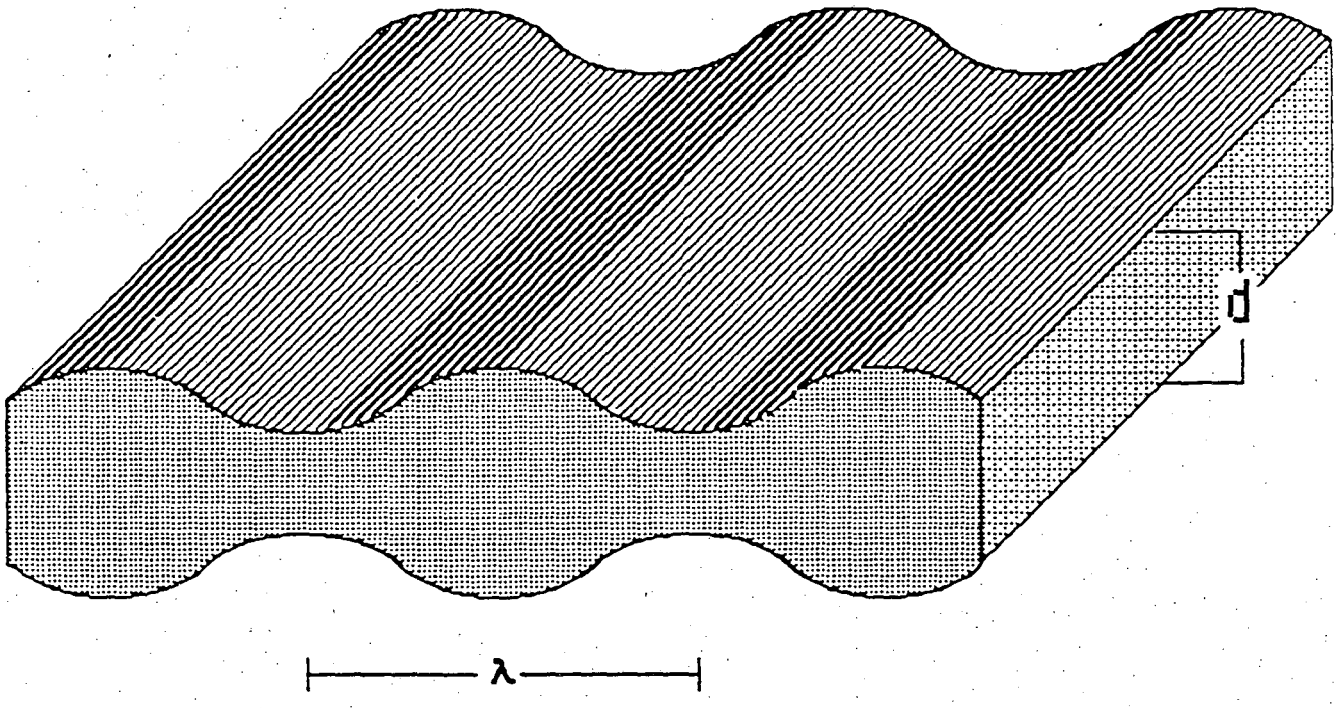

XBL 921-101

fig. 11

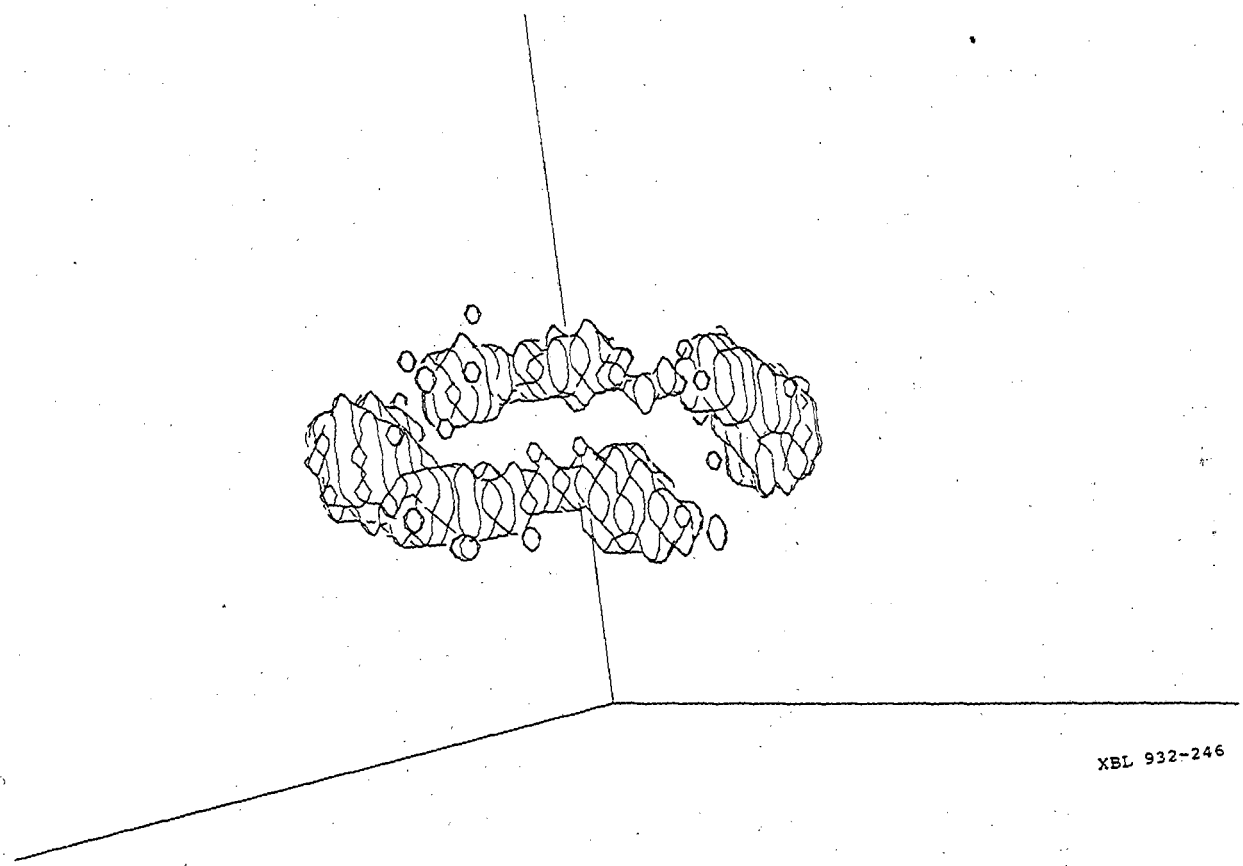

fig. 12

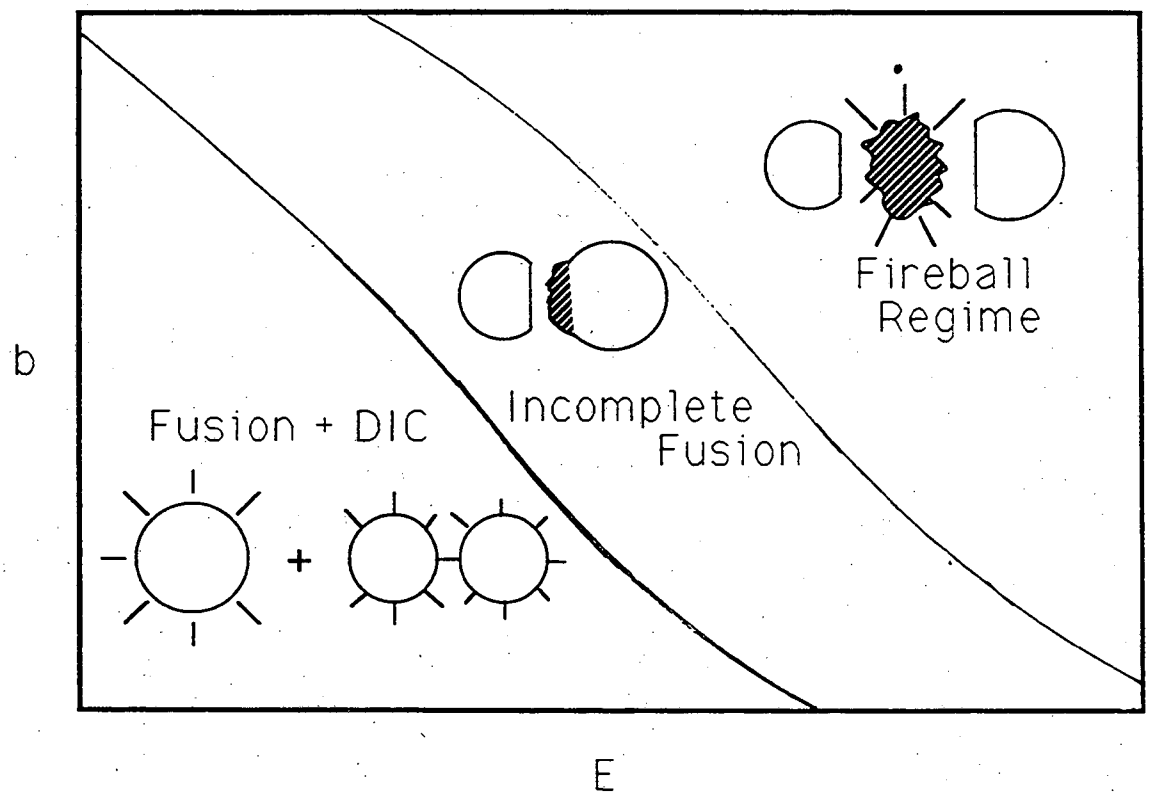

XBL 932-245

fig. 13

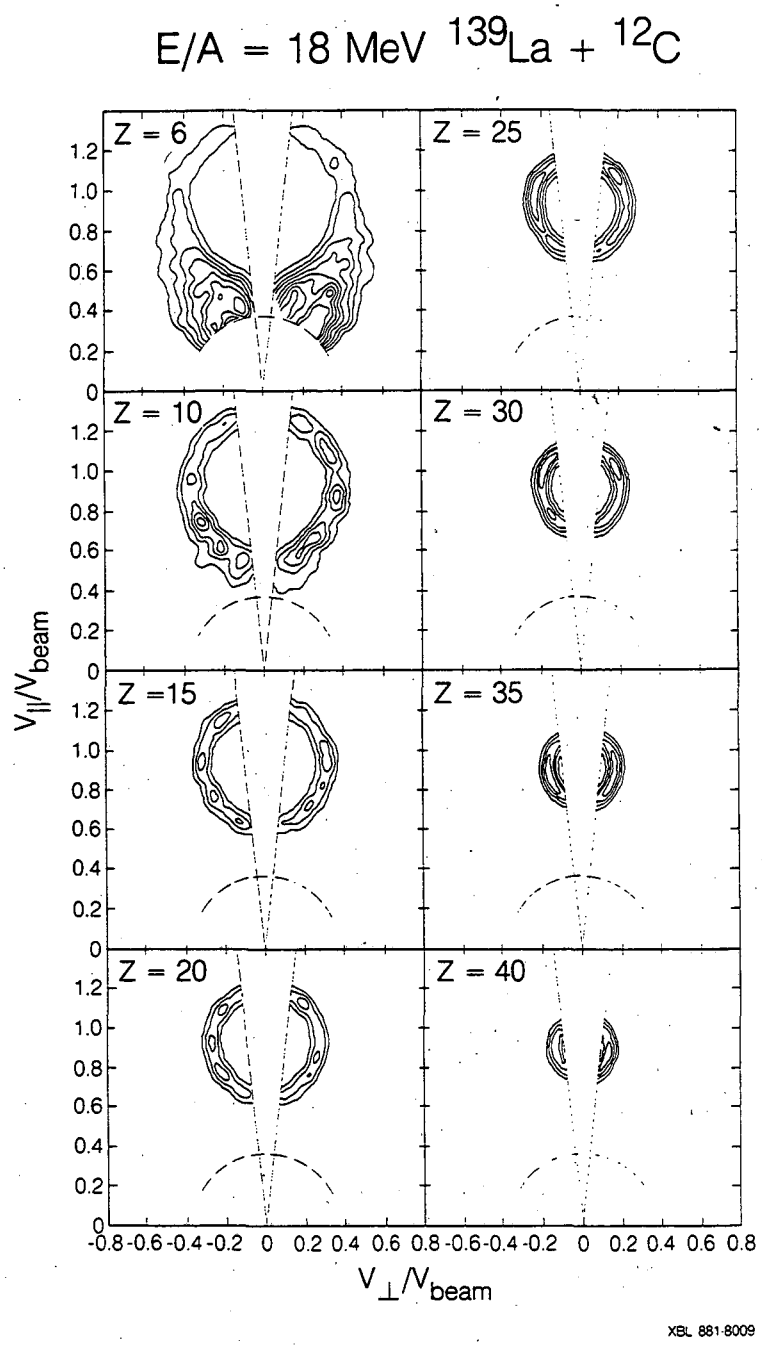
E/A = 18 MeV ^{139}La + ^{12}C
Z = 6
Z = 25
Z = 10
Z = 30
Z =15
Z = 35
Z = 20
Z = 40
$V_{\parallel}/V_{beam}$
$V_{\perp}/V_{beam}$
XBL 881-8009

fig. 14

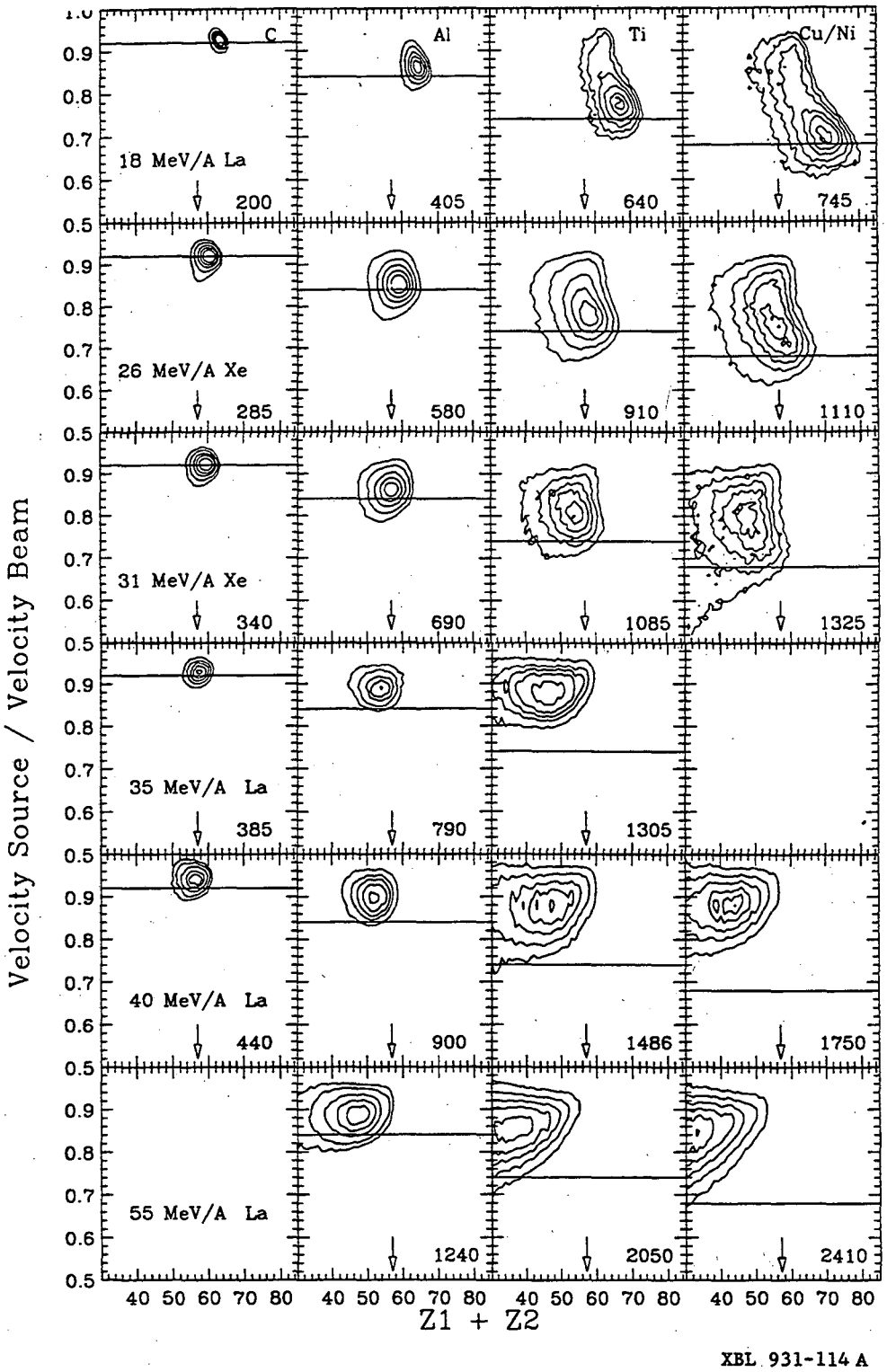
C
Al
Ti
Cu/Ni
18 MeV/A La
200
405
640
745
26 MeV/A Xe
285
580
910
1110
31 MeV/A Xe
340
690
1085
1325
35 MeV/A La
385
790
1305
40 MeV/A La
440
900
1486
1750
55 MeV/A La
1240
2050
2410
Velocity Source / Velocity Beam
Z1 + Z2
XBL 931-114 A

fig. 15

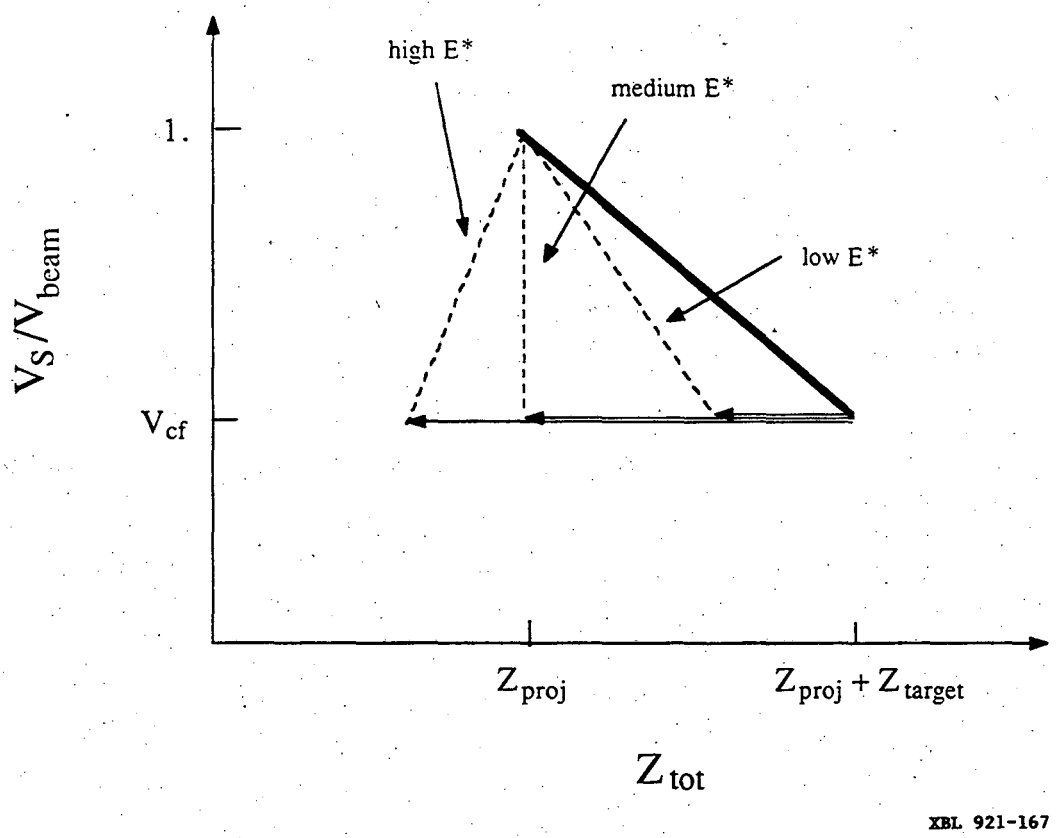
high E*
medium E*
low E*
1.
V_S/V_{beam}
V_{cf}
Z_{proj}
$Z_{proj} + Z_{target}$
Z_{tot}
XBL 921-167

fig. 16

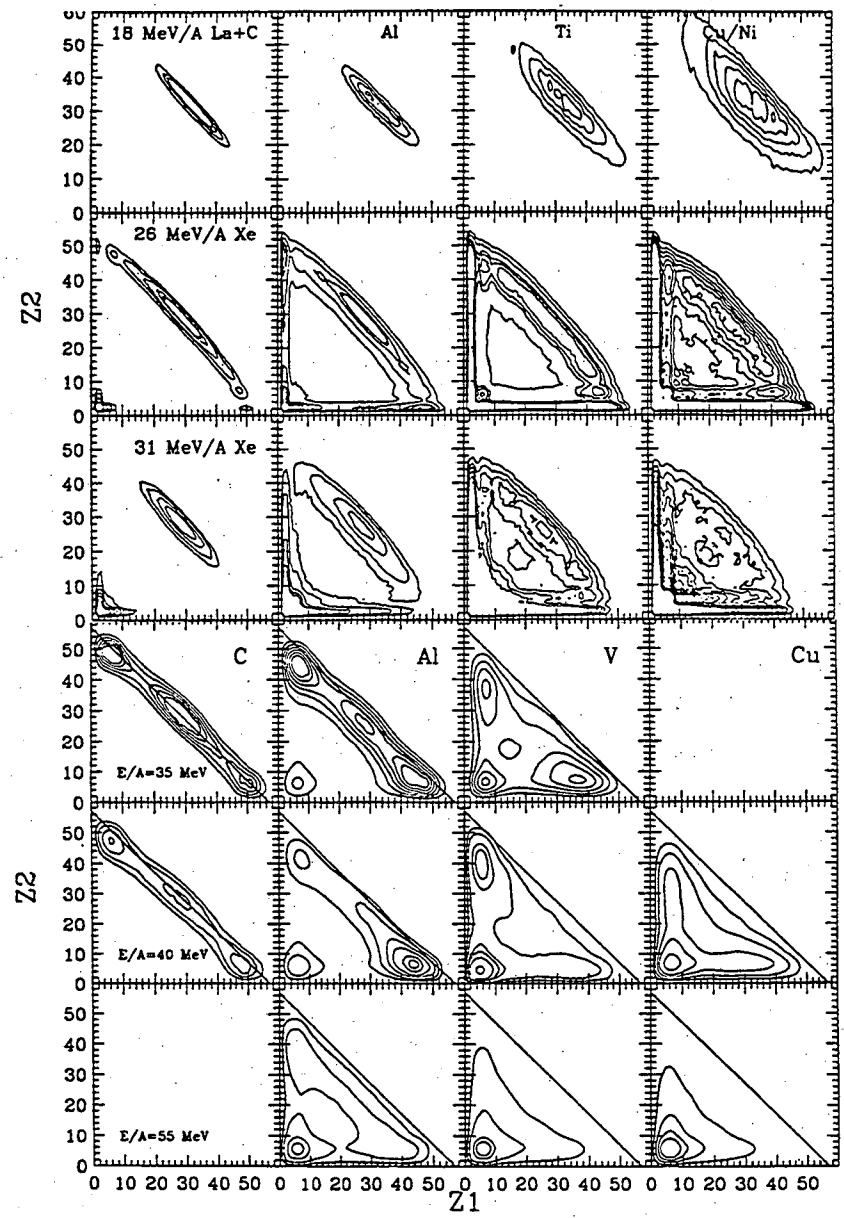
18 MeV/A La+C
Al
Ti
Cu/Ni
26 MeV/A Xe
31 MeV/A Xe
C
Al
V
Cu
E/A=35 MeV
E/A=40 MeV
E/A=55 MeV
Z2
Z1
0 10 20 30 40 50
XBL 931-113

fig. 17

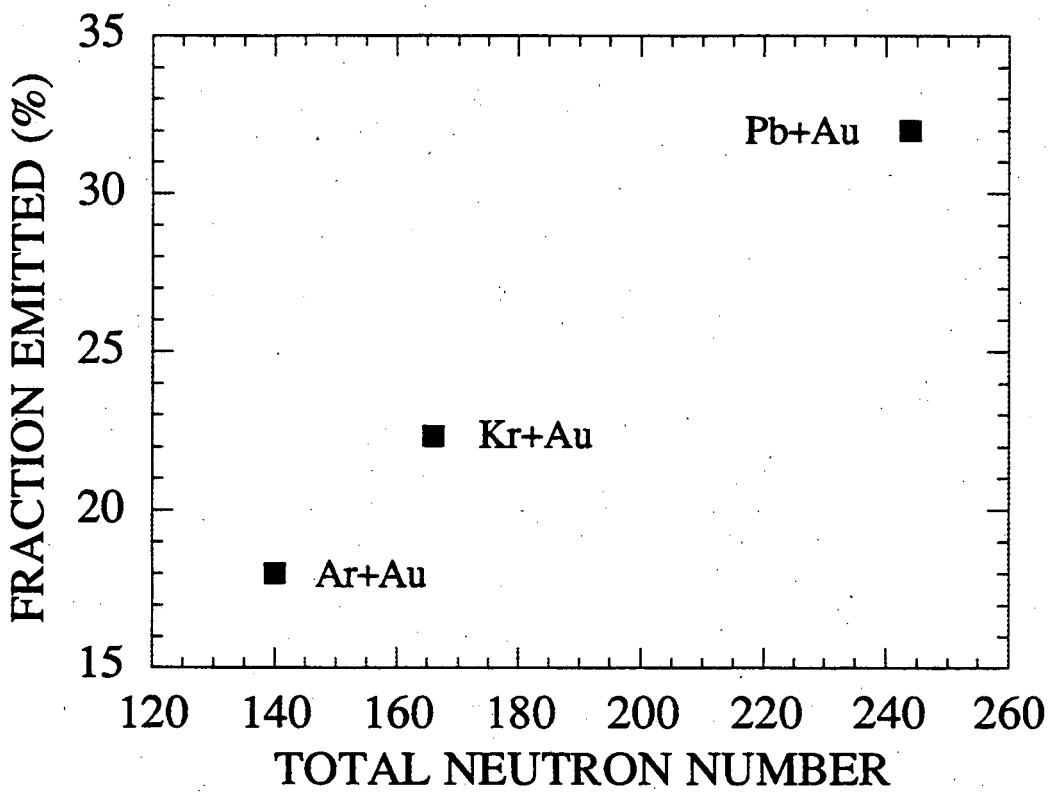

XBL 932-254

fig. 18

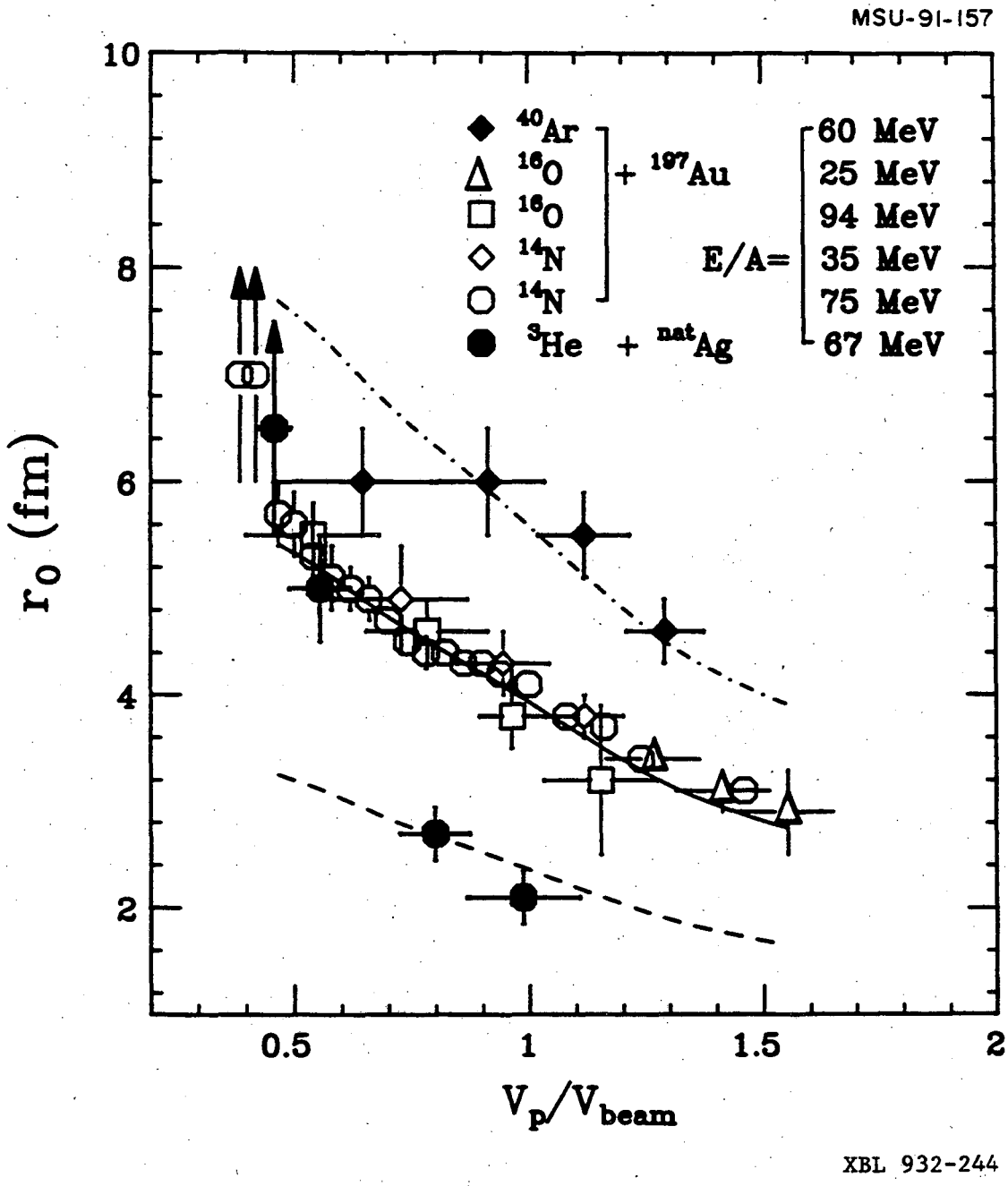
MSU-91-157
10
8
6
4
2
0.5
1
1.5
2
r_0 (fm)
V_p/V_{beam}
^{40}Ar
^{16}O
^{16}O
^{14}N
^{14}N
+ ^{197}Au
^{3}He + ^{nat}Ag
E/A=
60 MeV
25 MeV
94 MeV
35 MeV
75 MeV
67 MeV
XBL 932-244

fig. 19

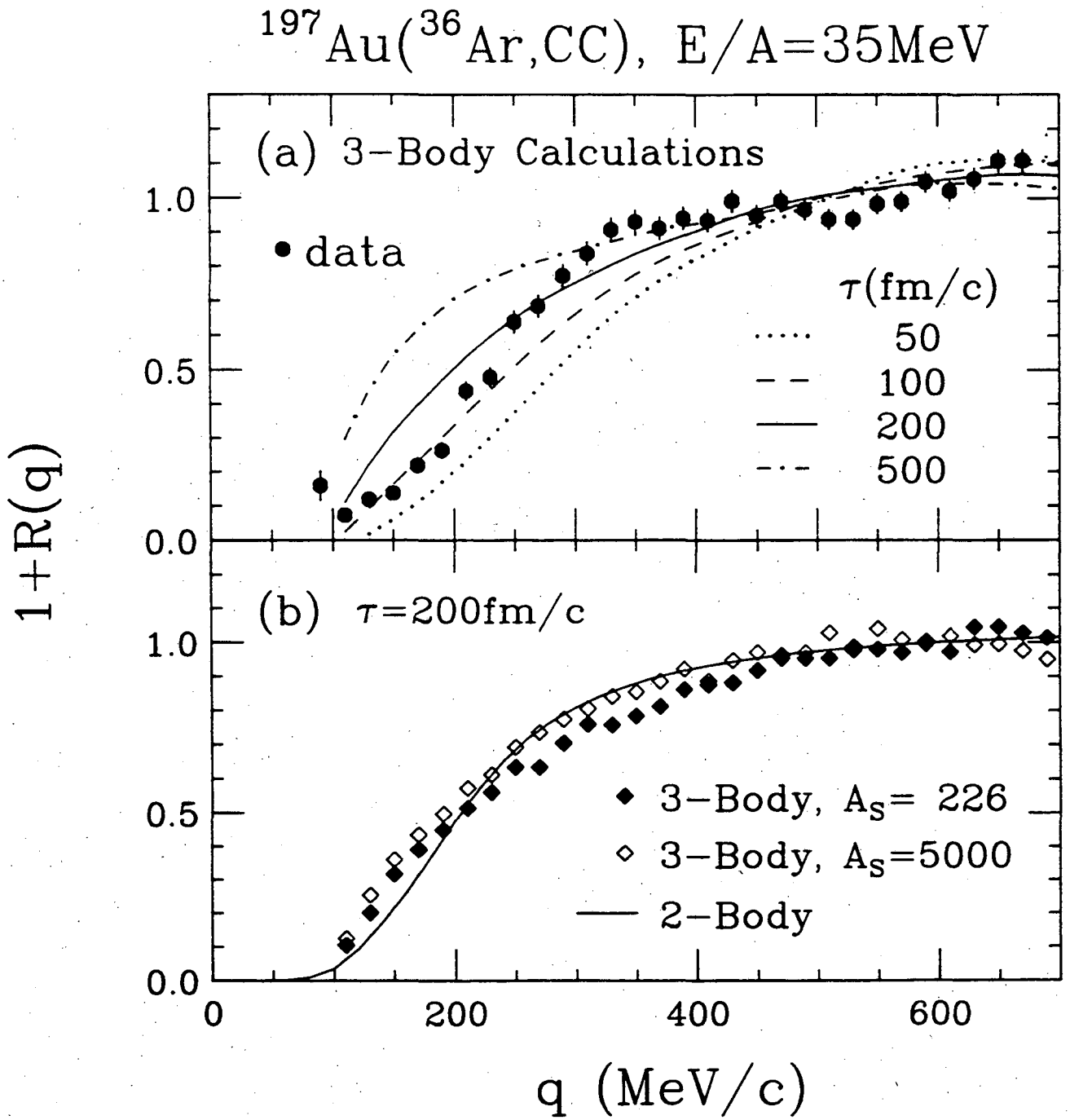
^{197}Au(^{36}Ar,CC), E/A=35MeV
(a) 3-Body Calculations
data
τ(fm/c)
50
100
200
500
(b) τ=200fm/c
3-Body, A_S= 226
3-Body, A_S=5000
2-Body
1+R(q)
q (MeV/c)
0.0
0.5
1.0
0
200
400
600

fig. 20

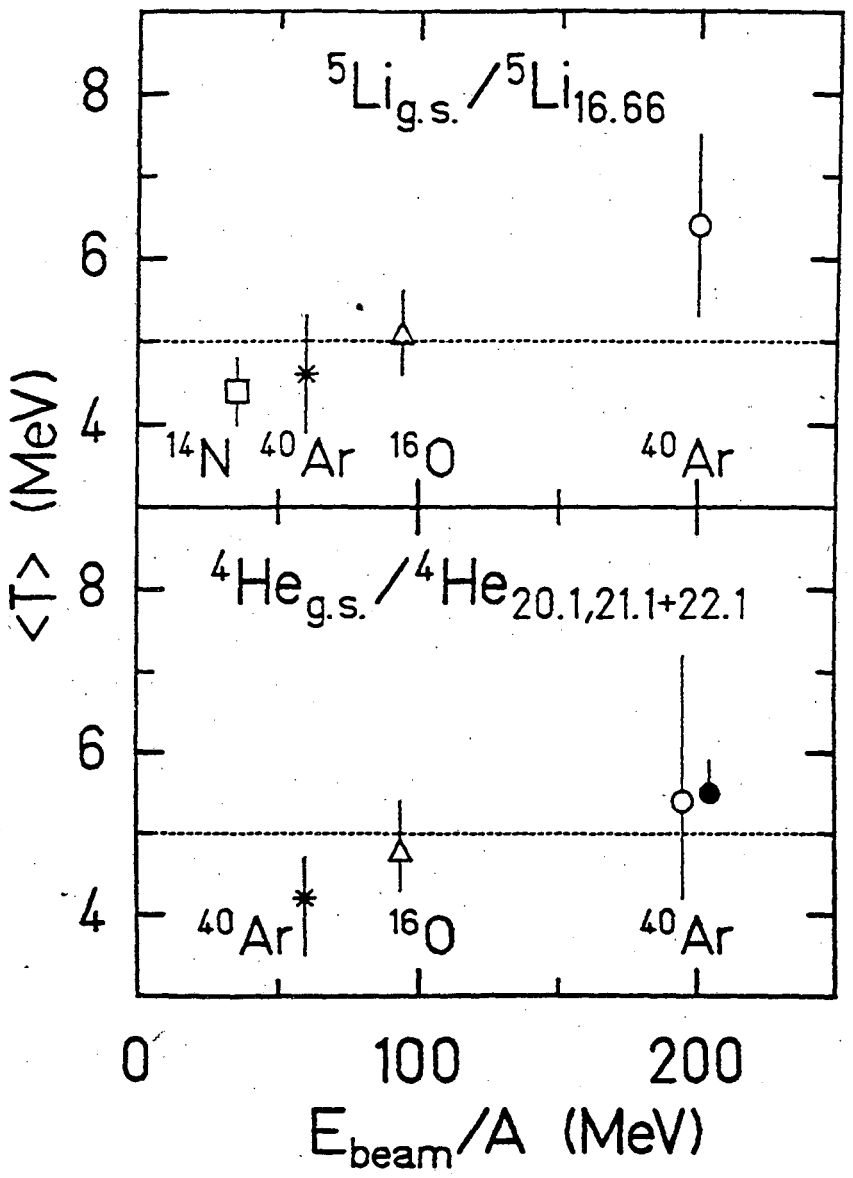

XBL 932-253

fig. 21

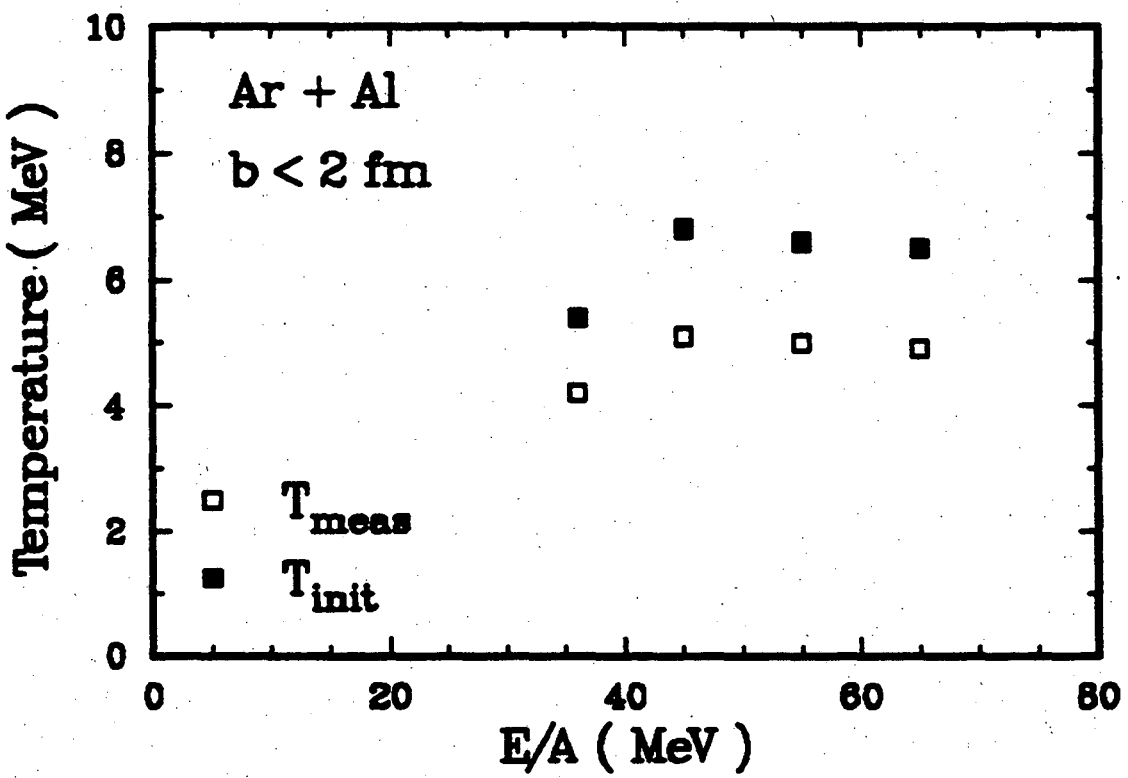

XBL 932-263

fig. 22

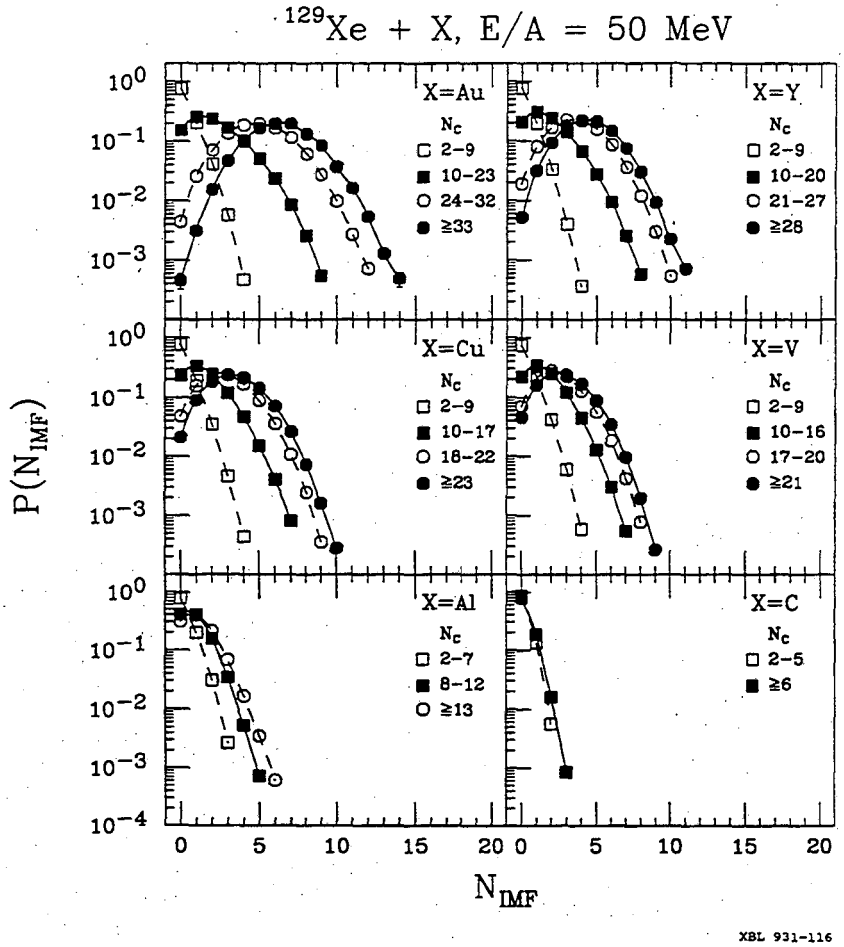
^{129}Xe + X, E/A = 50 MeV
X=Au
N_c
2-9
10-23
24-32
≥33
X=Y
N_c
2-9
10-20
21-27
≥28
X=Cu
N_c
2-9
10-17
18-22
≥23
X=V
N_c
2-9
10-16
17-20
≥21
X=Al
N_c
2-7
8-12
≥13
X=C
N_c
2-5
≥6
$P(N_{IMF})$
N_{IMF}
XBL 931-116

fig. 23

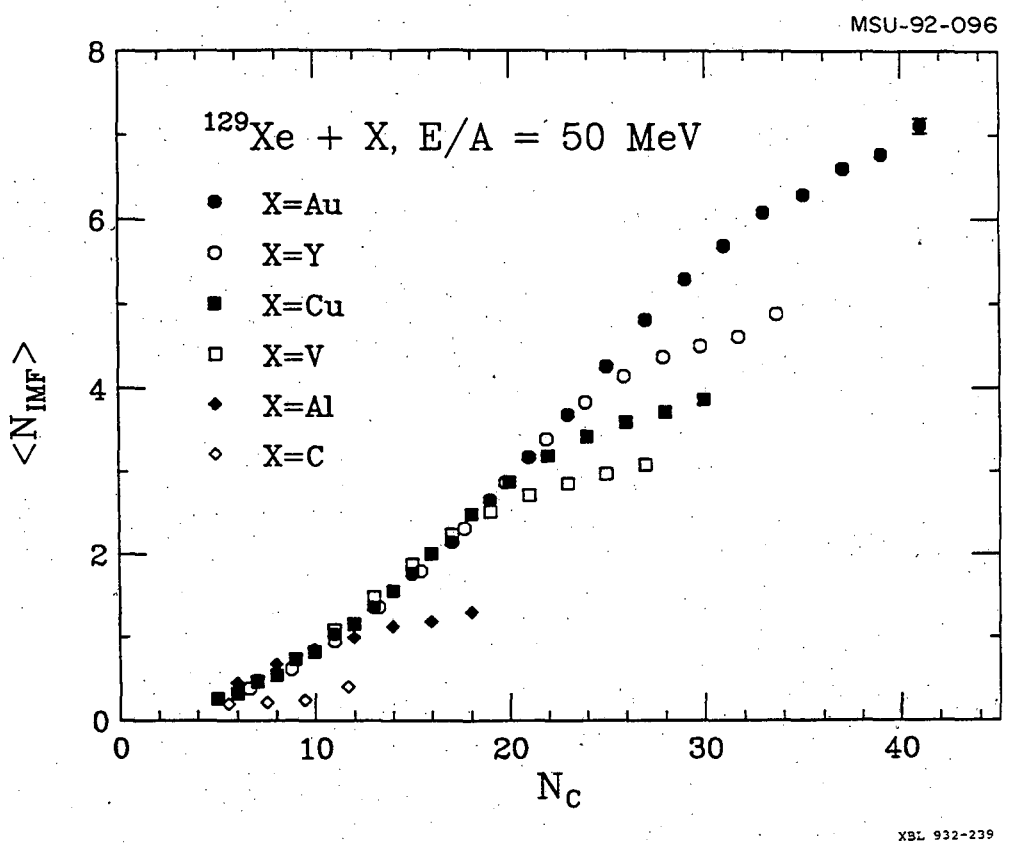
MSU-92-096
^{129}Xe + X, E/A = 50 MeV
X=Au
X=Y
X=Cu
X=V
X=Al
X=C
$\langle N_{IMF} \rangle$
N_c
0
2
4
6
8
0
10
20
30
40
XBL 932-239

fig. 24

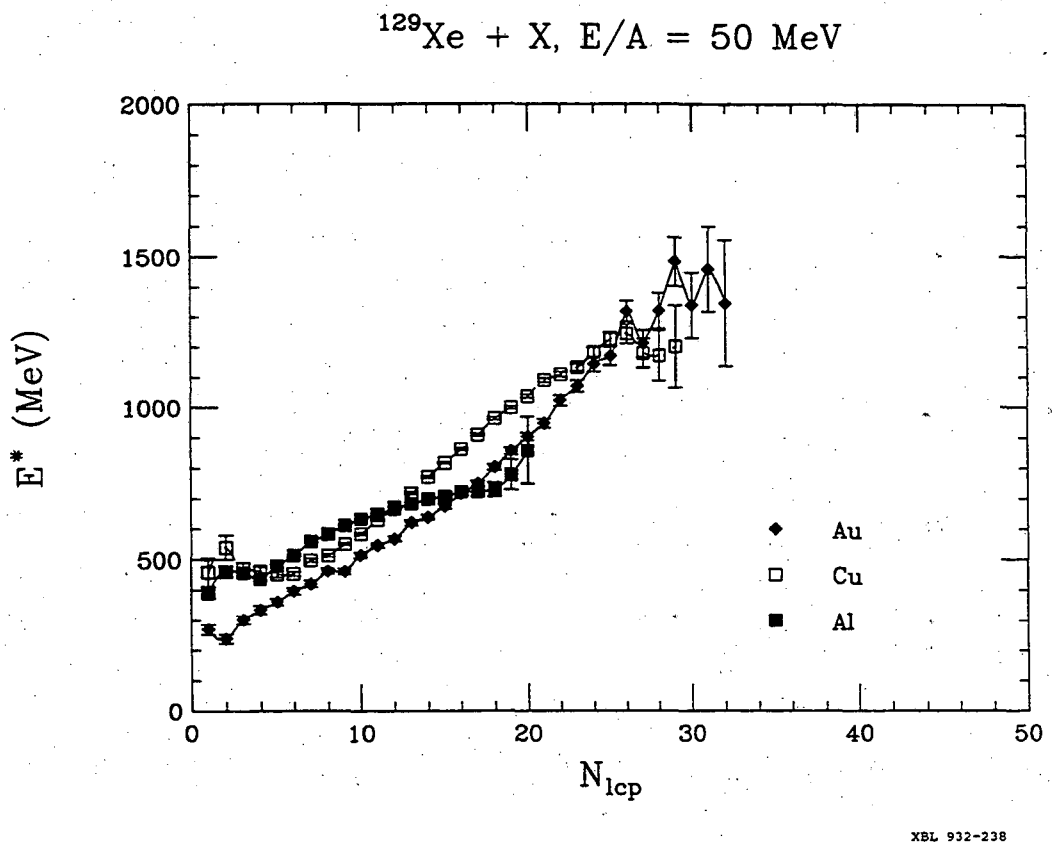
^{129}Xe + X, E/A = 50 MeV
2000
1500
1000
500
0
E* (MeV)
0
10
20
30
40
50
N$_{lcp}$
Au
Cu
Al
XBL 932-238

fig. 25

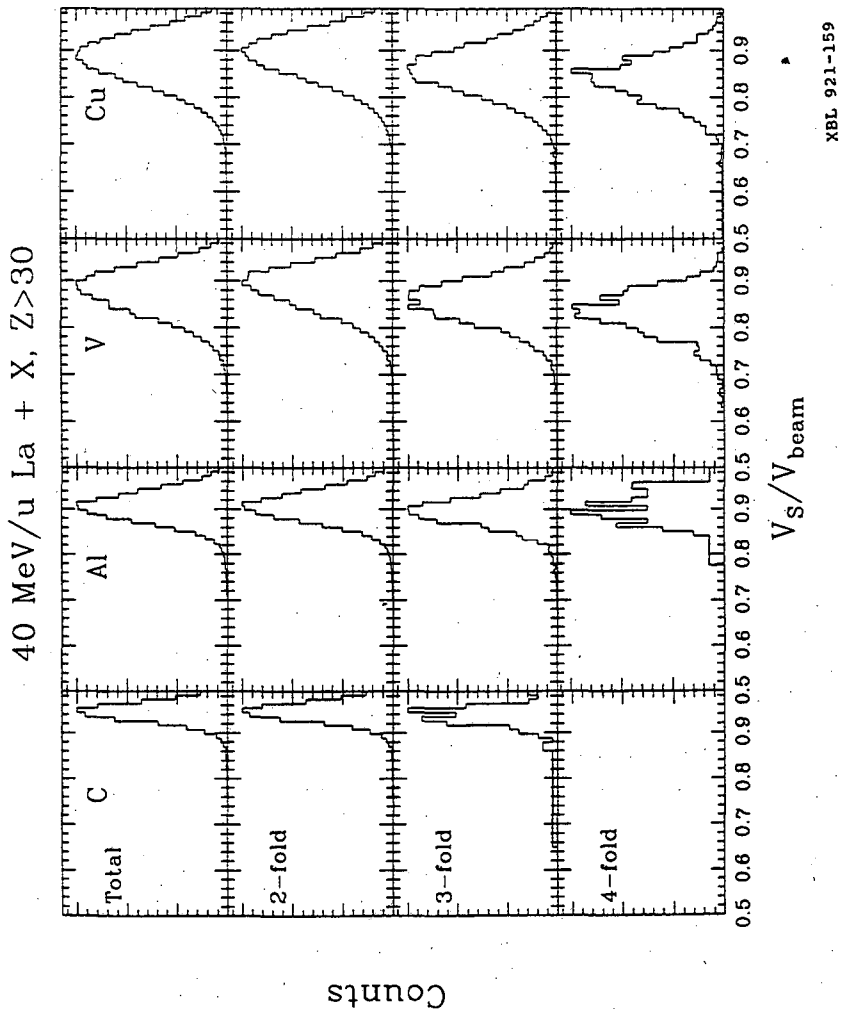
40 MeV/u La + X, Z>30
Total
2-fold
3-fold
4-fold
C
Al
V
Cu
0.5 0.6 0.7 0.8 0.9 0.5 0.6 0.7 0.8 0.9 0.5 0.6 0.7 0.8 0.9 0.5 0.6 0.7 0.8 0.9
V_S/V_{beam}
Counts
XBL 921-159

fig. 26

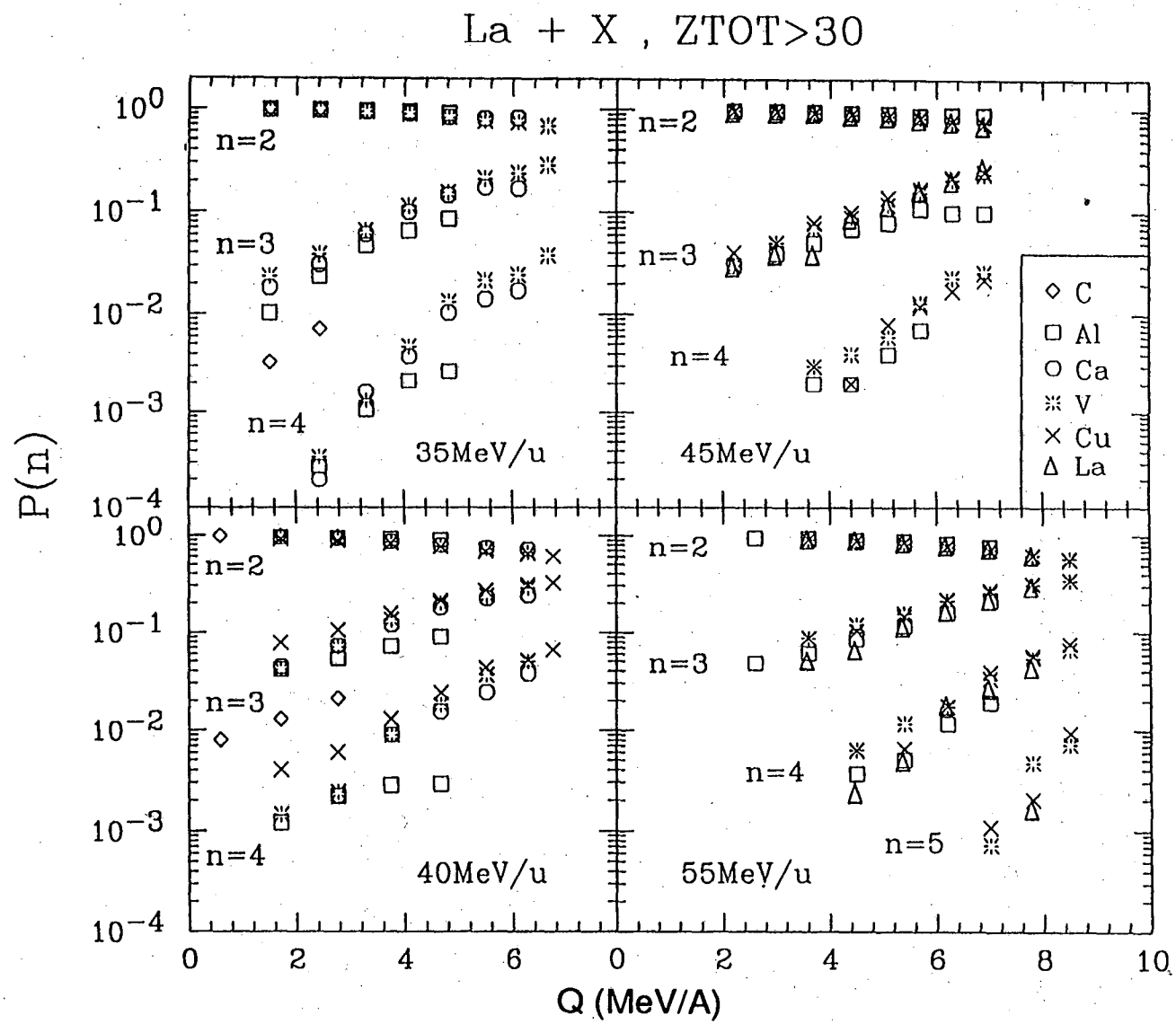
La + X , ZTOT>30
P(n)
Q (MeV/A)
n=2
n=3
n=4
n=5
35MeV/u
45MeV/u
40MeV/u
55MeV/u
C
Al
Ca
V
Cu
La
XBL 921-155 A

fig. 27

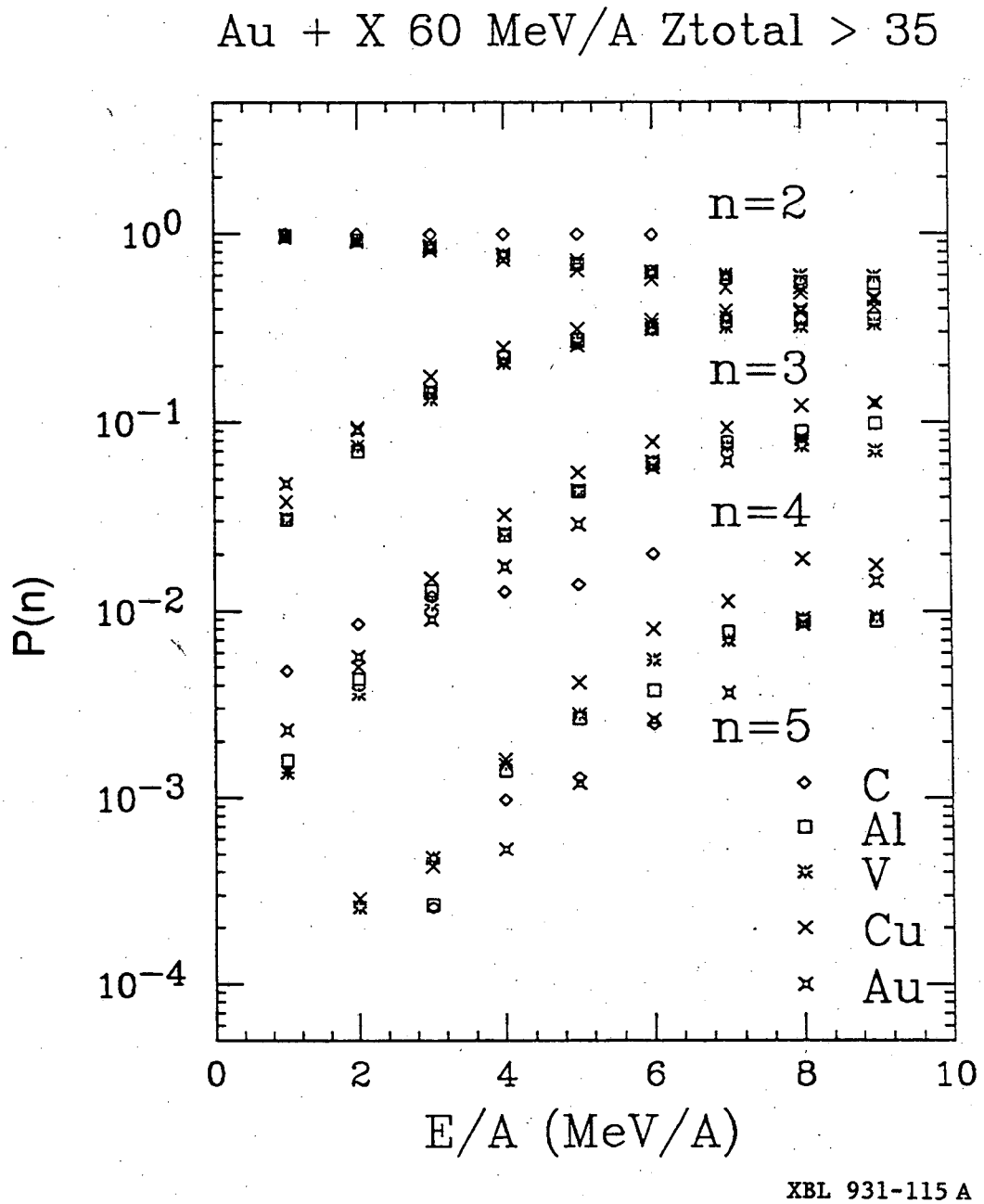
Au + X 60 MeV/A Ztotal > 35
P(n)
10^0
10^{-1}
10^{-2}
10^{-3}
10^{-4}
n=2
n=3
n=4
n=5
C
Al
V
Cu
Au
0
2
4
6
8
10
E/A (MeV/A)
XBL 931-115 A

fig. 28

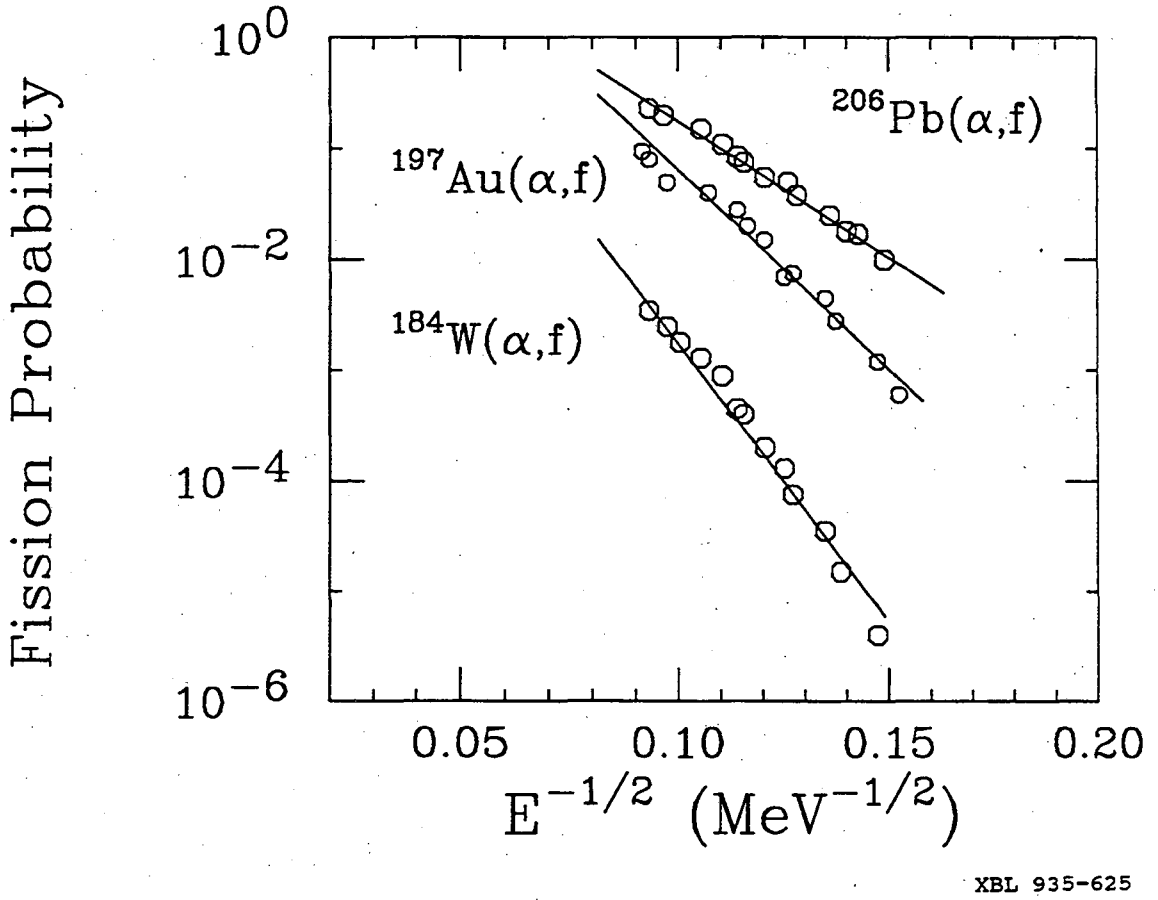
Fission Probability
10^0
10^{-2}
10^{-4}
10^{-6}
^{206}Pb(α,f)
^{197}Au(α,f)
^{184}W(α,f)
0.05
0.10
0.15
0.20
$E^{-1/2}$ ($MeV^{-1/2}$)
XBL 935-625

fig. 29

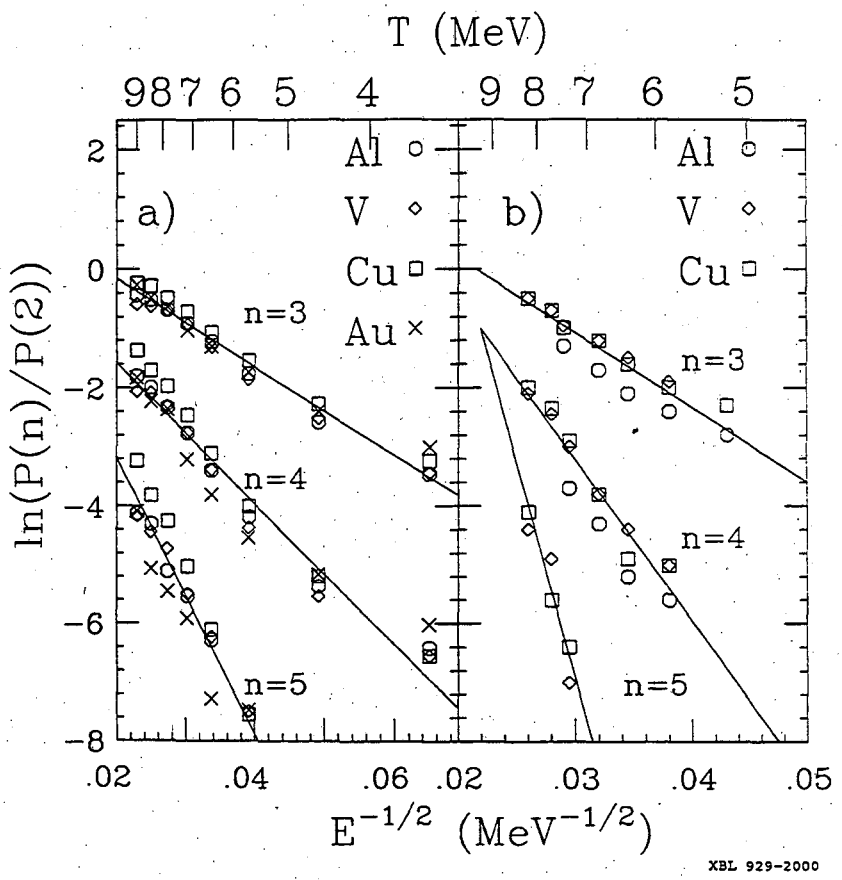
T (MeV)
9 8 7 6 5 4
9 8 7 6 5
a)
b)
Al
V
Cu
Au
n=3
n=4
n=5
ln(P(n)/P(2))
2
0
−2
−4
−6
−8
.02
.04
.06
.02
.03
.04
.05
E^−1/2 (MeV^−1/2)
XBL 929-2000

fig. 30

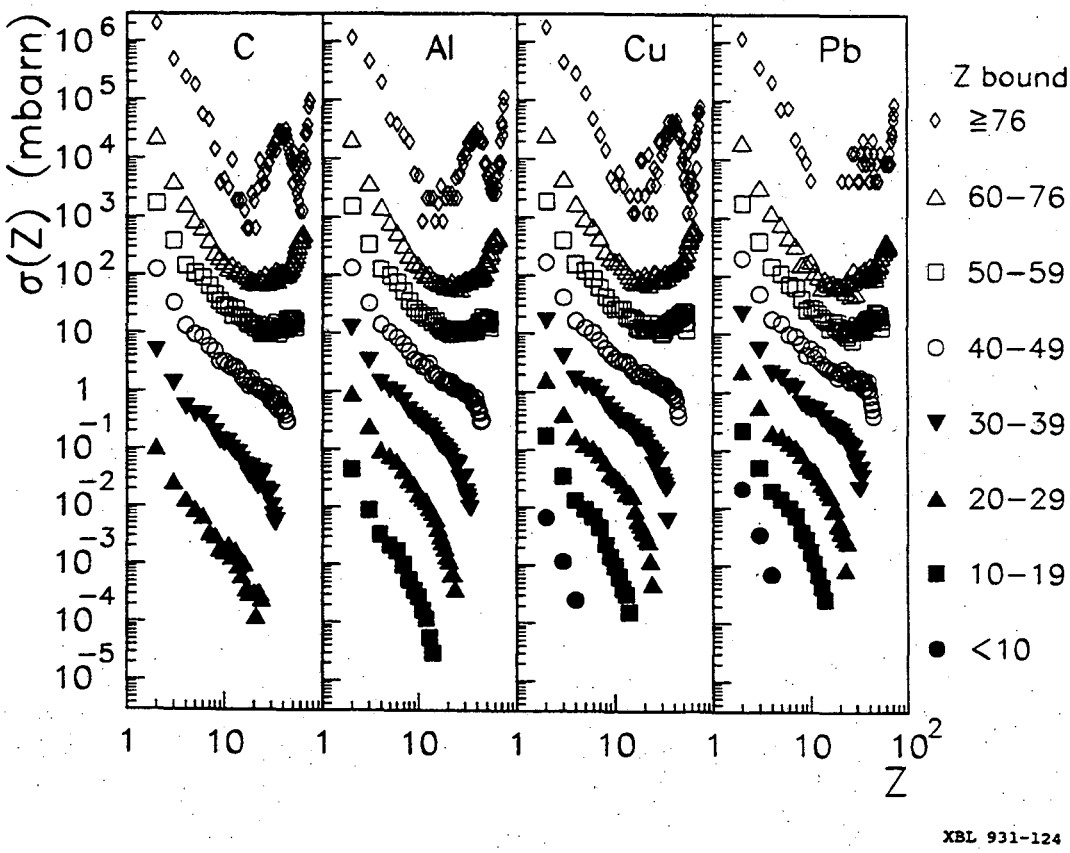
σ(Z) (mbarn)
C
Al
Cu
Pb
Z bound
≧76
60−76
50−59
40−49
30−39
20−29
10−19
<10
Z
XBL 931-124

fig. 31

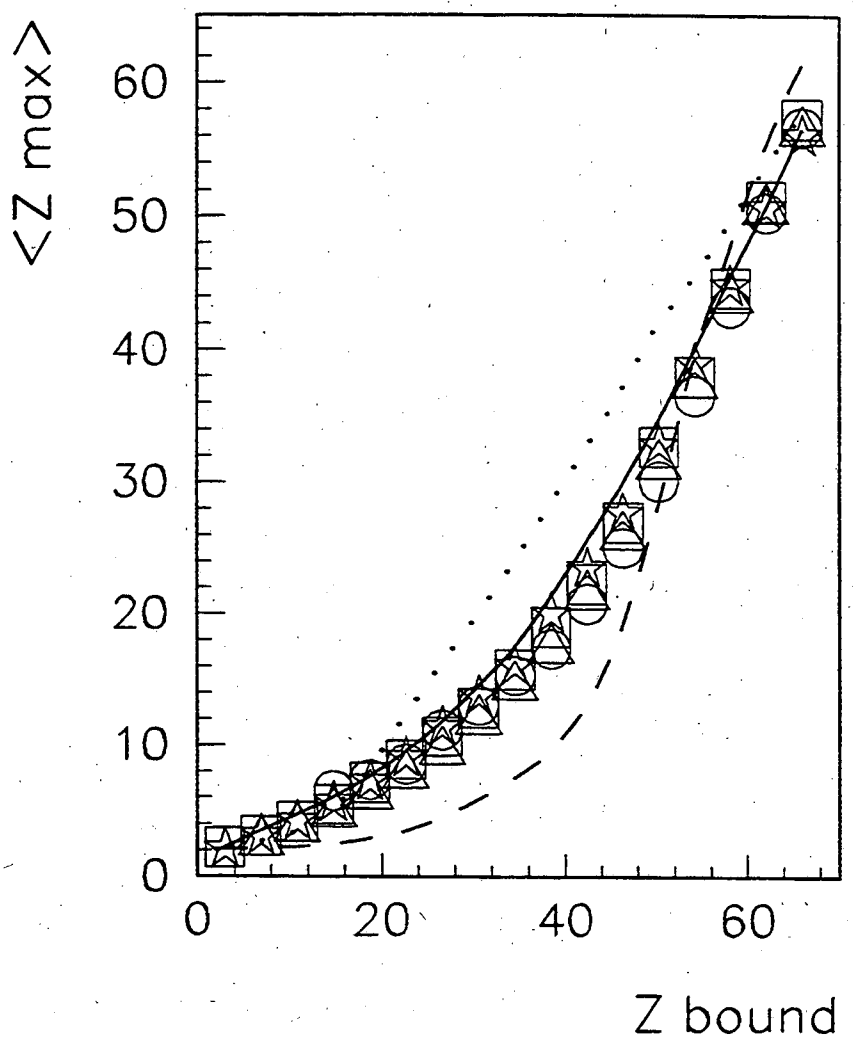

XBL 931-122

fig. 32

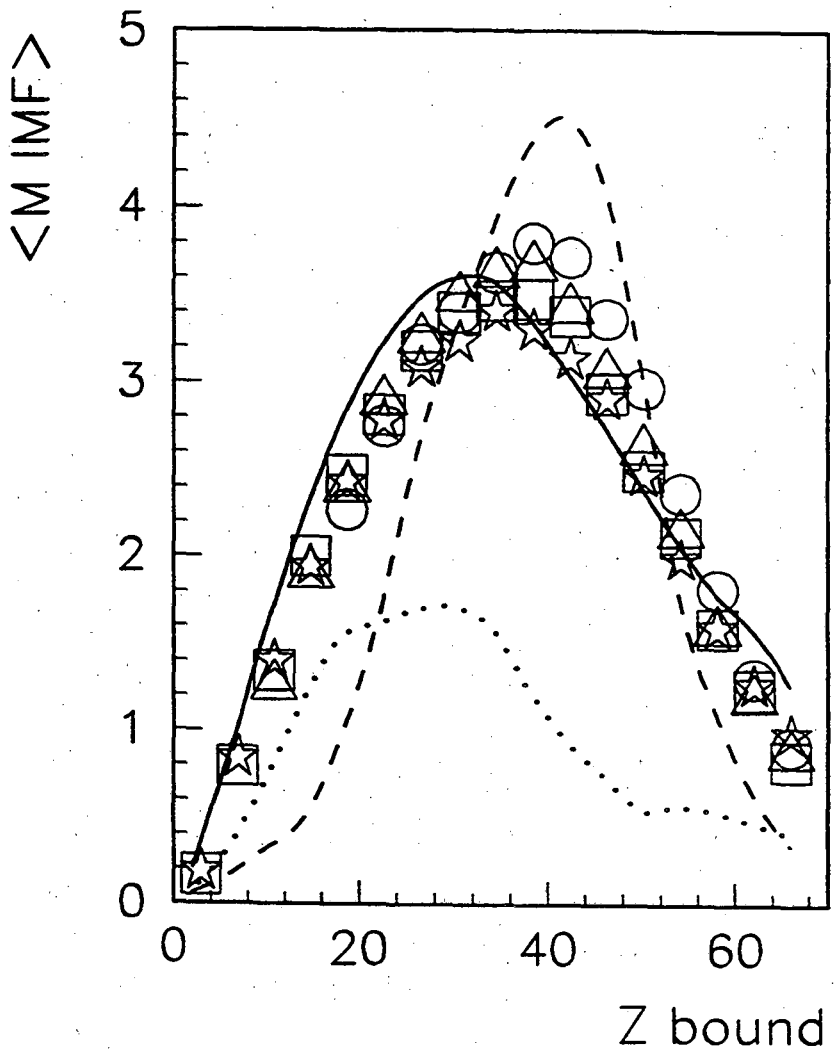

XBL 931-118

fig. 33

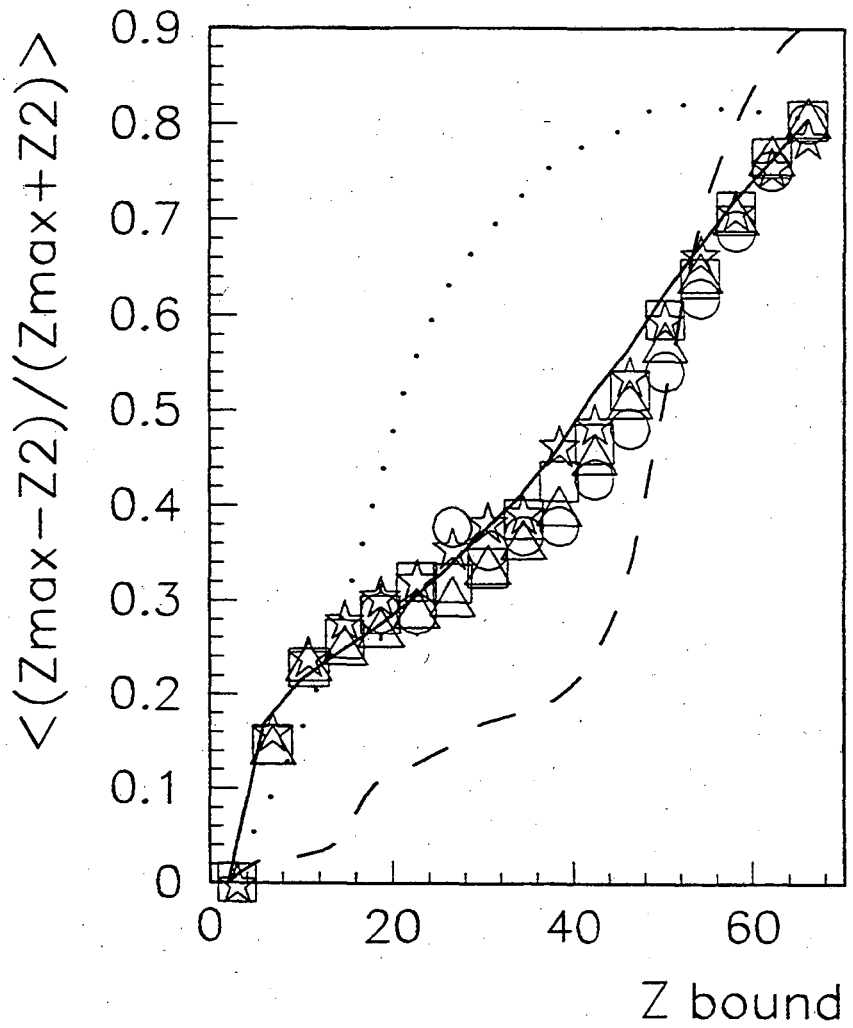

XBL 931-121

fig. 34

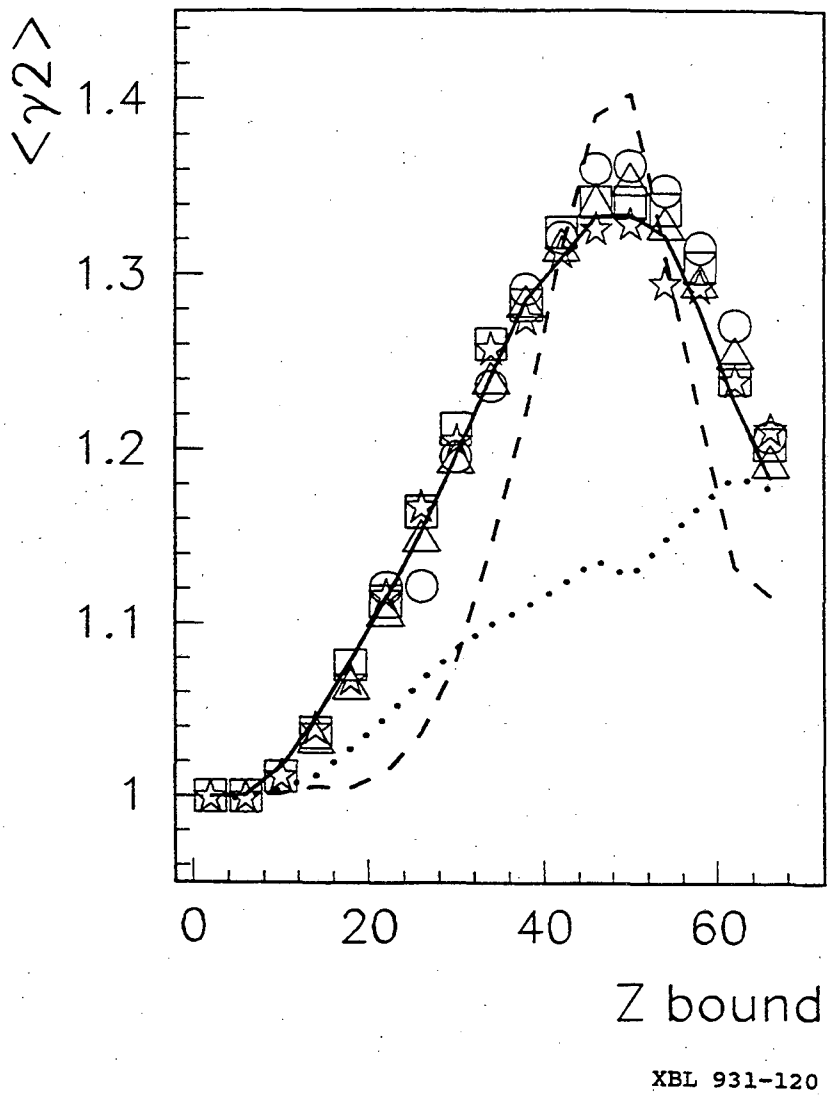

fig. 35

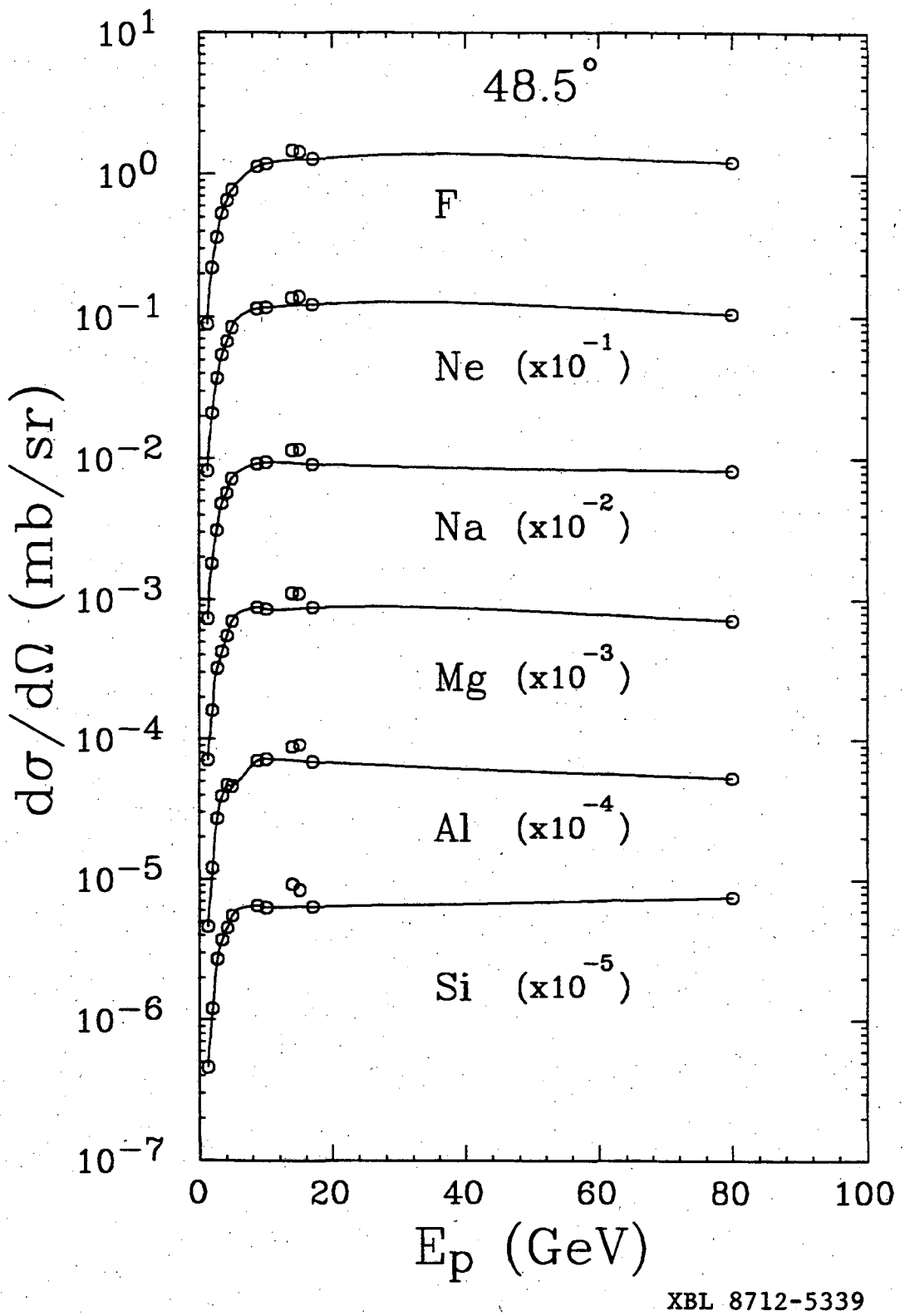
48.5°
F
Ne (x10^{-1})
Na (x10^{-2})
Mg (x10^{-3})
Al (x10^{-4})
Si (x10^{-5})
$d\sigma/d\Omega$ (mb/sr)
E_p (GeV)
10^1
10^0
10^{-1}
10^{-2}
10^{-3}
10^{-4}
10^{-5}
10^{-6}
10^{-7}
0
20
40
60
80
100
XBL 8712-5339

fig. 36

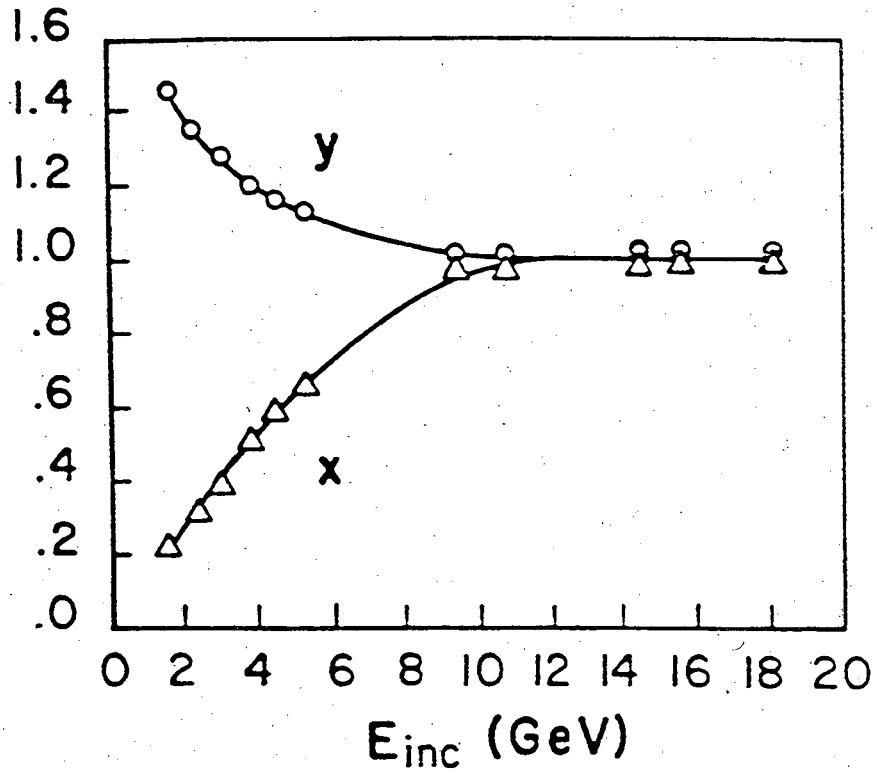

XBL 8712-5337

fig. 37

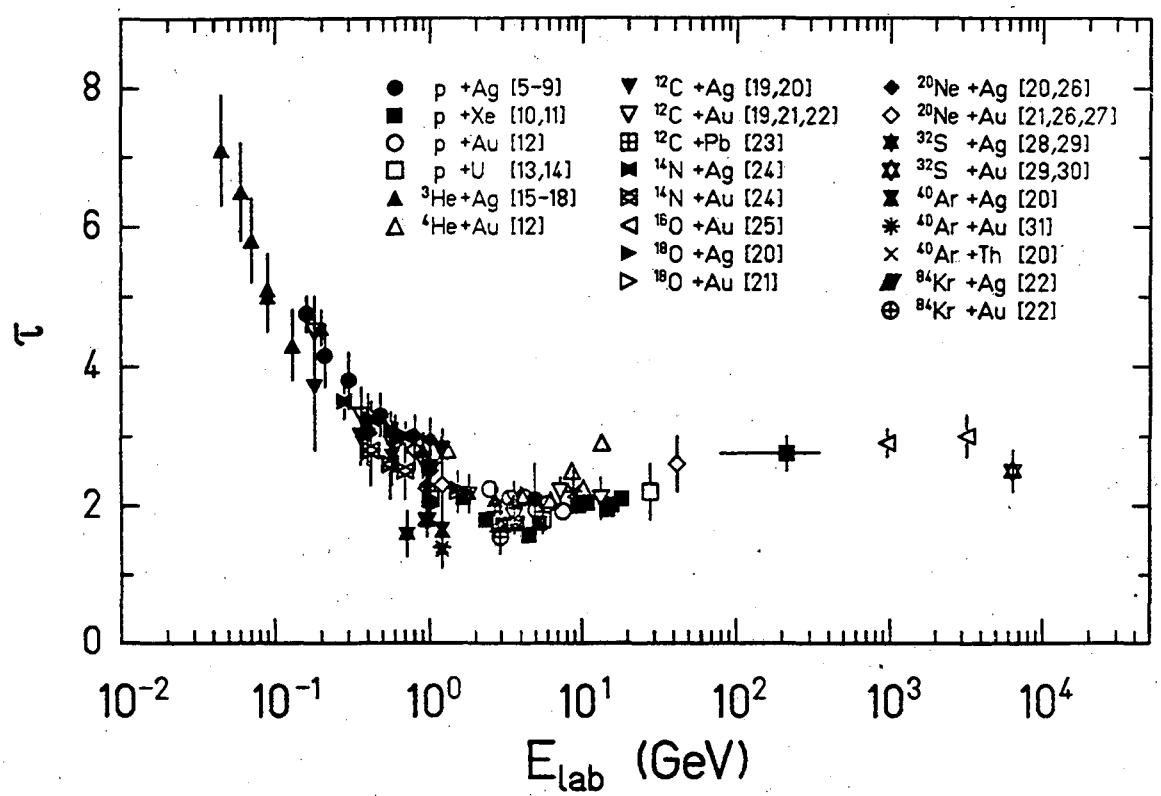

XBL 931-117

fig. 38

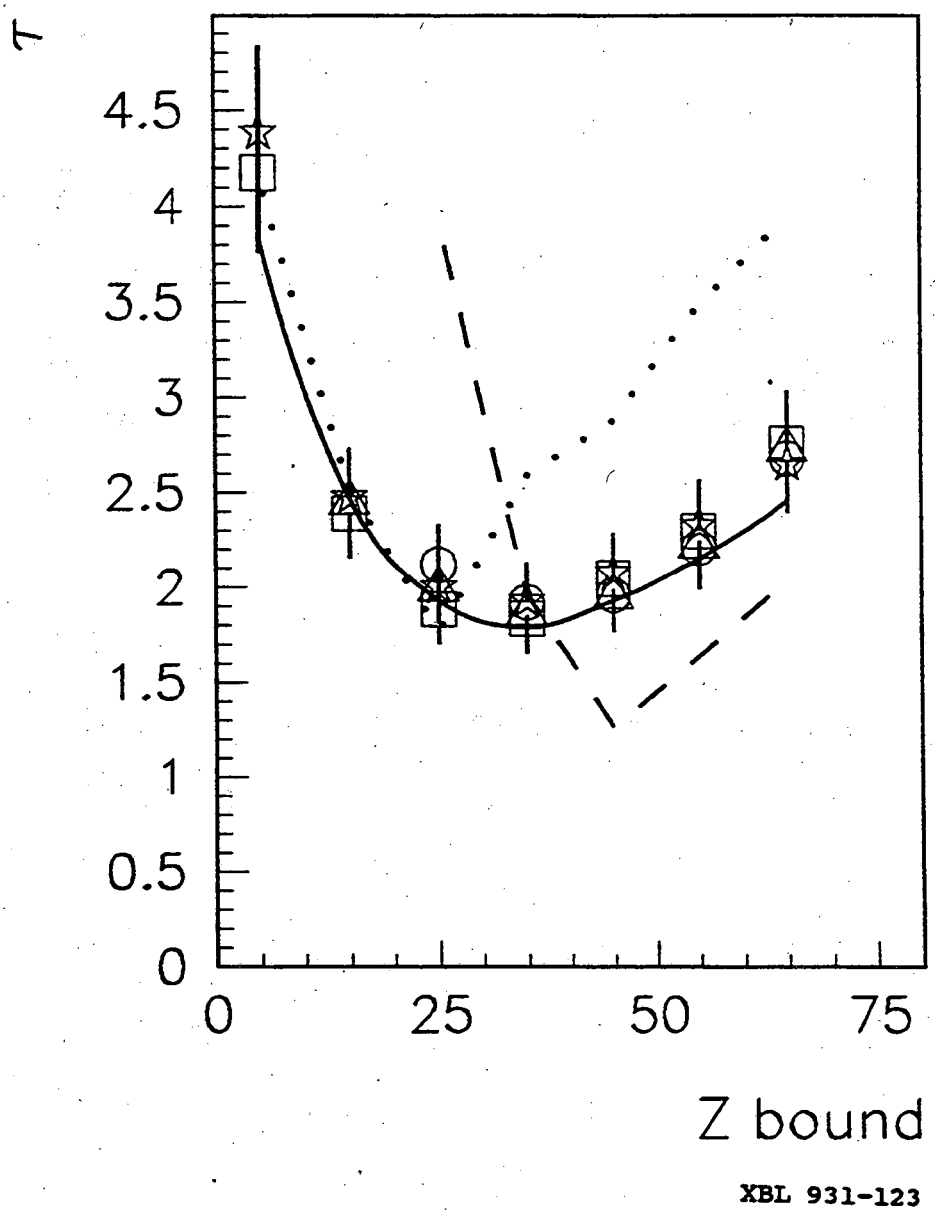

fig. 39

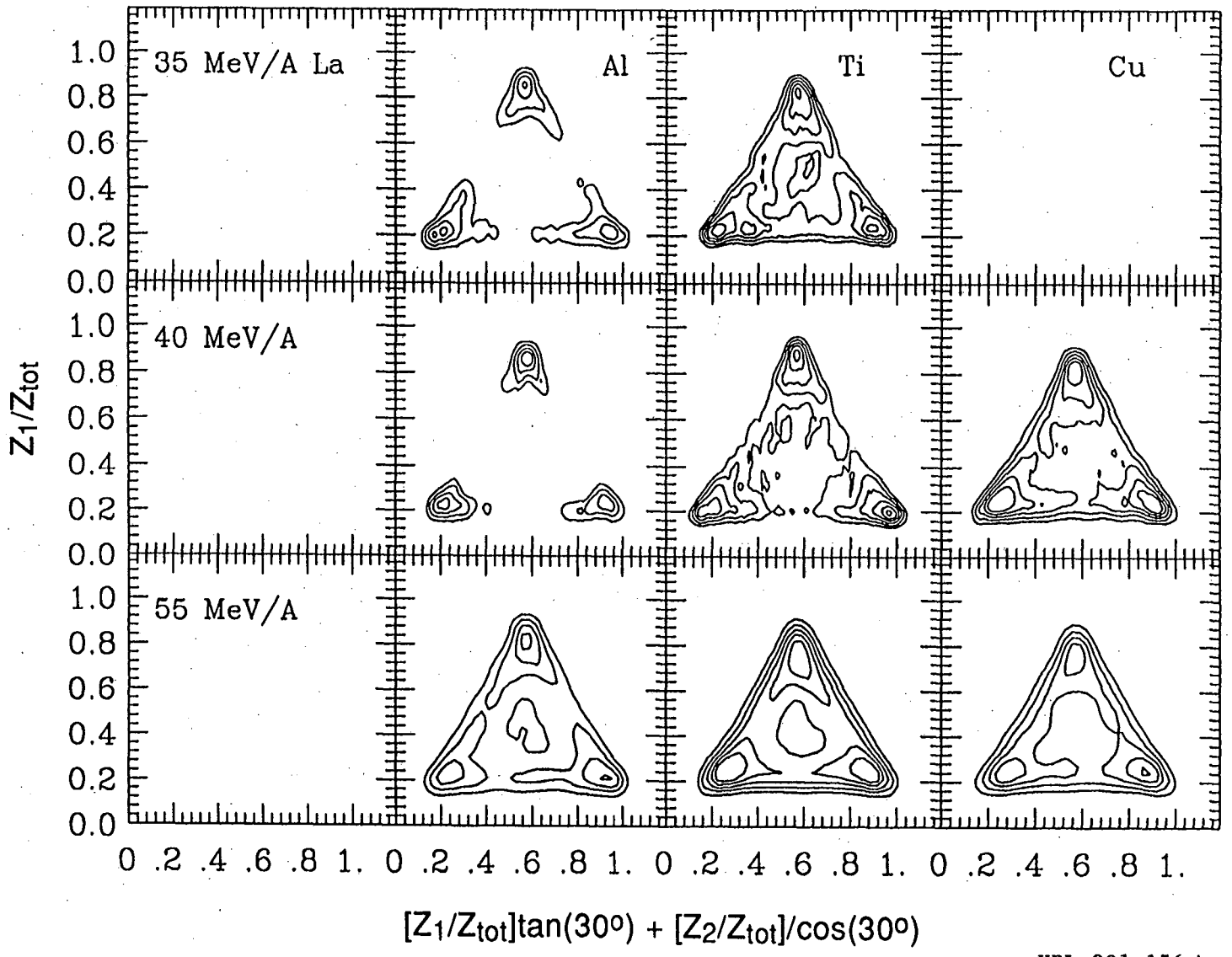

XBL 921-156 A

fig. 40

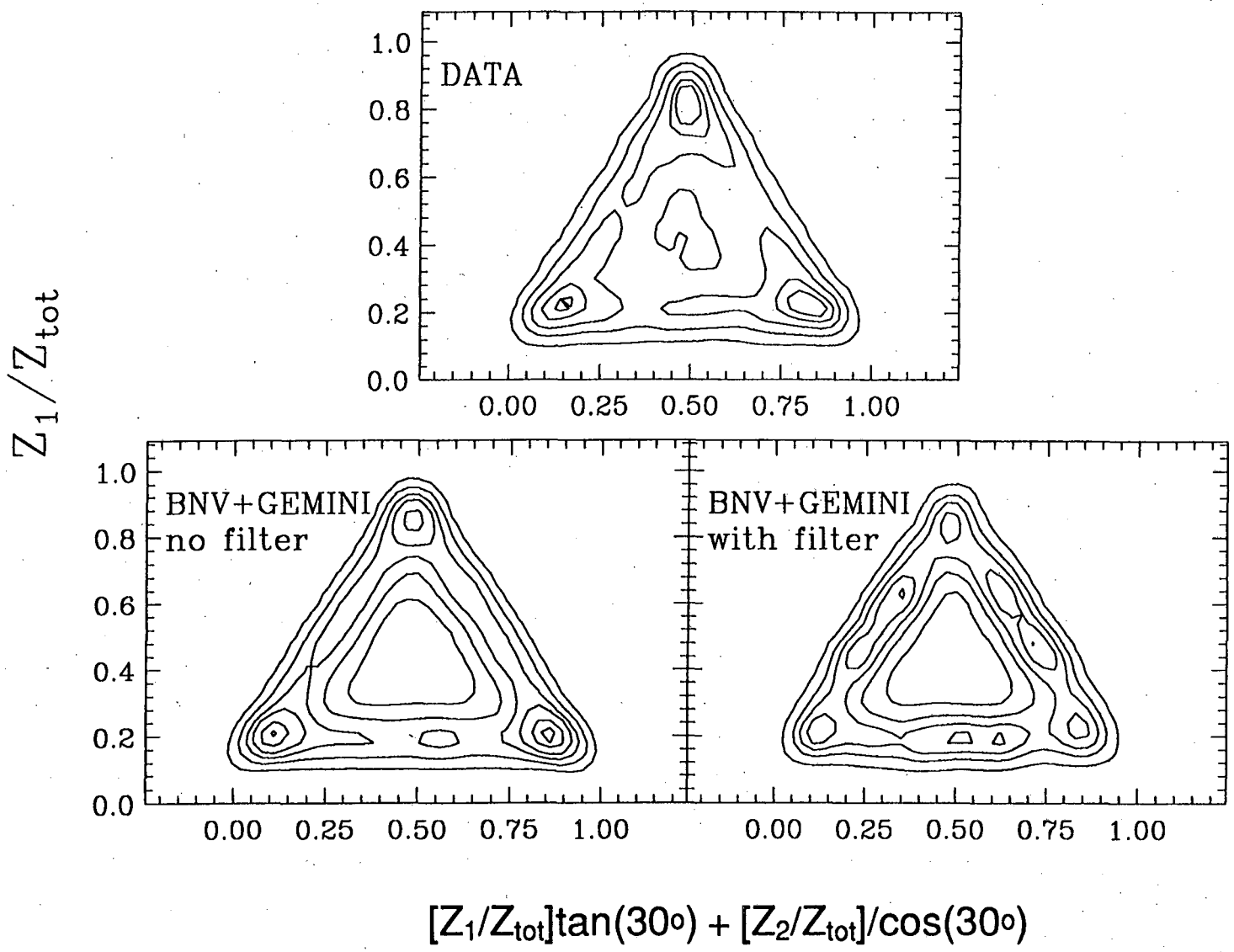

XBL 915-959 A

fig. 41

LAWRENCE BERKELEY LABORATORY
UNIVERSITY OF CALIFORNIA
TECHNICAL INFORMATION DEPARTMENT
BERKELEY, CALIFORNIA 94720

ABH396
LBL Libraries